Energy calibration of the Pierre Auger Observatory using the constant intensity cut method

MASTERARBEIT

zur Erlangung des akademischen Grades
Master of Science
(M. Sc.)

dem Fachbereich Physik der
Universität Siegen

vorgelegt von
Isabell Kristin Steinseifer

Oktober 2008

Contents

1 Introduction **1**

2 Cosmic Rays **3**
2.1 History . . . 3
2.2 Energy spectrum . . . 4
2.3 Extensive air showers . . . 5
2.3.1 Hadronic component . . . 8
2.3.2 Electromagnetic component . . . 8
2.3.3 Muonic component . . . 9

3 Pierre Auger Observatory **11**
3.1 Surface detector . . . 13
3.2 Fluorescence detector . . . 14
3.3 Hybrid measurement . . . 14
3.4 Radio detector . . . 15
3.5 AMIGA and HEAT . . . 17
3.6 Weather . . . 18

4 Surface Detector **23**
4.1 SD Calibration and Monitoring . . . 23
4.2 SD trigger system . . . 25
4.2.1 Local triggers T1 and T2 . . . 25
4.2.2 Event trigger T3 . . . 25
4.2.3 Physical trigger T4 . . . 27
4.2.4 Quality trigger T5 . . . 28
4.2.5 Trigger probability . . . 28
4.2.6 Acceptance . . . 29
4.3 SD event reconstruction . . . 30
4.3.1 CDAS and Offline . . . 30
4.3.2 Angular reconstruction . . . 31
4.3.3 Energy reconstruction . . . 31

5 Constant intensity cut method **35**
5.1 Data set . . . 36

5.2 Description of the constant intensity cut method . . . 36
5.3 Correction . . . 40
5.4 Statistical error estimation of $S_{\mathrm{CIC}}(1000)$ . . . 42
5.4.1 Influence of statistical fluctuations . . . 42
5.4.2 Influence of $\Delta S(1000)$ . . . 42
5.4.3 Influence of $\Delta\Theta$ . . . 46
5.4.4 Error estimation of $S_{\mathrm{CIC}}(1000)$ . . . 48
5.4.5 Error estimation of the attenuation function $f_{\mathrm{CIC}}(\cos^2\Theta)$ . . . 48
5.5 Systematic studies . . . 50
5.5.1 Systematic study of Θ . . . 50
5.5.2 Systematic study of the binning . . . 53

6 Constant intensity cut studies **57**
6.1 Analysis of the attenuation function for different intensity cuts . . . 57
6.2 Energy behaviour of the constant intensity cut method results . . . 59
6.3 Seasonal dependency on the constant intensity cut method results . . . 62
6.4 Weather dependency of the constant intensity cut method results . . . 66
6.4.1 Temperature . . . 66
6.4.2 Humidity . . . 70
6.4.3 Pressure . . . 73
6.4.4 Density . . . 73
6.5 Distance dependency of the constant intensity cut method . . . 76
6.5.1 Distance to the shower axis . . . 76
6.5.2 Distance to shower core . . . 79

7 Summary and outlook **85**

A Figures of Chapter 5 **89**

B Figures of Chapter 6 **99**

List of Figures **116**

List of Tables **117**

List of Acronyms **119**

Bibliography **121**

Acknowledgement **125**

Erklärung **127**

Chapter 1

Introduction

Since their discovery, nearly 100 years ago, cosmic rays are one of the most fascinating mysteries. Physicists study cosmic rays to answer the fundamental questions, like the origin of cosmic rays, their energy spectrum, particle interactions at high energies and acceleration mechanisms. To take a step forward to the answers, the Pierre Auger Observatory was built. The data acquisition started, during the installation period, in January 2004.

The Pierre Auger Observatory, located in Argentina, is the largest detector installation to measure ultra high energy cosmic rays (UHECR) until now. The surface detector array covers an area of 3000 km^2 and is therefore able to detect secondary particles of cosmic rays up to energies of $E = 10^{20}$ eV. The four fluorescence detectors measure the longitudinal energy development of extensive air showers. The combination of these two independent detector techniques allow hybrid measurements. These hybrid measurements can also be used for cross-checks and calibrations.

The knowledge of the energy spectrum will answer several questions. To investigate the energy spectrum of cosmic rays, the measured signals of the surface detector stations have to be converted to energies. Therefore, the constant intensity cut method is adopted. The scope of this thesis is to develop an ansatz for the constant intensity cut method.

Chapter 2 gives a short overview about cosmic rays, their energy spectrum and extensive air showers. The Pierre Auger Observatory in general is introduced in Chapter 3 and in Chapter 4 the focus is on the surface detector in particular. The calibration of surface detector events, the different trigger levels and both the angular and the energy reconstruction are described. In Chapter 5, the ansatz of the constant intensity cut method is explained. The procedure and the error estimation are discussed in detail. The energy independence is investigated in Chapter 6. Furthermore, it is studied, if the constant intensity cut method results are influenced by changing weather conditions or by the distance between the shower axis and the surface detector station with the highest signal. Finally, in Chapter 7, the results of the thesis are summarised and an outlook on possible further studies is given.

Chapter 2

Cosmic Rays

Highly energetic particles originating from outer space, called cosmic rays or cosmic radiation, are permanently hitting and penetrating the Earth‘s atmosphere. The major part of cosmic rays, 98%, are protons and nuclei. The remaining 2% of the charged cosmic radiation are electrons and the neutral part is consisting of neutrons and photons [1]. Cosmic rays entering the earth's atmosphere interact with molecules of the air, in most cases nitrogen or oxygen, thereby initiating extensive air showers.

2.1 History

After the discovery of radioactivity by Henri Becquerel in 1896, it was supposed that the conductivity (ionisation) of air is due to radioactivity in the soil or radioactive gases. In 1910, Theodor Wulf measured reduced ionisation rates on the top of the Eiffel tower using an electrometer, which confirmed the assumption of the Earth's crust as the origin for the atmospheric conductivity. Two years later Viktor Hess made balloon flights, to enlarge the distance to the ground, and also measured the ionisation using an electrometer. He found out, that the ionisation decreases up to 1500 m, but increases again with higher altitudes and reaches higher values in 3600 m than at the ground. This discovery gave reason for the idea that, in addition to the terrestrial component, there has to be a extraterrestrial source. Hess postulated the existence of a source located above the atmosphere, to explain the phenomenon. Further measurements of Werner Kohlhörster at altitudes up to 9000 m verified this assumption in 1914.

Robert Millikan was the first, who called this extraterrestrial source "cosmic rays". He found out, that cosmic rays are able to interact with particles in the atmosphere. The particles, produced by the interactions, were called "secondary particles". Some years later these particles could be detected using cloud chambers and photographic plates.

In 1936, Pierre Auger detected time coincidences of secondary particles with spatially separated detectors on ground level. He postulated, that these secondary particles are part of a cascade initiated by one cosmic ray. The measurements of these cascades allowed the first energy estimations of primary cosmic rays. Pierre Auger measured primary particles with energies up to $E = 10^{15}$ eV [2]. Because of the similar detection technique, the Pierre Auger Observatory obtained its name [3][1].

In the recent past many cosmic ray observatories were build to explore the mysteries of cosmic rays and their sources. From 1981 until 1993 the Fly's Eye Detector was taking data with fluorescence telescopes in Utah, USA [4]. The High Resolution Fly's Eye Cosmic Ray Detector, called HiRes, was the advancement of Fly's Eye and took data from 1997 until 2006. It made the first observation of the GZK-cutoff [5][6]. The Akeno Giant Air Shower Array (AGASA) in Japan consisted of 111 surface detectors and 27 muon detectors under absorbers and was operating from 1991 until 2004, to measure the energy spectrum of ultra high energy cosmic rays (UHECR) [7]. The KArlsruhe Shower Core and Array DEtector-Grande, KASCADE-Grande, is an extension of the KASCADE detector array which consists of 252 scintillation detectors. It is running since 1996 in Karlsruhe, Germany, and is sill taking data. The main issues of KASCADE-Grande are the analysis of the chemical composition and of the energy spectrum of primary cosmic rays. Since 2004 the Pierre Auger Observatory explores cosmic rays of the highest energies.

2.2 Energy spectrum

The energy range of cosmic rays reaching the Earth's atmosphere covers energies from 10^9 eV to 10^{20} eV. In Figure 2.1 the particle flux I is plotted against the energy E. The following power law describes the energy dependent flux:

$$\frac{dI}{dE} \propto E^{-\gamma}, \tag{2.1}$$

with the spectral index $\gamma = 2.7 - 3.1$. For cosmic rays with energies between 10^{11} eV and $4 \cdot 10^{15}$ eV, the spectral index is $\gamma = 2.7$. There is a bend at $E = 4 \cdot 10^{15}$ eV, called the "knee", where γ changes to 3.1. The "knee" was discovered in 1958 and measured by KASCADE Grande, e.g. [8]. A "second knee" is expected to be at $\sim 10^{17}$ eV, but its existence is controversial. At an energy of $E = 4 \cdot 10^{18}$ eV the spectral index changes again to $\gamma = 2.7$. This bend is called "ankle". It has been observed by Fly's Eye [4], Haverah Park [9], confirmed by Yakutsk [10], HiRes [5] and by Auger hybrid events [11]. The change of the origin of primary cosmic rays from galactic to extragalactic sources is supposed to be the reason for the ankle.

The energy spectrum is measured by different types of experiments, as shown in Figure 2.2. It is possible to measure primary particles with energies up to 10^{13} eV directly using balloons or satellites experiments. The flux of particles is very large and hence a detection area in the order of magnitude of m^2 is big enough to detect particles in a reasonable frequency. But for higher energies a larger detection area is necessary and this can not be put into practice with balloons or satellites. For this reason, cosmic rays with energies $E > 10^{13}$ eV are measured indirectly by detection areas at the ground of the earth. At an altitude of around 20 km, the primary cosmic rays initiate cascades of secondary particles. These secondary particles can be measured at ground level and the characteristics of the primary cosmic particle can be reconstructed. The cosmic ray experiments mainly aim at measuring the energy regions around the knee or the ankle and beyond the extreme energies of up to 10^{20} eV. Thus the Pierre Auger Observatory covers an detection area of 3000 km^2, in order to measure the ankle, UHECR and to proof the existence of the

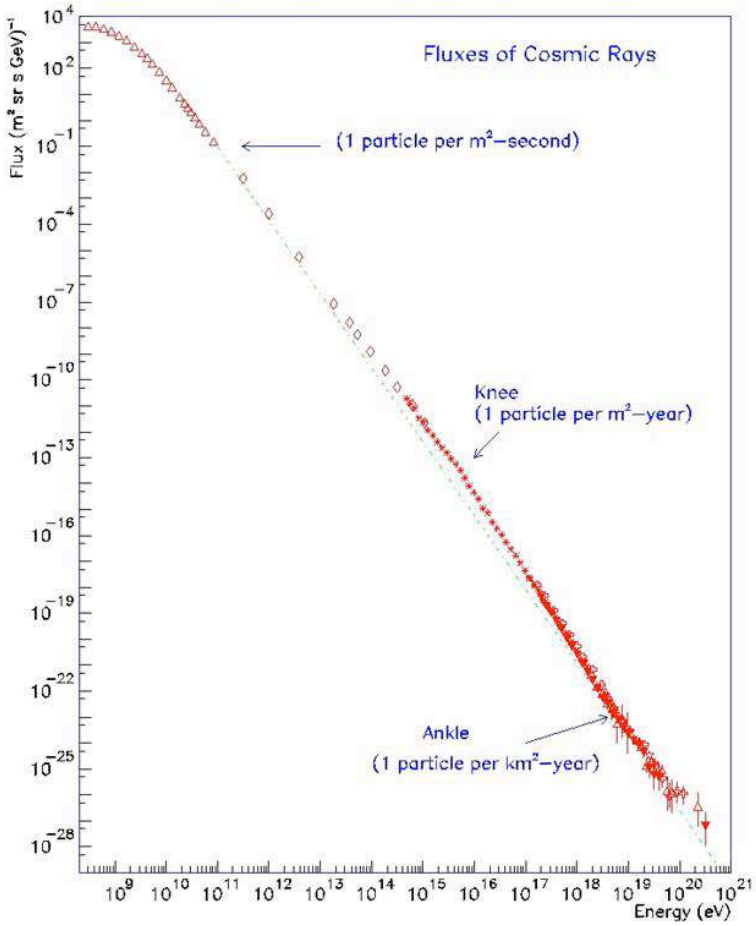

Figure 2.1: Energy spectrum of primary cosmic rays [12]. The ”knee” and the ”ankle” are illustrated.

GZK-cutoff. Greisen, Zatsepin and Kuzmin postulated a cutoff of cosmic rays at energies higher than $6 \cdot 10^{19}$ eV, since the flux is extremely low in this energy region [13]. In 1966, they proposed that particles with $E > 6 \cdot 10^{19}$ eV interact with the photons of the cosmic microwave background radiation to produce pions. This interaction continues until the energy of the cosmic ray particle falls below the pion production threshold. The probability of a particle with $E = 8 \cdot 10^{19}$ eV to pass 100 Mpc without having at least one GZK interaction is 10%, the possibility of a particle with $E > 3 \cdot 10^{20}$ eV to pass 50 Mpc is only 0.1%. Therefore half of the particles with energies higher than 10^{20} eV originate within a radius of 20 Mpc. First results of the Pierre Auger Observatory support the existence of the GZK-cutoff [14].

2.3 Extensive air showers

Primary cosmic rays initiate extensive air showers (EAS) when they penetrate the Earth’s atmosphere. Cascade initiation takes place in an altitude of around 20 km. The primary particle interacts with a nucleus of the atmosphere, which in most cases is the nucleus

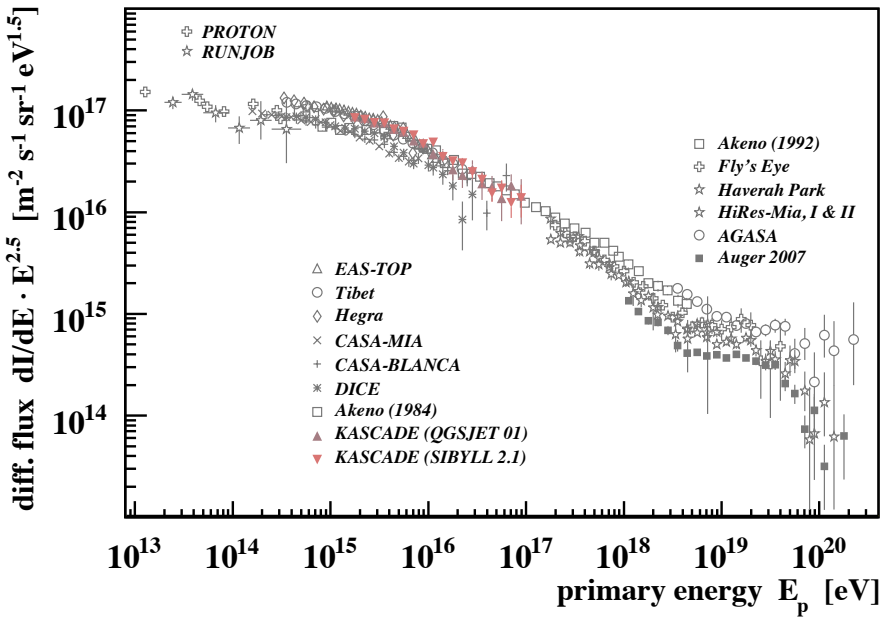

Figure 2.2: Energy spectrum measured by different cosmic ray experiments [15]. The differential particle flux $\frac{dI}{dE}$ is multiplied by a factor of $E^{2.5}$, to illustrate the structure in detail. Data points measured with the Pierre Auger Observatory are marked with grey quadrates.

of a nitrogen atom, and a multitude of secondary particles is produced. The number of particles first increases, because the secondary particles also interact with components of the atmosphere and new secondary particles arise. After a maximum of particles, their number decreases. The altitude, where the shower contains the maximum number of secondary particles, is called the shower maximum X_{max}. This altitude depends on the energy and the type of primary particle. When the energy of secondary particles is too low to produce new particles, the extensive air shower decreases exponentially with the atmospheric depth. Most air showers die before they reach the ground. Just a small fraction of secondary particles, produced by a cosmic ray, can be detected. The number of produced secondary particles at the shower maximum increases with growing energy of the primary cosmic ray.

An air shower propagates with nearly the speed of light. The shower front can be described by a curved disc with a surface area in the order of magnitude of km^2 and a thickness of a few meters. In the centre, the particle density is much higher than at the edges and the thickness of the disc increases from the shower axis to the border. The shower front of an extensive air shower is illustrated on the right of Figure 2.3. The secondary particles, produced in an extensive air shower, are composed of a hadronic (1%), an electromagnetic (95%) and a muonic component (4%), described in the following sections.

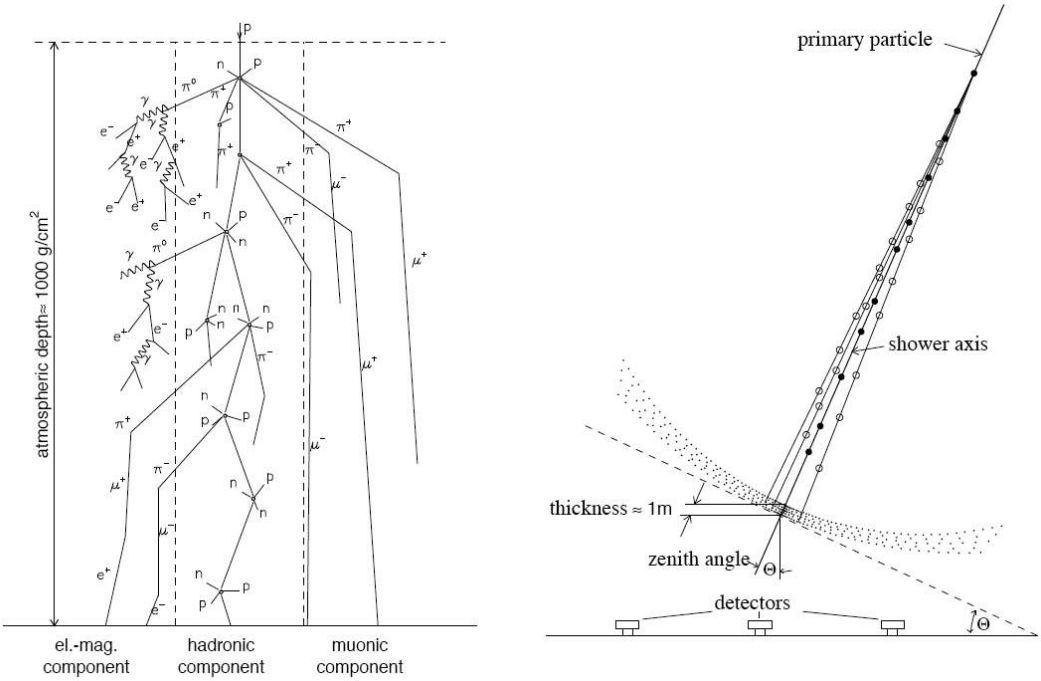

Figure 2.3: On the left: Development of an extensive air shower and fragmentation into the hadronic, electro magnetic and muonic component. On the right: Shower front coming down to a detector array. The edge of the disk is thicker than the centre, the particle density near the shower axis is higher. [16]

2.3.1 Hadronic component

The hadronic component only contains about 1% of the produced particles in an air shower. When a hadron, mostly a proton, enters the atmosphere and interacts with an atmospherical constituent, secondary particles arise in a strong interaction. These secondary particles decay or interact again with air components, to produce further secondary particles. In the most cases, these secondaries are pions, less frequently kaons, protons and neutrons. Charged pions are supposed to be involved in interactions, while neutral pions mostly decay, $\pi^0 \longrightarrow 2\gamma$, because their interaction length is much higher than their decay time (see Section 2.3.2). Until the secondary hadrons drop below the energy threshold to produce new particles, the cascade of secondaries is growing. After that the particles lose their energy by ionisation until they decay and the number of particles decreases exponentially. Because the transverse momentum of secondary hadrons is very small, compared to the total momentum, the cascade of secondaries develops along the shower axis and only reaches a maximum distance of up to 20 m. Although the hadronic component is only 1% of the produced particles, it is very important, because it feeds the electromagnetic and the muonic component.

2.3.2 Electromagnetic component

The hadronic component primarily feeds the electromagnetic component. The decay of the neutral pion π^0 into 2γ initiates an electromagnetic cascade. The γ's produced create e^+e^- pairs in pair production:

$$\gamma + \text{nucleus} \longrightarrow e^+ + e^- + \text{nucleus}.$$

These electrons and positrons generate 2γ again. This process is called Bremsstrahlung:

$$e^\pm + \text{nucleus} \longrightarrow e^\pm + \text{nucleus} + \gamma.$$

Pair production and Bremsstrahlung take place alternatively and, therefore, cause a cascade. Due to the fact, that neutral pions are produced again and again, many electromagnetic cascades are initiated, that contribute to the electromagnetic component. An electromagnetic cascade can also be initiated by a primary electron. Then the generation of a hadronic component is improbable.

Depending on the energy of the primary particle, the electromagnetic component reaches a lateral spread in the order of magnitude of km^2. It is caused by Rutherford scattering. J. Nishimura, K. Kamata and K. Greisen proposed a function to describe the lateral distribution, called the NKG function: The electron density ρ_e, in dependence on the distance r to the shower axis, is given by

$$\rho_e(r) = \frac{\Gamma(4.5-s)}{\Gamma(s)\cdot\Gamma(4.5-2s)} \cdot \frac{N_e}{2\pi r^2} \left(\frac{r}{r_M}\right)^{s-2} \cdot \left(1+\frac{r}{r_M}\right)^{s-4.5}, \tag{2.2}$$

with the number of electrons N_e at observation level, the Molière radius r_M, which is $r_M = 79$ m at sea level, and the longitudinal shower age s. The longitudinal shower age s, which describes the age of the extensive air showers, is $s = 0$ at the initiation of the

shower, $s = 1$ at the shower maximum and $s = 2$, when the shower dies out. The NKG function is valid between $0.8 < s < 1.6$ [17].

The fraction of photoelectric effect, Compton scattering and ionisation can be neglected considering to the energy necessary for the cascade development.

2.3.3 Muonic component

Muons are mostly produced by the decay of charged mesons (weak interaction). The following decays of pions and Kaons are predominant:

$$\begin{aligned} \pi^{\pm} &\longrightarrow \mu^{\pm} + \nu_{\mu}\ (\overline{\nu}_{\mu}), \\ K^{\pm} &\longrightarrow \mu^{\pm} + \nu_{\mu}\ (\overline{\nu}_{\mu}), \\ K^{\pm} &\longrightarrow \pi^{0} + \mu^{\pm} + \nu_{\mu}\ (\overline{\nu}_{\mu}). \end{aligned}$$

Most of the muons are produced at an early shower age. Because the density of the atmosphere decreases with increasing altitude, mesons decay mainly in high altitudes. Muons lose their energy predominantly in ionisation. They are not affected by strong interaction and, therefore, they fly almost undisturbed through the atmosphere. Although only 4% of the particles produced in an air shower belong to the muonic component, around 80% of the particles at sea level are muons. Muons pass the atmosphere with almost the speed of light and, therefore, are influenced by time dilatation. Without time dilatation they would decay after a distance of 600 m and the probability, that a muon reaches the sea level, would be very low.

Chapter 3

Pierre Auger Observatory

The southern site of the Pierre Auger Observatory (PAO) is located in the Pampa Amarilla, near Malargüe in the province of Mendoza, Argentina. The Pierre Auger Observatory is an air shower experiment, built to measure extensive air showers, which are caused by ultra high energy cosmic rays (UHECR). One of the main aims of the Pierre Auger Observatory is to verify the postulated GZK-cutoff at $6 \cdot 10^{19}$ eV, described in Section 2.2. Therefore, the observatory is designed to the highest energetic cosmic rays. It is able to measure energies in the range of 10^{17} to 10^{20} eV. Another purpose of the Pierre Auger Observatory is to measure the "ankle", which is assumed to be at about $4 \cdot 10^{18}$ eV, as specified in Section 2.2. It is also used to search for anisotropies in the distribution of arrival directions and regarding this matter, an article concerning correlation with active galactic nuclei (AGN) was published in 2007 [18]. Cosmic rays are deflected by intergalactic magnetic fields. Only for cosmic rays with energies above 10^{19} eV these deflections are small enough, to trace back the origin of the primary particles. Particles at energies above 10^{19} eV proximately arrive only once per year and square kilometre, particles of energies above 10^{20} eV arrive only once per century and square kilometre. Because the particle density of these UHECR is very low, the detection area has to be large, in order to detect many of those rare events. Therefore the southern site of the observatory covers an area of 3000 km^2 and is the largest detector facility to observe UHECR.

The Pierre Auger Observatory uses two detection techniques to observe cosmic rays. The surface detector (SD) consists of 1600 water Cherenkov tanks, arranged in a hexagonal structure. Four fluorescence detectors (FD), each consisting of six fluorescence telescopes, are arranged along the edges of the array. The combination of both methods results in a hybrid detector. In Figure 3.1 the detector array is shown. Radio antennas have been installed as an additional component. A first test setup is built.

The Pampa Amarilla near Malargüe is an ideal location for a cosmic ray observatory. Because of the Andes, which work like a barrier, the weather conditions are optimal. They shield the Pampa Amarilla from clouds. Most of the time the sky is clear and only low precipitations are measured. Furthermore, no sources of light pollution, like large cities, are located near the detector array. These cloudless, clear and dark conditions are necessary for the FD measurements. The experiment is located on a plateau at an average

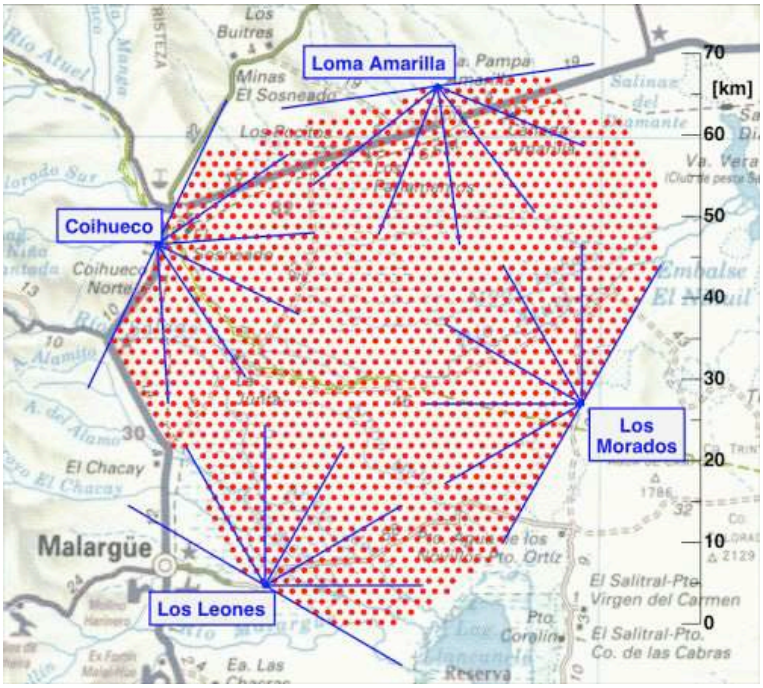

Figure 3.1: The surface detector array of the Pierre Auger Observatory covers an area of 3000 km^2. Each dot illustrates the position of one of the 1600 water Cherenkov tanks. The hexagonal structure is visible very well. The fluorescence detector stations are located at the borders of the array. Each of the six fluorescence telescopes has a field of view of $30° \times 30°$, marked by the lines. This results in a total field of view for each telescope station of $180° \times 30°$ [19].

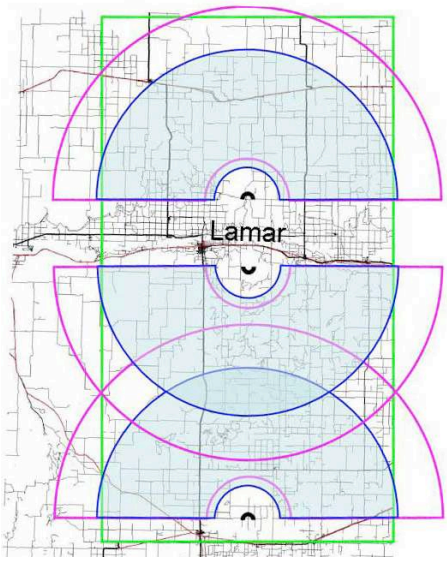

Figure 3.2: The surface detector array of Auger North will be located within the rectangular edges. The fields of view of the fluorescence detectors are marked with the semicircles [19].

altitude of 1420 m above sea level and, therefore, the distance to the shower maximum X_{max} is reduced. Hence, the shower is measured at an earlier stage of its development and the particle density is higher than at sea level. In addition to this advantages, the necessary infrastructure is available in Malargüe.

For the near future AMIGA, HEAT and the construction of a radio antenna array are planned to be built.

A northern site of the Pierre Auger Observatory is planned to be built in Lamar, Colorado, USA. With the completion of the northern site, the Pierre Auger Observatory will be the first air shower experiment, which is able to observe the whole hemisphere. The main focus of Auger North will be on the highest energies. Therefore, currently a surface detector array of 4000 stations is planned to be built, with a spacing between the stations of 1 mile = 1.609 km. This results in a surface of 10000 km^2, shown in Figure 3.2. Three fluorescence detectors, each with six telescopes, shall observe the air space above the array. A detailed design report of Auger North is in preparation.

3.1 Surface detector

The surface detector (SD) consists of 1600 water Cherenkov tanks, arranged in a hexagonal grid with a spacing of 1500 m. This array covers a surface of 3000 km^2. The design of the SD array is optimised for primary energies $E \geq 3 \cdot 10^{18}$ eV.

Each SD station consists of a cylindrical polyethylene tank with a diameter of 3.6 m and a height of 1.2 m. The Cherenkov tanks are filled with 12 t of highly pure water, as detection medium. Three photomultiplier tubes (PMTs) are symmetrically positioned in the tanks, with a distance of 1.2 m to each other. They are looking downwards into the water. A solar power system and a battery box allow the tanks to be self-sufficient. With a global positioning system (GPS) antenna the timing of an event and the position of each tank can be determined, which is important for a precise shower reconstruction. The communication and data transfer is ensured by a radio transceiver [20]. In Figure 3.3, the schematic design and a photo of a water Cherenkov tank are shown.

Secondary particles, entering an SD station, have a velocity higher than the speed of light in water. Thus, these charged particles, mainly electrons and muons, produce Cherenkov light while penetrating the water. This light is reflected by the white polyethylene layer which covers the tank's inside. The photomultipliers detect the light signal and convert it into a current pulse. The current signals of the anode and the last dynode are read out every 25 ns by a flash analogue to digital converter (FADC). Because of the good time resolution, the arrival time and the chronological sequence of the energy deposit can be measured. The arrival time allows the reconstruction of the arrival direction of the primary particle. Together with the energy information it is possible, to draw conclusions about the primary cosmic ray which initiates the extensive air shower.

The SD stations use the muon signals to calibrate themselves. For the calibration, the known energy distribution of muons is compared to the measured spectrum. The signals are measured in units of vertical equivalent muon (VEM), which corresponds to the light signal which a single muon produces, penetrating the tank vertically. $I_{\mathrm{VEM}}^{\mathrm{est}}$ is the corresponding photoelectric current.

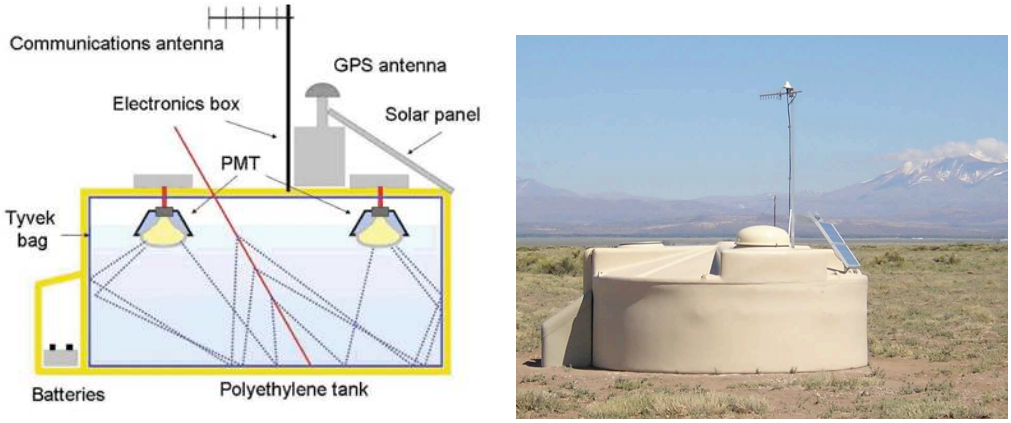

Figure 3.3: On the left: Schematic view of the surface detector station [21]. On the right: Photo of a surface detector station located in the Pampa Amarilla [22].

3.2 Fluorescence detector

The fluorescence detector (FD) consists of four ”eyes”, called Loma Amarilla, Coihueco, Los Leones and Los Morados. Each eye contains six fluorescence telescopes, each with a field of view of $30^\circ \times 30^\circ$, which results in a total field of view of $180^\circ \times 30^\circ$ for each telescope station.

Secondary particles, penetrating the atmosphere, excite nitrogen molecules. These in turn emit fluorescence light in the ultra violet range when falling back into their ground states. This light can be measured by the sensitive fluorescence telescopes. Because nitrogen particles are excited along the cascade, the longitudinal development of the shower can be observed. The amount of ultra violet light is proportional to the number of secondary particles and thus proportional to the energy of the primary cosmic ray. This allows for calorimetric measurements. At the shower maximum, the number of excited molecules also reaches its maximum and subsequently the energy attenuation is visible. Events with energies $E \geq 10^{17}$ eV produce enough light to be measured by the FD. This amount of light can only be measured, if it is very dark and no other light sources exist. Therefore, the measuring periods of fluorescence telescopes are limited to moonless nights, which leads to an duty cycle of only $\approx 12\%$.

In Figure 3.4, the design of a fluorescence telescope is shown. The light traverses through the diaphragm onto the segmented mirror, which focuses the light on the pixel camera. The camera consists of 440 pixels, each pixel being one photomultiplier tube.

3.3 Hybrid measurement

One of the main advantages of the Pierre Auger Observatory is the application of two independent detector techniques, the surface and the fluorescence detector. An event, detected by both detectors coincidentally, is called a hybrid event, like it is shown in Figure 3.5 on the left. On the right side of the figure, a measured hybrid event is shown,

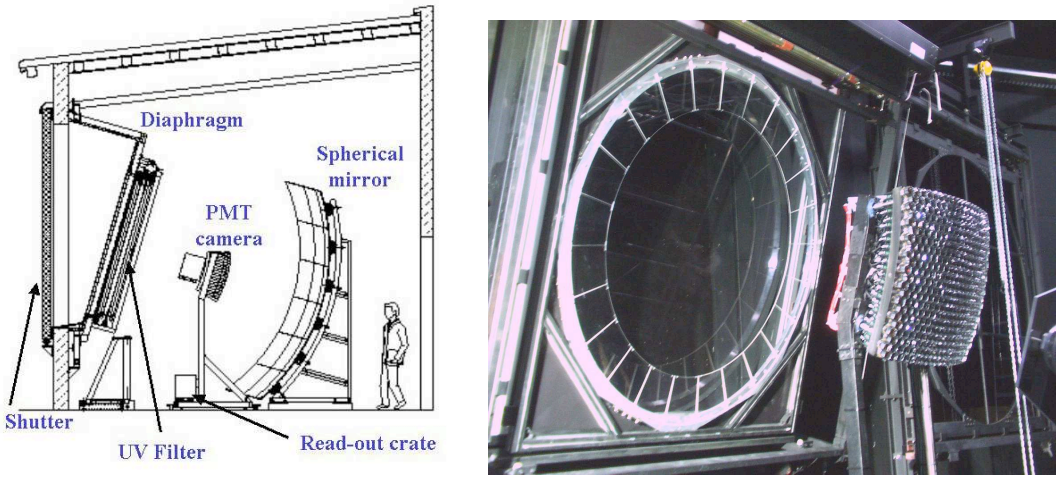

Figure 3.4: On the left: Schematic view of the assembly of a fluorescence telescope [23]. The light traverses through the diaphragm and hits the spherical mirror, which focuses the light on the pixel camera. On the right: The pixel camera of the fluorescence detector is consisting of 440 PMTs [24].

which is detected by all four fluorescence eyes and the surface detector.

Hybrid events allow for calibration and cross checks. The energy calibration of SD events is very complicated, because the shower is sampled only at one point during its development. This problem can be solved by hybrid events. The FD allows for a nearly calorimetric energy measurements and therefore the energy reconstruction is much easier. Hybrid events can be used to calibrate the SD signals with the reconstructed energy of the FD, both corresponding to the same event.

3.4 Radio detector

An extensive air shower, penetrating the atmosphere, emits radio waves. This radio emission is due to two different mechanisms, geomagnetic radiation and Cherenkov radiation.

Firstly, the charged secondary particles are influenced by the Earth's magnetic field. This leads to a separation into a negative and a positive particle fraction and a transversal charge transfer occurs. Because of this, dipole radiation can be measured. Another possible reason for geomagnetic radiation, is the movement of the charged particles on gyration circles due to the geomagnetic field. This circular motion results in synchrotron radiation.

A second reason for radio emissions is Cherenkov radiation. Cherenkov light is emitted, because the velocity of the secondary particles exceeds the speed of light in air. In a neutral shower, the radio signals of positively and negatively charged particles would compensate each other. But, by reason of the negative charge excess, caused by the recombination of positrons with electrons in the air, Cherenkov radiation in radio frequency is emitted in forward direction [27].

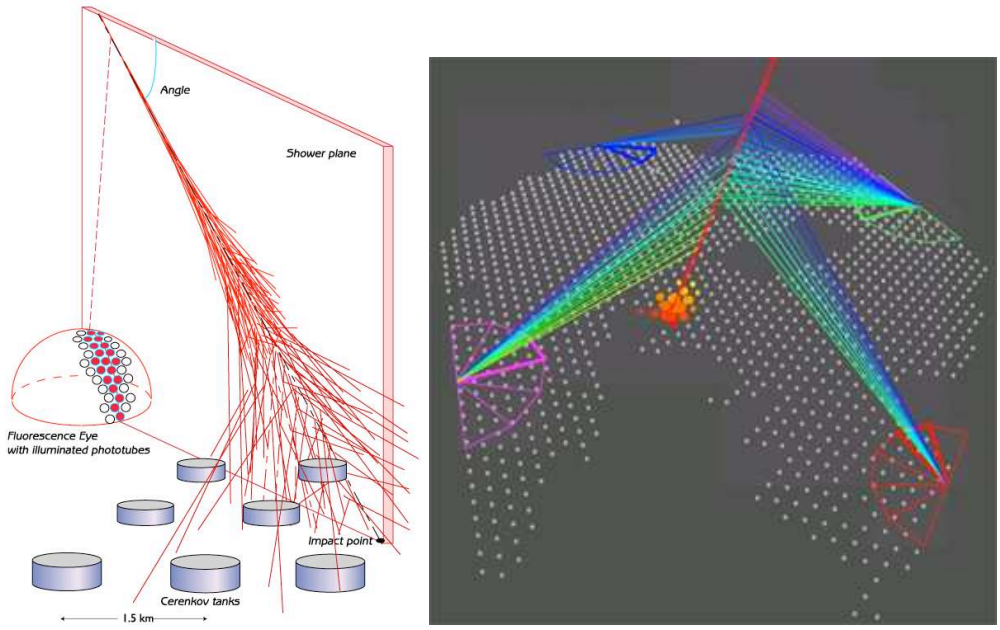

Figure 3.5: On the left: Schematic view of an event, detected by both the surface and the fluorescence detector [25]. On the right: Data event which is detected by all four eyes [26] and the surface detector array.

As radio emission is coherent, the amplitude of the measured signal is almost linearly related to the energy of the primary cosmic ray. This signal can be measured by radio antennas. Complementary to the fluorescence detector, a radio antenna array could observe the longitudinal development of an EAS. The radio detection system aims at measuring cosmic rays with energies beyond $E = 1$ EeV. Therefore, a test setup with different antenna prototypes is built, see Figure 3.6. The radio background around Malargüe, due to commercial radio and TV stations, is moderate and it is possible to filter out the remaining frequency background [28].

Figure 3.6: Different antenna prototypes, installed near Malargüe [29].

3.5 AMIGA and HEAT

The Auger Muons and Infill for the Ground Array, AMIGA, is an upgrade of the Pierre Auger Observatory. Firstly AMIGA is designed in order to record the energy spectrum in the region of the ”second knee” and the ”ankle”. This energy range, between these two bends in the energy spectrum, is supposed to be the transition of cosmic ray sources from galactic to extra galactic origins. Secondly the muon content of the extensive air shower will be determined with muon counters. The chemical composition of cosmic rays at energies above 10^{17} eV should provide a clue about their origin and will allow to investigate this hypothesis of transition.

AMIGA will consist of an infill array of 85 additional Cherenkov detectors. A 23.5 km^2 hexagonal surface detector array with a spacing of 750 m will be installed. Inside this infill array, a second smaller infill array is included, with a spacing of 433 m, covering an area of 5.9 km^2. The threshold energies of the infill arrays will be reduced to $10^{17.6}$ eV and 10^{17} eV, respectively. The Cherenkov detectors on a 750 m grid are installed already. The second infill array, with a spacing of 433 m, is under construction. The two hexagonal SD infill arrays are shown in Figure 3.7.

Next to each AMIGA surface detector station, a 40 m^2 muon counter will be buried in a depth of ≈ 2 m. It consists of 256 highly segmented scintillator strips. The light signal of the scintillators will be transmitted via wavelength shifting fibres to one of four 64-pixel multi-anode photomultipliers. The muon counters will be buried, to avoid the measurement of charged electromagnetic particles, that are stopped by the soil. Because the number of produced muons depends on the mass of the primary particle, it is possible to conclude from the number of counted muons to the type of primary cosmic ray. Another advantage of the muon content determination is to make the energy reconstruction more precise. The imprecise muon component in Monte Carlo simulations causes uncertainties in the energy determination by the surface detector, especially for zenith angles $\Theta > 60^\circ$ [30] [31].

The High Elevation Auger Telescopes, called HEAT, are an extension of the fluorescence telescopes and is under construction at the moment. HEAT is located next to the fluorescence detector Coihueco and will observe the sky above the AMIGA detector area. Because it will have a field of view from 30° to 58° above the horizon, the detectable energy range will be expanded down to 10^{17} eV. The signal strength of fluorescence photons at the air shower maximum is proportional to the primary energy and, therefore, cosmic rays at lower energies can only be detected, if the distance to the telescope is short. But for nearby air showers, the fluorescence detectors have to look up to higher altitudes, than for showers far away. Furthermore, the lower the primary energy, the higher is the altitude of the shower maximum [32]. The vertical field of view of HEAT is $4 \times 30^\circ$ and is marked in Figure 3.7.

The combination of AMIGA and HEAT will allow for a composition study, consisting of muon content determination and measurements of the atmospheric depth at the shower maximum, $X_{\max}$, in dependency on the energy. These two parameters are very sensitive to the mass of the primary cosmic ray. A simultaneous change of both parameters , detected by FD / HEAT and muon counters, would be a strong evidence for the transition from

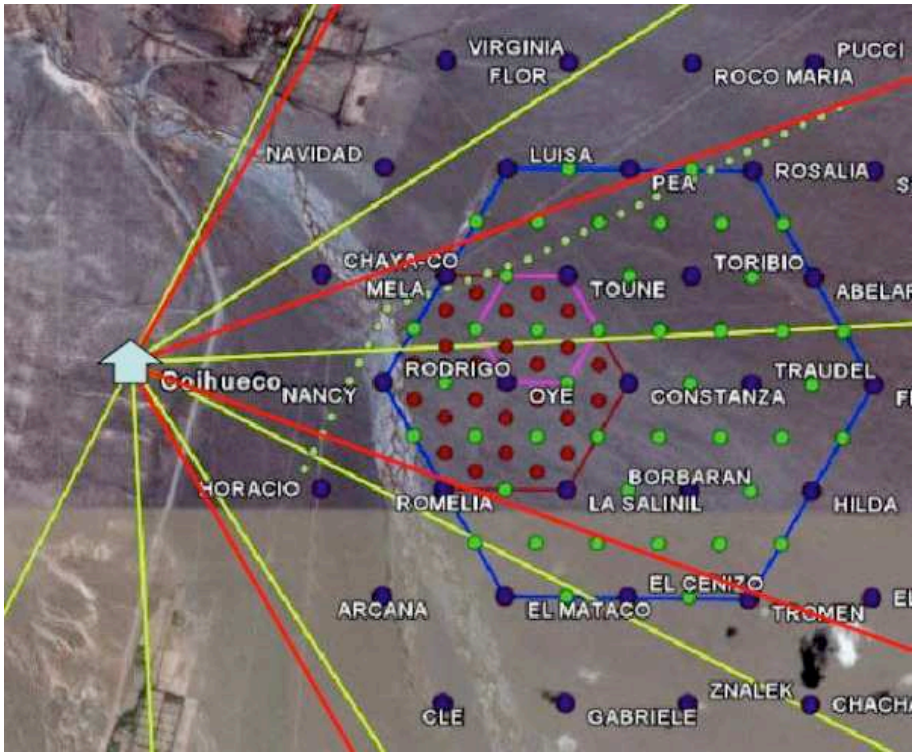

Figure 3.7: The green dots, inside the blue hexagon, illustrate the SD infill array with a surface of 23.5 km^2 and a spacing of 750 m. The second infill array has a surface of 5.9 km^2, with a spacing of 433 m. Next to the telescope station Coihueco, the HEAT telescope is located. The vertical field of view of each HEAT fluorescence telescope is marked by the red lines. The yellow lines illustrate the field of view of Coihueco. [19]

galactic to extragalactic cosmic rays in the energy region between the ”second knee” and the ”ankle”.

3.6 Weather

One of the scopes of this thesis is to investigate the influence of the weather on the constant intensity cut method results. Therefore the weather data of Malargüe and possible weather effects are discussed in this section.

The telescope station Los Leones (LL) provides weather data since January 01, 2004, the central laser facility (CLF) since June 22, 2004. Because the weather informations, obtained by the central laser facility, are more accurate, they are favoured for analyses. Only if no data of the CLF weather station is available, weather data of Los Leones is chosen. Weather data are recorded every 300 s = 5 min, except for the pressure, which is measured once per hour. In Figures 3.8 to 3.11 the temperature T, the humidity H, the pressure P and the density ρ of the whole year 2007. In order to see variations in smaller scale, these parameters are shown for the time period from July 23 to July 30, 2007 as well. The time scale is in days, related to the UTC time. The time in Malargüe is

UTC time minus 3 hours. Between January 1 and January 9 and between October 20 and November 14, 2007, no weather data is available, neither of the central laser facility, nor of Los Leones.

As expected in the southern hemisphere, the temperature T decreases from January to July and afterwards increases again. Also the daily fluctuations between day and night are visible, with a maximum at 4 pm and a minimum at 8 am. It becomes obvious, that the daily fluctuations of around 20° are higher than the seasonal fluctuation of 15°.

The relative humidity H is the ratio of the partial pressure of water vapour to the saturated partial pressure of water vapour at the same temperature. It fluctuates from around 30% to 85% daily, but is constant over the year. The humidity has its minimum at 4 pm, when the temperature has its maximum, because the humidity saturation increases with increasing temperature. Therefore the relative humidity decreases with higher temperatures, but the amount of water in the air does not change.

The pressure P shows no seasonal dependence, but daily fluctuations are visible. Each day the pressure has two maximum values, caused by the tide. The periodical change of the Earth's gravitational field, caused by the combined attraction of Earth and Moon, influences the weight of the air column and therefore the air pressure. A temperature dependence is not visible.

Because the density ρ is not given by the weather data, it has to be calculated from the existing weather parameters. A change in temperature T or pressure P results in a change of the air density ρ, which can be calculated from T and P, measured at ground level:

$$\rho \simeq \overline{\rho}\left(1 - \frac{T-\overline{T}}{\overline{T}} + \frac{P-\overline{P}}{\overline{P}}\right), \tag{3.1}$$

with the reference values $\overline{T} = 280\ \mathrm{K} = 6.75\ ^{\circ}\mathrm{C}$, the average night temperature, $\overline{P} = 860$ hPa, the average pressure and the average ground density $\overline{\rho} \simeq 1.07 \cdot 10^{-3} \frac{\mathrm{g}}{\mathrm{cm}^3}$ of Malarüge [33]. The density ρ decreases with increasing temperature, in seasonal as well as daily developing.

Since the central laser facility only records ground data, the atmospheric profile has been studied with balloon measurements above the surface detector array. With this balloon measurements a model of the atmospheric depth $X(h)$ was developed [34], which can be included to air shower simulations. The atmospheric depth $X(h)$ influences the age of a shower at ground level, the density ρ affects the Molière radius r_M. Both factors have an impact on the particle density at the detector level and therefore on the measured signal [33].

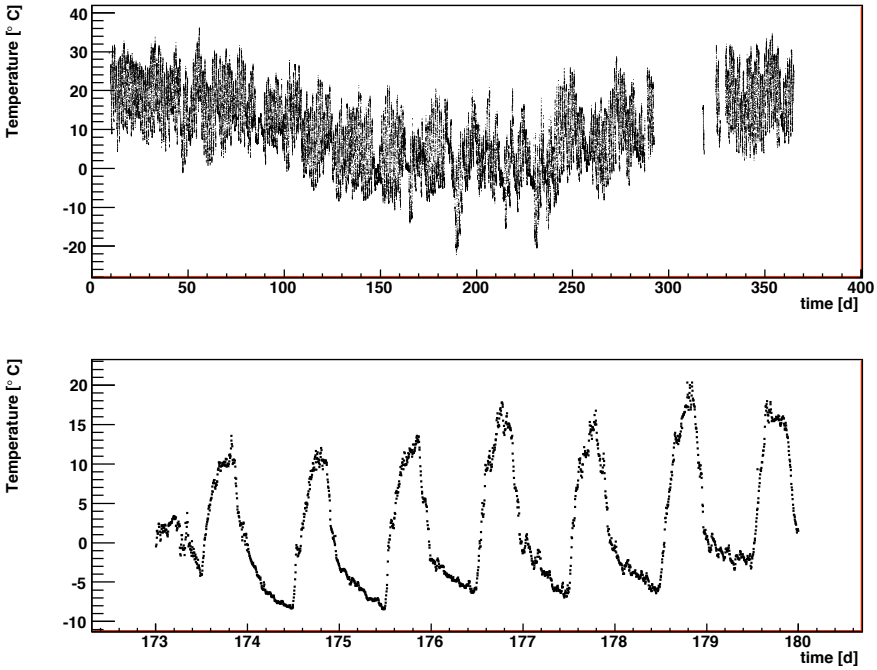

Figure 3.8: The temperature profile of 2007 is shown in the upper plot, the lower plot shows the temperature T from July 23 to July 30, 2007

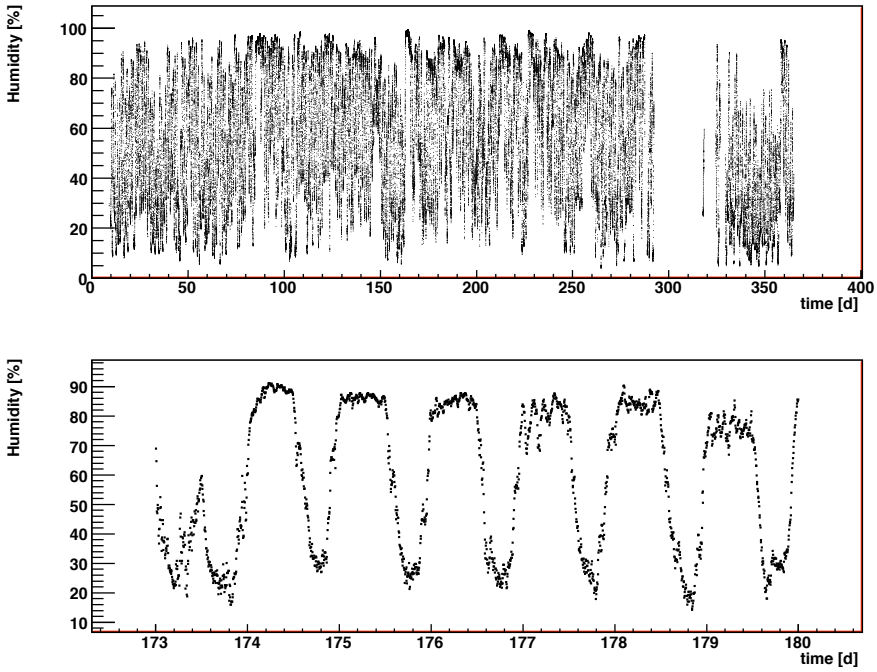

Figure 3.9: The humidity profile of 2007 is shown in the upper plot, the lower plot shows the humidity H from July 23 to July 30, 2007

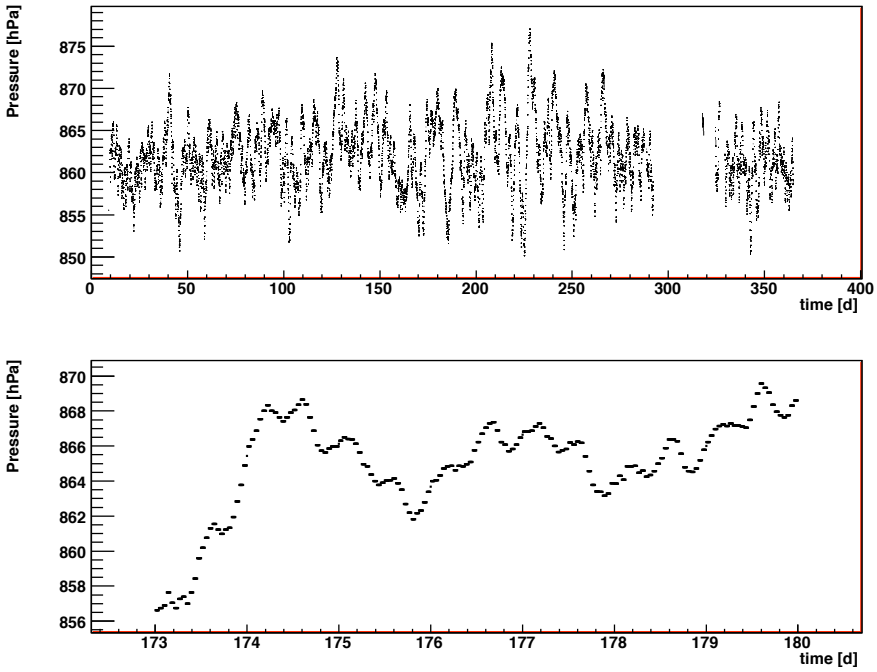

Figure 3.10: The pressure profile of 2007 is shown in the upper plot, the lower plot shows the pressure P from July 23 to July 30, 2007

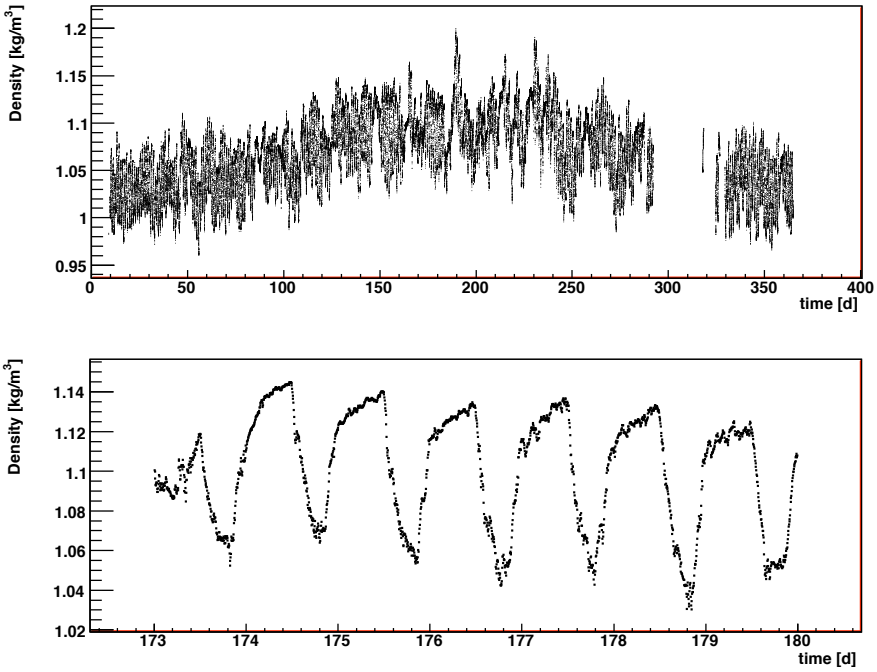

Figure 3.11: The density profile of 2007 is shown in the upper plot, the lower plot shows the density ρ from July 23 to July 30, 2007. The density is calculated from Equation 3.1

Chapter 4

Surface Detector

Because in this thesis only surface detector events are analysed, SD calibration, trigger levels and the SD event reconstruction are described in more detail in the following sections.

4.1 SD Calibration and Monitoring

The aim of the calibration is to achieve equal pulse height histograms for the three PMTs in a station. It is necessary that all stations of the array are calibrated uniformly, in order to reconstruct cosmic ray showers. Because the signal of each tank depends on many parameters like the water quality, the liner reflectivity, the coupling between PMT and water and the PMT amplification factor, it is necessary to perform the calibration for each PMT of each station. Furthermore, this calibration has to be repeated time and again, to correct for temporal changes of the parameters.

In order to calibrate the PMT signals, the spectrum of atmospheric muons is used. The charge deposit of muons is proportional to their track length, as muons are not stopped in the tank. The reference signal is induced by a vertical and central through-going (VCT) muon. Therefore signals are measured in units of vertical equivalent muons (VEM). Since not all background muons are vertical and the surface detector stations are not able to distinguish between vertical and inclined muons, vertical and central through-going muons have been measured by a reference surface detector station, equipped with additional scintillators [35]. Due to atmospheric muons, the charge distributions of the PMTs exhibit a muon peak, related to the reference unit VEM. The distribution for each individual PMT has a peak at (1.03 ± 0.02) VEM, because only a fraction of light is deposited in its proximity. For the sum of all three PMT signals of a single station, the charge distribution peaks at (1.09 ± 0.02) VEM, since the total deposited signal is measured.

When commissioning a surface detector station, the high voltage of the PMTs is adjusted until the signal rate reaches 100 Hz at 150 ADC channels above baseline (measured charge, without detecting a particle). But after the PMTs' end-to-end gains are set up, they drift away from this point, because of their temperature responses. Therefore, the gains have to be calibrated all the time. The VEM calibration procedure is performed in three steps:

1. The end-to-end gain of each PMTs has to be calibrated such, that the pulse height distribution has its peak $I_{\mathrm{VEM}}^{\mathrm{peak}}$ at ADC channel 50. Therefore, the sum of the three PMTs has a peak at channel 150, as shown in Figure 4.1, on the right.

2. After setting the value, the peak $I_{\mathrm{VEM}}^{\mathrm{peak}}$, is constantly adjusted, in order to compensate for drifts.

3. The corresponding charge $Q_{\mathrm{VEM}}^{\mathrm{peak}}$ has to be determined from the charge histogram, in order to convert the integrated signals to the unit VEM. The charge distribution is shown in Figure 4.1, on the left.

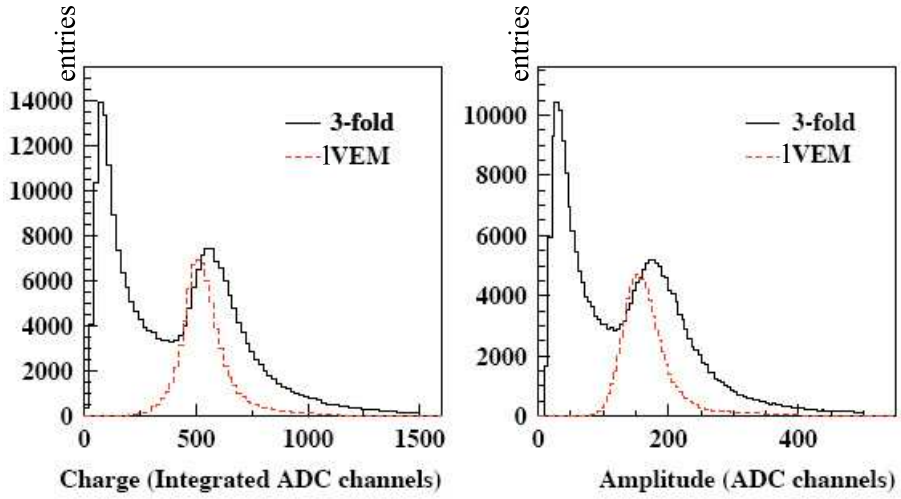

Figure 4.1: Charge (left) and pulse height (right) histograms of a three PMT coincidence measurement (solid line). The first peak is due to low energy particles from air showers, the second peak is caused by atmospheric muons. The dashed line illustrates the charge distribution due to vertical and central through-going muons, measured with the reference tank [36].

The charge $I_{\mathrm{VEM}}^{\mathrm{peak}}$ could not be determined on-line, because the processing time would increase the dead time of the surface stations enormously. Therefore, the trigger levels are set with the estimate value $I_{\mathrm{VEM}}^{\mathrm{est}}$, requiring the "calibration trigger". To fulfill this trigger, the total signal of all three PMTs has to be above $1.75 I_{\mathrm{VEM}}^{\mathrm{est}}$ for a rate of 110 Hz. Each PMT of its own has to be above $2.5 I_{\mathrm{VEM}}^{\mathrm{est}}$ for a lower rate of 70 Hz. If a measured PMT signal does not satisfy these requirements, it has to be adjusted in an iterative procedure.

To evaluate the charge corresponding to 1 VEM, a signal peaking exactly at 1 VEM is divided by 1.75. The uncertainty of 1 VEM is 2%.

4.2 SD trigger system

The SD trigger system is designed to allow the data acquisition of a wide range of primary particle energies. For energies larger than $E = 10^{19}$ eV, full efficiency is reached, for both vertical and inclined showers. The trigger system should distinguish between real events and background. To satisfy these requirements, a hierarchical trigger system has been developed. It consists of the two local triggers T1 and T2, the event trigger T3 and T4 and T5, which are applied off-line. In this section the different trigger levels [37] [38] are explained.

4.2.1 Local triggers T1 and T2

The first and the second trigger levels T1 and T2 are processed by the SD station's electronics and, therefore, they are called local triggers. Their aim is to separate possible events from backgound noise. With this triggers the data is reduced to important signals before it is sent to the central data acquisition system (CDAS) on the campus in Malargüe.

The T1 trigger contains two trigger modes. The Time over Threshold (ToT) trigger, the Single Threshold (ST) trigger or both have to be fulfilled. At least two of the three PMTs have to measure a coincident current above $0.2 \cdot I^{\text{est}}_{\text{VEM}}$ in at least 13 time bins within a 120 bin window, to fulfill the ToT trigger. One time bin corresponds to the 25 ns readout period of the FADC. This trigger criteria is very efficient to choose small but spread signals, caused by low energy events or measured by stations with a large distance to a high energy shower core. The ToT trigger rate of 1.6 Hz is not sensitive to the muonic component, since the muon signals are too short ($t < 200$ ns). Therefore, single muon signals are ignored by this trigger. The ST trigger requires a three PMT coincidence above the threshold current of $1.75 \cdot I^{\text{est}}_{\text{VEM}}$ in one single time bin. Short signals, corresponding to the muonic component of horizontal showers, are chosen by this trigger criteria, but also much noise. Therefore, the trigger rate is with 100 Hz much higher, than the ToT rate.

Signals passing the ToT trigger, are automatically promoted to T2. In contrast ST triggered signals have to cross a higher current threshold of $3.2 \cdot I^{\text{est}}_{\text{VEM}}$ in coincidence of three PMTs, to select only signals caused by an EAS. With the T2 trigger, the trigger rate is reduced to 20%. The T2 triggered events are also used to calculate the exposure of the array and to monitor the SD array performance. Only T2 triggered signals are transferred to the CDAS for the next trigger level T3.

For all T2 triggered stations of each event, 13 histograms are send to the CDAS. In Figure 4.2 the raw histograms of station 1640 of event 20082140018 are shown.

4.2.2 Event trigger T3

The aim of the T3 trigger level is to select the real physical events from the transferred data. T3 distinguishes between ToT and T2 triggered signals.

Three coincidently ToT triggered tanks, located near to each other, are required by the so-called 3ToT trigger. To achieve 3ToT, one of the triggered stations has to have at least one closest and one second closest triggered tank in its neighbourhood. As the

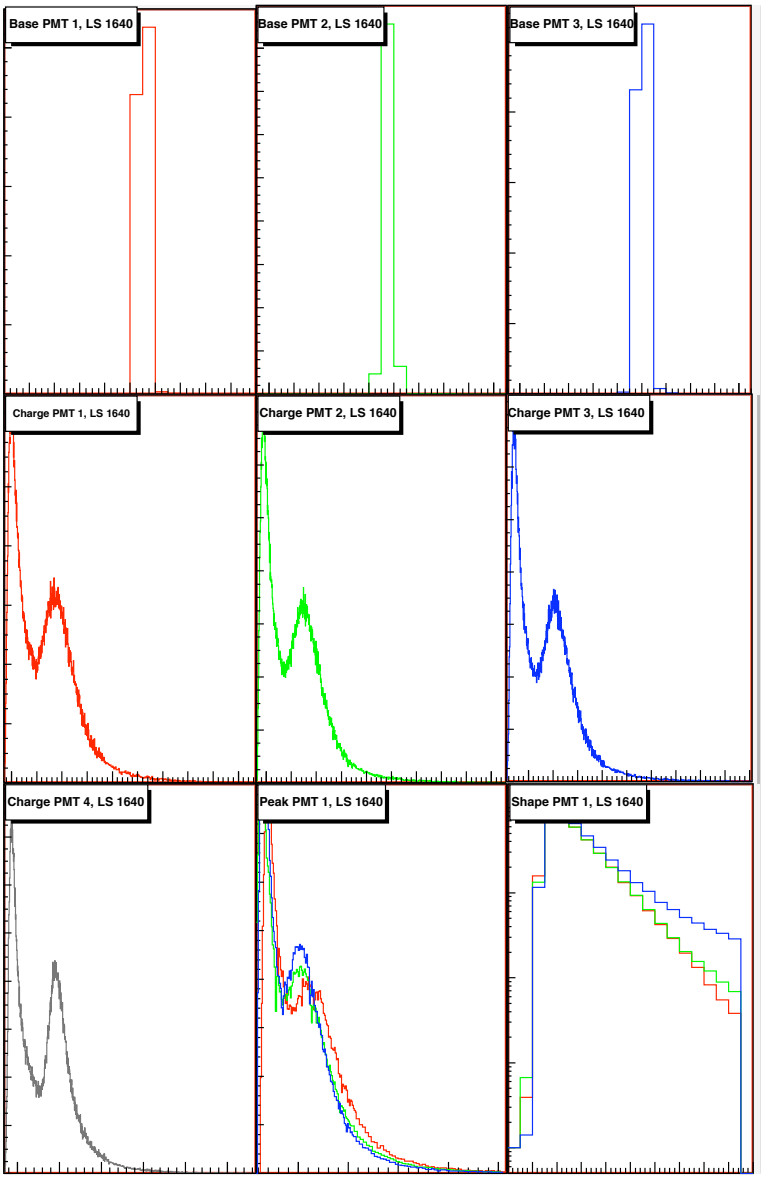

Figure 4.2: Raw historgams of station 1640 of event 200821400018. On the top: The baseline histograms of the dynode signals of all three PMTs. In the middle: Charge histogram of each PMT. At the bottem left: The sum of the three charge histograms. At the bottem middle: Pulse height histograms of the three PMTs. At the bottem right: Average pulse shape of the three PMTs.

ToT triggered events have a very low background, in comparison to ST, this 3ToT trigger selects 90% of the physical events that are mainly vertical showers.

T2 triggered stations have to satisfy the so-called 3C1 trigger. This trigger requires a coincidence measurement of four triggered tanks at moderate distances to each other. One of the four tanks can be located up to 6 km away from the others within an adequate time window. The 3C1 trigger is very sensitive to horizontal showers with triggered stations spread over larger areas.

All T3 triggered events are stored and then processed off-line at the trigger levels T4 and T5.

4.2.3 Physical trigger T4

To select only real physical events from the stored T3 data, the T4 trigger level is performed. This physical trigger also consists of two different trigger conditions, the 3ToT T4 and the 4C1 trigger. The 3ToT T4 trigger requires a compact 3ToT trigger. Less than 5% of the showers with zenith angles $\Theta \leq 60^\circ$ are discarded by this trigger. The 4C1 trigger chooses events with at least three triggered stations within the six nearest neighbours. This trigger ensures the selection of the shower events, discarded by the 3Tot T4 trigger. For both trigger methods, the trigger time compatibility with the speed of light is required. In Figure 4.3, the zenith angle and energy distributions of both trigger conditions, 3ToT T4 and 4C1, are illustrated. It becomes obvious, that the major fraction of events is triggered by the 3ToT T4 trigger, whereas horizontal events are triggered by the 4C1 trigger more often. Only 3ToT and 4C1 triggered events with zenith angles $\Theta \leq 60^\circ$ are officially called T4 triggered events.

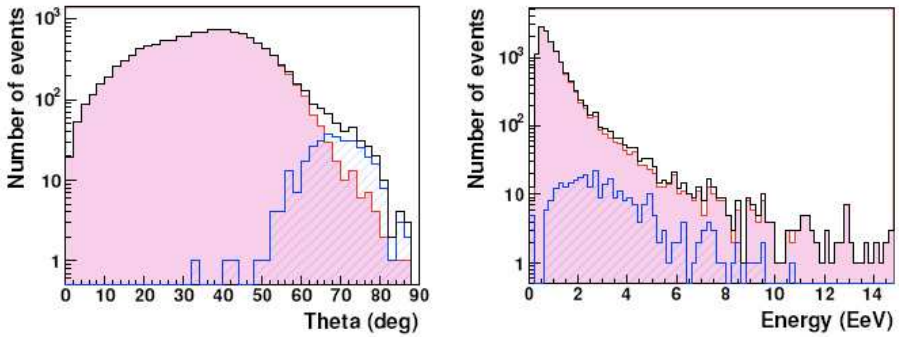

Figure 4.3: The zenith angle (left) and the energy (right) distribution of T4 triggered events. 3ToT T4 triggered events are illustrated by the red shaded fraction, 4C1 events by the blue dashed area. Events passing both T4 triggers are counted as 3ToT T4 events [37].

Tanks that are triggered within the time window of an extensive air shower, but originate from atmospheric muons or background radiation, are called accidental. The following method is performed to remove those tanks from the triggered events. A triangle of the three highest signals, called the seed, is used to define the shower front of the event. Stations, that do not agree with the time development of the shower front, are removed.

Isolated tanks without a triggered neighbour in a distance of $d = 1800$ m or with less than two triggered neighbours in a distance of $d = 5000$ m are also neglected.

4.2.4 Quality trigger T5

The main purpose of the last trigger level is to select only events, that can be reconstructed accurate in energy and direction. Events located close to an array border, are often reconstructed incorrect, because a part of the shower is possibly lost. These events should be rejected by the quality trigger T5. Many studies have been performed to find a trigger, that separates the defective events without causing a systematical effect itself. The most common T5 triggers are the strict-T5 and the ICRC T5 triggers. The strict-T5 trigger requires an active unitary cell, i.e. the station with the highest signal has to be surrounded by six active stations. To fulfill the ICRC T5 trigger, the central station has to be surrounded by five active stations and the core has to be located within an active triangle of stations. Both trigger methods avoid border effects. The trigger requirements are shown in Figure 4.4.

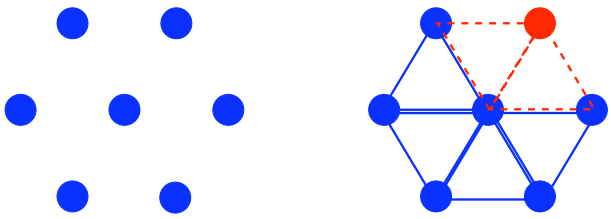

Figure 4.4: On the left: The strict-T5 trigger requires an active unitary cell. The stations are depicted by full dots. On the right: The ICRC-T5 trigger requires the central station to be surrounded by five of the six closest neighbours. In addition, the core has to be inside an active triangle (solid lines) and not inside an inactive triangle (dashed lines).

4.2.5 Trigger probability

The signals, detected by the surface detector stations, are affected by many different influences, e.g. shower-to-shower fluctuations, the number of produced photoelectrons and electrical noise. Therefore, the measured signals are overestimated or underestimated with respect to the expected signal. Because underestimated events are often not triggered, the event signal is shifted to higher values, as it is visible in Figure 4.5 [38].

Therefore, it is meaningful to discuss the trigger probability, before discussing the reconstruction. The triggered stations are sorted into bins of $S(1000)$ and Θ to calculate the experimental trigger probability

$$P_{\mathrm{exp}}(S) = \frac{N_{T+}(S)}{N_{\mathrm{ON}}(S)}. \tag{4.1}$$

$N_{T^+}(S)$ is the number of triggered stations with an expected signal S and $N_{\mathrm{ON}}(S)$ is the total number of active stations, both within a chosen signal bin. From the trigger probability the lateral trigger probability (LTP) can be calculated:

$$LTP(r) = P(LDF(r)), \tag{4.2}$$

with the lateral distribution function (LDF) in dependence on the shower axis distance r. In Figure 4.5, on the right, the lateral trigger probability LTP(r) is plotted for $S(1000) =$ 3 VEM, 10 VEM and 30 VEM and the zenith angle $\Theta = 45°$ and $0°$, respectively. The probability to trigger a station increases with the signal size increasing, the zenith angle Θ decreasing and decreasing shower axis distance r. This result confirms the expectation, that events with a high signal, a small zenith angle and a small distance to the shower axis are triggered rather than lateral events with a small signal and a large shower axis distance.

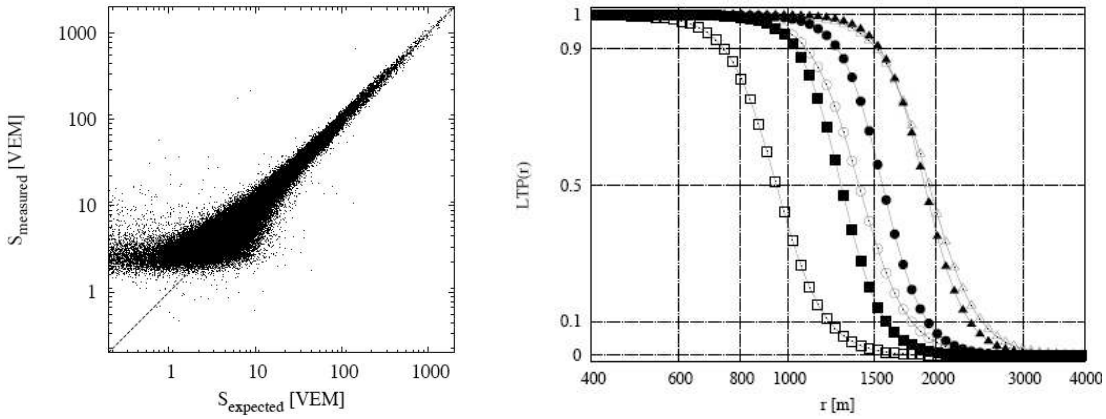

Figure 4.5: On the left: The measured signal S_{measured} is plotted versus the expected signal S_{expected}. Especially for low signals the triggered signals are shifted to higher values. On the right: The LTP(r) is plotted for $S(1000) = 3$ VEM, 10 VEM and 30 VEM (boxes, circles and triangles, respectively) and zenith angle $\Theta = 45°$ and $0°$ (filled and unfilled symbols) [38].

4.2.6 Acceptance

Only events with an energy $E \geq 3.0$ EeV and a zenith angle $\Theta \leq 60.0°$ achieve full acceptance. Below these limits, the probability to detect an event depends on the zenith angle Θ and the distance d between the shower axis and the station with the highest signal. Especially the number of horizontal events decreases with the energy decreasing. For full acceptance, the zenith angle distribution is proportional to $\sin\Theta\cos\Theta$. This distribution is shifted towards smaller angles for events with energies below $E = 3.0$ EeV, since the track through the atmosphere is longer. The Θ distribution for all events is shown in Figure 4.6, the one for full acceptance events is shown in Figure 5.2.

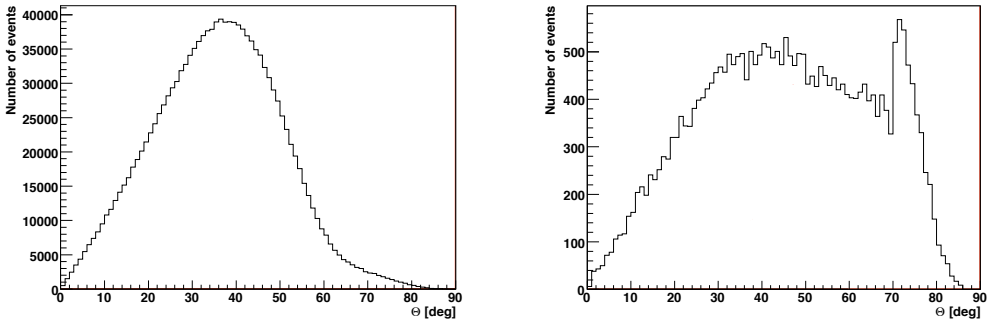

Figure 4.6: On the left: The Θ distribution for all events. It is visible, that the distribution is shifted towards smaller angles. On the right: The Θ distribution for events achieving full acceptance is proportional to $\sin\Theta\cos\Theta$. The peak at 71° is due to a change of reconstruction method.

Since the data aquisition started January 1, 2004, the surface detector measured more than 1.5 Mio. events, 20000 events of the whole data set achieve full acceptance. For this analyses only events are used, that fulfill these acceptance limits.

4.3 SD event reconstruction

Stations, that are belonging to an event and satisfying all trigger requirements, are called selected stations. These stations are used to reconstruct the arrival direction and the energy of the primary cosmic ray. From the curvature informations about the primary particle's mass are obtained.

The signal S and the time t measured and the positions x and y of the stations are necessary for the reconstruction. The position of all surface detectors are determined by the GPS system with an accuracy of 1 m. The time resolution of each selected stations is influenced by the uncertainty of the FADC trace's starting point (7 ns) and, additionally, by the uncertainty of the time synchronisation, performed by the GPS system. This leads to a total time resolution of 10 ns.

In the following three sections, the two different reconstruction softwares are introduced and both the angular and the energy reconstruction methods are described.

4.3.1 CDAS and $\overline{\text{Off}}\underline{\text{line}}$

Two different reconstruction softwares are available, called CDAS and $\overline{\text{Off}}\underline{\text{line}}$. $\overline{\text{Off}}\underline{\text{line}}$, the more common reconstruction code, is able to reconstruct both surface detector and fluorescence detector events and consequently hybrid events, too. In this analysis the CDAS software is used, which only reconstructs SD events. For each day a ROOT file with raw data of all SD T4 events exists. This data is reconstructed with the CDAS code. Furthermore the HERALD file is produced with CDAS, containing all reconstructed

T4 events. For each event 39 reconstructed properties are listed, e.g. the event-id, the reconstructed angles Θ and ϕ, the core coordinates x_{core} and y_{core} and different energy reconstructions [39]. The reconstructed data of the HERALD file is used for anisotropy studies, like the published studies of the AGN search.

The reconstructions differ marginally from each other. A comparison of both softwares is described in [40].

4.3.2 Angular reconstruction

The direction of a primary cosmic ray is described by the zenith angle Θ and the azimuth angle ϕ. To determine Θ and ϕ, the signals of each selected station i, its positions x_i and y_i and the arrival time t_i are required.

The easiest assumption, to reconstruct the direction, is a plane shower front, given by the three stations with the highest signals. In order to consider the curvature of the shower front, the factor $d_i^2/(2Rc)$ is added, with the distance d_i between the surface station i and the shower axis in the shower plane and the curvature R, variating with the position at ground. In Figure 4.7 the geometrical relation between the plane and the spherical shower front is illustrated. The time difference Δt_i between the measured arrival time t_i and the expected arrival time of the spherical shower front, can be calculated as follows:

$$\begin{aligned} \Delta t_i &= t_i - \left(t_{\text{plane}} + \frac{d_i^2}{2Rc} \right) \\ &= t_i - \left(T_0 - \frac{u(x_i - x_{\text{core}}) + v(y_i - y_{\text{core}})}{c} + \frac{d_i^2}{2Rc} \right), \end{aligned} \tag{4.3}$$

with the time T_0, when the shower hits the ground, the shower direction cosines $u = \sin\Theta\cos\phi$ and $v = \sin\Theta\sin\phi$, the core coordinates x_{core} and y_{core} and the speed of light c [41]. The barycentre of the positions of all selected stations, weighted with the square root of their signal sizes, defines the core position with a precision of 150 m.

The angles Θ and ϕ are determined by minimising $\chi^2 = \sum_i (\Delta t_i)^2/\sigma_{t_i}^2$, with the uncertainty σ_{t_i} of the arrival time t_i. The uncertainty $\sigma_{t_i} = (22 + 0.03 \cdot r)$ ns increases with increasing distance r between station and shower core [41]. The resulting angles Θ and ϕ have an uncertainty of 1.8° for events with energies below $E = 3$ EeV, which decreases to 1.2° for energies above $E = 3$ EeV.

4.3.3 Energy reconstruction

A primary particle, interacting with the atmosphere, initiates an extensive air shower of secondary particles. Their number is roughly correlated to the energy of the primary cosmic ray. The secondary particles come down to the Earth forming a spherical shower front. The curvature of the shower front is an indication of the primary particle's mass, since a heavier primary particle interacts earlier in the atmosphere and results in a shallow shower front whereas the shower front originating from a lighter particle is bent stronger. After the shower maximum X_{max}, the number of particles decreases. Obviously, vertical

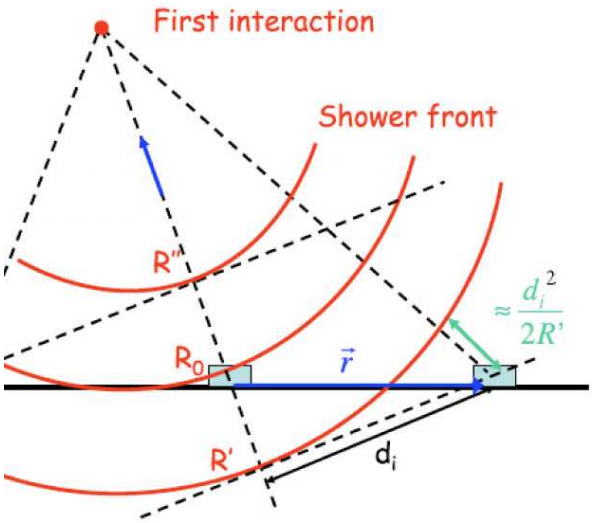

Figure 4.7: Plane versus spherical shower front. It becomes obvious that the curvature R depends on the position at ground [42].

showers are younger, when they reach the ground, than inclined showers. But also particles of a single shower reach the ground at different stages of age. The left SD station, illustrated in Figure 4.7, detects secondary particles earlier than the right station. Therefore, signals, measured with equal shower axis distances d, behave in a different way. The signals are corrected for this effect, called forward-backward asymmetry.

When the extensive air shower reaches the ground, only a small fraction of the particles is detected by the surface detector stations. The lateral dependence of the measured signals on the distance to the shower axis is described by the lateral distribution function (LDF), where the signals of the SD stations are plotted versus their distance d to the shower axis. $f_{\mathrm{LDF}}(d)$ is a parametrisation of the shape normalised to $S(1000)$:

$$S(d) = S(1000) \cdot f_{\mathrm{LDF}}(d), \tag{4.4}$$

with the signal $S(1000)$ at a distance $d = 1000$ m. $S(1000)$ is effectively independent of the primary particle's mass and shower fluctuations on $S(1000)$ and, therefore, it is a good estimator for the primary energy.

CDAS provides different lateral distribution functions, like the log-log parabola, the NKG-function and the Havera Park function. The log-log parabola has been developed in consideration of Monte Carlo simulations and has been tested with Auger data:

$$S(d) = S_{1000} \times \begin{cases} \left(\frac{d}{1000\,\mathrm{m}}\right)^{\beta} \times \left(\frac{d}{1000\,\mathrm{m}}\right)^{2\cdot\gamma\cdot\lg\left(\frac{300\,\mathrm{m}}{1000\,\mathrm{m}}\right)} \times \left(\frac{300\,\mathrm{m}}{1000\,\mathrm{m}}\right)^{-\gamma\cdot\lg\left(\frac{300\,\mathrm{m}}{1000\,\mathrm{m}}\right)} & d < 300\,\mathrm{m} \\ \left(\frac{d}{1000\,\mathrm{m}}\right)^{\beta+\gamma\cdot\lg\left(\frac{d}{1000\,\mathrm{m}}\right)} & d > 300\,\mathrm{m} \end{cases}, \tag{4.5}$$

with the uncertainty $\sigma_S(\Theta)$ [43] of the signal $S(r)$:

$$\sigma_S(\Theta) = (0.32 + 0.42\sec\Theta)\sqrt{S}. \tag{4.6}$$

In the standard reconstruction, the slope parameter β is fitted to the data points, if enough signals are triggered by a shower. Otherwise, β is calculated from the following equation [44]:

$$\beta = 0.7 \cdot \arctan(9.0 \cdot (0.65 - \cos\Theta)) - 3.0. \tag{4.7}$$

The NKG-function is based on Equation 2.2, developed by J. Nishimura, K. Kamata and K. Greisen, which describes the lateral distribution of the electron density [17]. It is the standard LDF parametrisation of the Offline reconstruction software:

$$S(r) = S_{1000} \times \left(\frac{r}{1000\,\mathrm{m}}\right)^{\beta} \times \left(\frac{r+700\,\mathrm{m}}{1700\,\mathrm{m}}\right)^{\beta+\gamma}. \tag{4.8}$$

Since the log-log parabola is the standard energy reconstruction in CDAS, it is also used in this analysis, to fit the lateral distribution. In Figure 4.8, the signal sizes and the fitted LDF of event 200821400018 are shown.

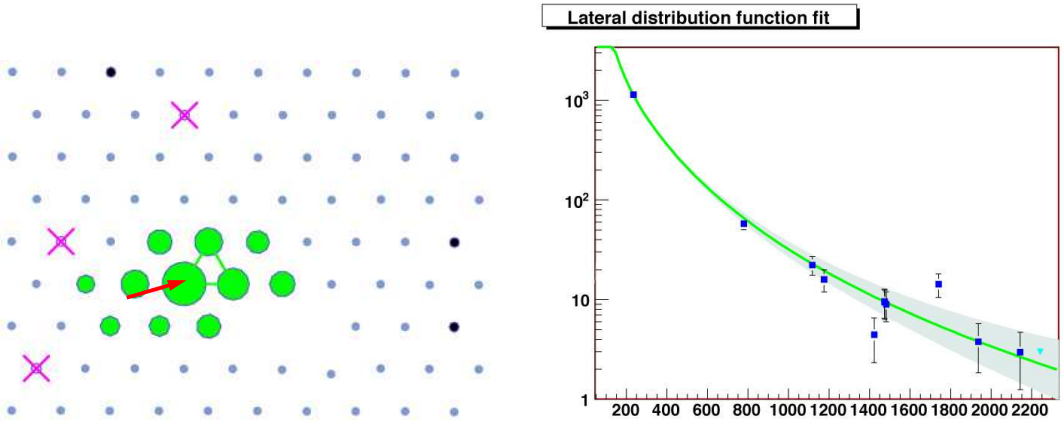

Figure 4.8: Both pictures, taken from the CDAS Event Display, show event 200821400018, with a reconstructed energy of $E = 12.03$ EeV, a zenith angle of $\Theta = 51.5°$ and an azimuth angle of $\phi = -166.4°$. On the left, the triggered surface detector stations are shown. The size of their circles is proportional to their measured signal. The three central stations, that are connected with the triangle, are the so-called ”seed” of this event. Surface detector tanks, marked by a cross, are accidental, and black coloured tanks are not active. The arrow marks the azimuth direction angle of the extensive air shower. On the right, the resulting LDF (solid line) is shown. The triggered stations (rectangles) are plotted in dependence on the distance to the shower axis. Silent stations (triangle) are active stations, that measure no signal. These stations are considered in the LDF fit.

From the LDF, the signal $S(1000)$ at a distance to the shower axis of $d = 1000$ m can be determined. $S(1000)$ depends on the energy E and the zenith angle Θ. After determining $S(1000)$, the energy information has to be extracted. In order to determine the energy estimator $S_{38°}(E)$, the constant intensity cut is performed, as described in

Chapter 5. $S_{38^\circ}(E)$ is the signal of a surface detector event which would be measured at a distance $d = 1000$ m and a zenith angle $\Theta = 38^\circ$. Because $\Theta = 38^\circ$ is the median zenith angle of the Θ distribution for all events achieving full acceptance, $S_{38^\circ}(E)$ is selected as a reference value. After determining $S_{38^\circ}(E)$, hybrid events can be used to relate the energy E, measured by the fluorescence detector, to the calculated energy estimator $S_{38^\circ}(E)$ of the surface detector. In Figure 4.9, the $S_{38^\circ}(E)$ values of the surface detector are plotted against the energy measured by the fluorescence detectors in a double logarithmic plot. A strong correlation between the $S_{38^\circ}(E)$ values and the FD energy E_{FD} of hybrid events is visible and the data points can be fitted with the following power law:

$$E_{\mathrm{FD}} = p \cdot \left(S_{38^\circ}(E_{\mathrm{SD}})\right)^q, \tag{4.9}$$

with the parameters $p = (1.49 \pm 0.06(\mathrm{stat.}) \pm 0.12(\mathrm{syst.})) \cdot 10^{17}\mathrm{eV}$ and $q = 1.08 \pm 0.01(\mathrm{stat.}) \pm 0.04(\mathrm{syst.})$ [45] [46].

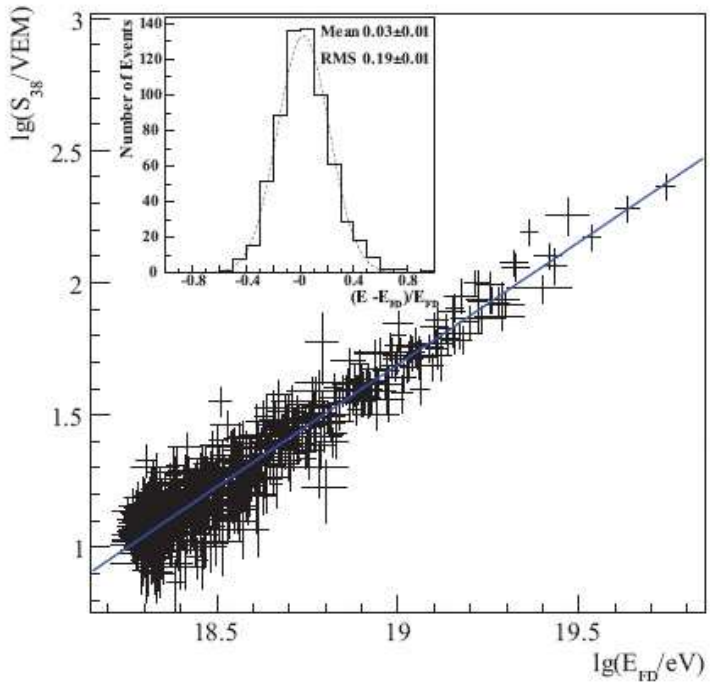

Figure 4.9: Hybrid events: Correlation between $\lg S_{38^\circ}(E)$ of the surface detector measurements and $\lg E$ measured by the fluorescence detector. The power law $E_{\mathrm{FD}} = p \cdot (S_{38^\circ}(E_{\mathrm{SD}}))^q$ is the best fit to the data points [46].

Chapter 5

Constant intensity cut method

One of the goals of the Pierre Auger Observatory is to reconstruct the energy of the primary cosmic particles. Because this energy cannot be measured directly, it has to be reconstructed from the measured properties of the extensive air showers. The signal at a distance of 1000 m from the shower axis, called $S(1000)$, is linked to the energy of surface detector measurements. The stage of development of the air shower is dependent on the penetrated atmospheric depth. Because the track length through the atmosphere increases with growing Θ, the surface detector measures different signals $S(1000)$ for primary particles with the same energy, depending on the zenith angle Θ. Hence, the signal $S(1000)$ is a function of the energy E and the zenith angle Θ. In order to relate $S(1000)$ to the energy and to correct for the Θ dependence the constant intensity cut (CIC) method is performed. It was developed by the MIT group in 1961 [47].

The flux of primary cosmic ray particles decreases with increasing energy. The differential flux is:

$$\frac{dI}{dE} \propto E^{-\gamma}, \tag{5.1}$$

with the spectral index γ.

The main assumption of the constant intensity cut method is that the particles are arriving isotropically from the cosmos and hence the flux does not depend on the arrival direction. Because the intensity is the time averaged energy flux, it is also isotropic.

Because the Pierre Auger Observatory comprises a hybrid detector, it is possible to calibrate the energy of the SD events in consideration of hybrid data. The signal $S(1000)$ is determined from the LDF of a surface detector event. $S(1000)$ is linked to the primary energy E of an UHECR, but it also depends on the zenith angle Θ. To separate the energy information from $S(1000)$, the constant intensity cut method is used. Afterwards hybrid events can be used to relate the energy E, measured by the fluorescence detector, to the calculated energy estimator S_{38° of the surface detector.

In Section 5.2, the ansatz of the constant intensity cut method is described. Because the constant intensity cut method was never performed like this in Auger before, in Section 5.4 the focus is on the development of an error estimation and in Section 5.5 on systematical studies.

5.1 Data set

In this analysis, data from January 1, 2004 till July 8, 2008 is used. The reconstruction is performed with CDAS v4r6 p2. Bad periods, due to failures in the data acquisition, hardware difficulties and lightnings, are excluded. The following cuts are chosen, to archive full acceptance:

- Strict T5.
- Estimation compatible with reconstruction.
- Energy $E \geq 3$EeV.
- Zenith angle $\Theta \leq 60^\circ$.

The number of events that satisfy these cuts is 19895.

In the following analysis the attenuation function $f_{\mathrm{CIC}}(\cos^2\Theta)$ is tested for dependencies on temperature, humidity, pressure and density. The necessary weather informations are obtained from the "Bariloche Monitoring and Weather files" [48]. The weather data from the central laser facility (CLF) is used, because it measures the temperature values more precisely. Only from January 1, 2004 till June 22, 2004 data of the telescope station Los Leones (LL) is used, because the central laser facility

5.2 Description of the constant intensity cut method

In this section a new ansatz for the constant intensity cut method is developed. The procedure is described in detail.

Although anisotropy studies of ultra high energy cosmic rays show an anisotropy of events with energies higher than 57 EeV in equatorial coordinates, the flux is expected to be isotropic for lower energies and local coordinates [18].

The number of the events observed by the Pierre Auger Observatory is proportional to $\sin(\Theta)\cos(\Theta)$, for geometrical reasons. The $\sin(\Theta)$ term is caused by the increasing spherical segment and the $\cos(\Theta)$ term is due to the effective detector surface A_{eff}. The effective detector surface is given by: $A_{\mathrm{eff}} = A \cdot \cos\Theta$, see Figure 5.1. The theta distribution of the events and the $const \cdot \sin(\Theta)\cos(\Theta)$ fit are shown in Figure 5.2. The peak at 71° is caused by a change of the reconstruction method at 70°. The electromagnetic component decreases due to the longer distance covered in the atmosphere and therefore the muonic part preponderates. Therefore the energy of horizontal showers with zenith angles $\Theta \geq 70^\circ$ is reconstructed in a different way, because of the high muon fraction. With the changed reconstruction method the reconstructed energy is higher than with the other method and more events are able to cross the energy cut of 3 EeV. This modification of the reconstruction has no influence on this analysis, as only events with zenith angles below $\Theta = 60^\circ$ are used.

The Θ distribution plotted against $\cos^2\Theta$ is expected to be a constant distribution. This distribution is divided into ten bins, in order to have enough data points to plot and

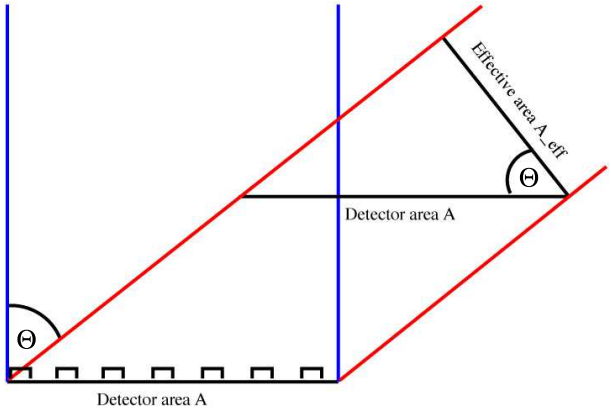

Figure 5.1: Effective detector area: $A_{\text{eff}} = A \cdot \cos\Theta$.

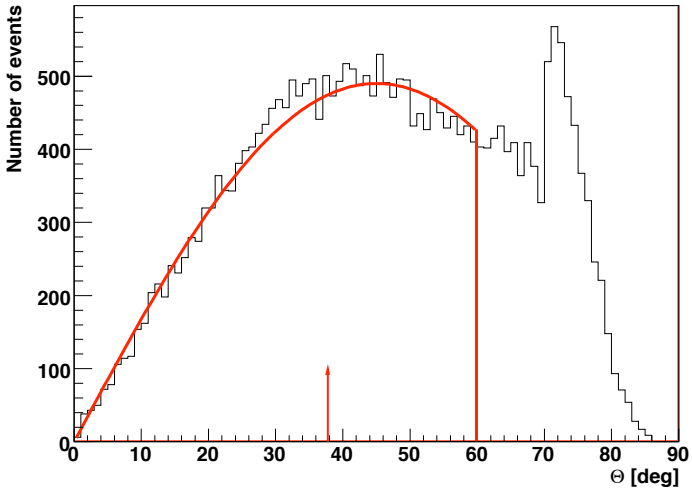

Figure 5.2: Distribution of events in dependency on the zenith angle Θ. The solid line illustrates the $const \cdot \sin(\Theta)\cos(\Theta)$ fit. $\Theta = 38°$, the median zenith angle of the $0° - 60°$ range, is marked by the arrow. The peak at 71° is caused by a change of reconstruction method.

to have enough entries N_i in each bin in order to guarantee sufficient statistics. To get bins of equal sized areas, the curve $\sin(\Theta)\cos(\Theta)$ is integrated with respect to Θ between 0° and 60°:

$$\int_{0^\circ}^{60^\circ} \sin(\Theta)\cos(\Theta)d\Theta = \left[\frac{1}{2}\sin^2(\Theta)\right]_{0^\circ}^{60^\circ} = \frac{1}{2}\sin^2(60^\circ) = \frac{1}{2}\left(1-\cos^2(60^\circ)\right). \quad (5.2)$$

The area below the integrated curve is divided into 10 bins of equal size. The limits of each bin i are calculated as follows:

$$\frac{i}{10}\cdot\frac{1}{2}\sin^2(60^\circ) = \frac{1}{2}\sin^2(\Theta_i) \qquad \Rightarrow \qquad \Theta_i = \arcsin\left(\sqrt{\frac{i}{10}}\cdot\sin(60)^\circ\right). \quad (5.3)$$

The median value of each bin is calculated in the same way.

The events are sorted into the resulting Θ bins and an average $\overline{\Theta}_i$ of the Θ values in each bin is calculated. The number N_i of events in each bin i, the edges of the ten bins, the median values and their average values $\overline{\Theta}_i$ with errors $\Delta\overline{\Theta}_i$ are given in Table 5.1. For the constant intensity cut method the average values $\overline{\Theta}_i$ are used. Their errors $\Delta\overline{\Theta}_i$ are calculated by the standard deviation.

Bin i	N_i	Θ-range	median value	$\overline{\Theta}_i$	$\Delta\overline{\Theta}_i$
1	1887	$0.00^\circ - 15.89^\circ$	11.17°	10.56°	0.09°
2	1968	$15.89^\circ - 22.79^\circ$	19.60°	19.56°	0.05°
3	2035	$22.79^\circ - 28.32^\circ$	25.66°	25.63°	0.04°
4	2141	$28.32^\circ - 33.21^\circ$	30.82°	30.79°	0.03°
5	2060	$33.21^\circ - 37.76^\circ$	35.52°	35.47°	0.03°
6	2044	$37.76^\circ - 42.13^\circ$	39.96°	39.96°	0.03°
7	2035	$42.13^\circ - 46.43^\circ$	44.28°	44.31°	0.03°
8	1921	$46.43^\circ - 50.77^\circ$	48.59°	48.60°	0.03°
9	1883	$50.77^\circ - 55.24^\circ$	52.98°	53.03°	0.03°
10	1921	$55.24^\circ - 60.00^\circ$	57.58°	57.57°	0.03°

Table 5.1: The number of bin entries N_i in each bin i, the ranges of the ten Θ bins, the median values and the average of Θ values of each bin are listed.

In Figure 5.3, the number N_i of events in each Θ-bin is illustrated. Ideally, the number of entries in every bin should be equal, because the flux of cosmic particles is isotropic and the integrated surfaces of the bins are identical. In reality, there are statistical fluctuations. The straight line illustrates the average number $\overline{N} = 1989.5$ of the bin entries N_i.

In each bin the entries are sorted according to their value of $S(1000)$ in increasing order and numbered from the higher $S(1000)$ values down to the lower ones. Every time in this analysis, speaking about the number of an entry, the number of the entry, counted down from the highest $S(1000)$, is meant.

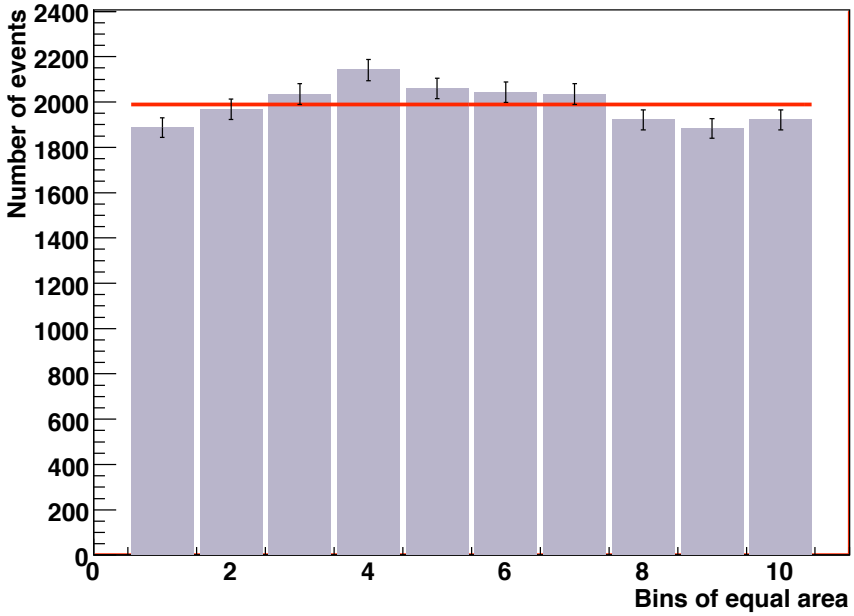

Figure 5.3: Number of events in the equal sized Θ bins. The total number of events is 19895. The line illustrates the average value $\overline{N} = 1989.5$ of the number of bin entries N_i.

Equally numbered bin entries are expected to correspond to the same intensity, because particles arrive isotropically from the cosmos and the bins have the same sizes. These equally numbered bin entries, corresponding to a cut at a constant intensity, are selected and plotted against $\cos^2\Theta$. Figure 5.4 illustrates $S_{\mathrm{CIC}}(1000)$ in dependence on the zenith angle Θ for the entry number 1030 in all bins.

$S_{\mathrm{CIC}}(1000)$,which depends on the energy E and the zenith angle Θ, is separated in the energy estimator $S_{38^\circ}(E)$ and the attenuation function $f_{\mathrm{CIC}}(\cos^2\Theta)$:

$$S_{\mathrm{CIC}}(1000) = S_{38^\circ}(E) \cdot f_{\mathrm{CIC}}(\cos^2\Theta). \tag{5.4}$$

$S_{38^\circ}(E)$ is the value of $S(1000)$ for an event with a zenith angle of $\Theta = 38^\circ$, the median zenith angle. The Θ distribution of the events with an energy $E \geq 3$EeV and a zenith angle $\Theta \leq 60^\circ$ has its median angle at $\Theta \cong 38^\circ$ and therefore $S_{38^\circ}(E)$ is chosen as the reference signal. Since $S_{\mathrm{CIC}}(1000) = S_{38^\circ}(E)$ for $\Theta = 38^\circ$, the attenuation function has to fulfill the side condition $f_{\mathrm{CIC}}(\cos^2 38^\circ) = 1$. The $S_{\mathrm{CIC}}(1000)$ curve is fitted with the following 2nd order polynomial, because it describes the curve well:

$$S_{\mathrm{CIC}}(1000) = S_{38^\circ}(E) \cdot f_{\mathrm{CIC}}(\cos^2\Theta) = S_{38^\circ}(E) \cdot (1 + ax + bx^2), \tag{5.5}$$

with $x = \cos^2(\Theta) - \cos^2(38^\circ)$ and the parameters a and b. For the zenith angle $\Theta = 38^\circ$, x is equal zero and $f_{\mathrm{CIC}}(\cos^2 38^\circ)$ becomes one. The required condition is fulfilled. After determining the attenuation function $f_{\mathrm{CIC}}(\cos^2\Theta)$, it is possible to calculate the energy estimator $S_{38^\circ}(E)$ from each signal $S(1000)$, considering the zenith angle Θ:

$$S_{38^\circ}(E) = \frac{S(1000)}{f_{\mathrm{CIC}}(\cos^2\Theta)}. \tag{5.6}$$

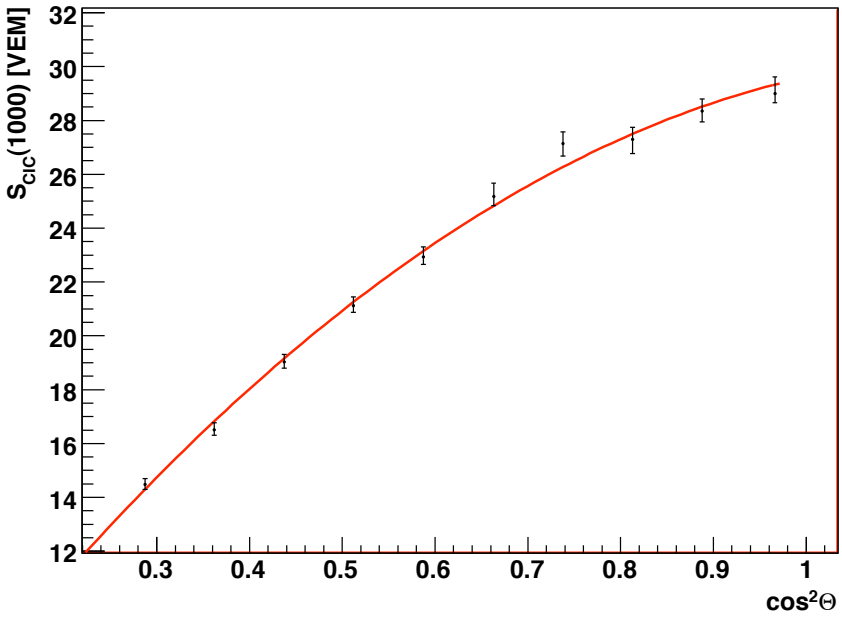

Figure 5.4: $S_{\mathrm{CIC}}(1000)$ in dependence on $\cos^2\Theta$. For this cut, entry number 1030 is chosen which corresponds to an energy of $E \approx 4.3$ EeV. The entry number 1030 is not corrected for fluctuations of the number of bin entries. The error estimation is explained in section 5.4.

In this analysis, the stability of the constant intensity cut method is investigated by studying the attenuation function. The advantage of $f_{\mathrm{CIC}}(\cos^2\Theta)$ over the $S_{\mathrm{CIC}}(1000)$ curve is, that it is not depending on the energy. The energy dependent fraction of $S(1000)$ is separated in the energy estimator S_{38° and the attenuation function $f_{\mathrm{CIC}}(\cos^2\Theta)$ which is, for an ideal case, independent of the energy and hence identical for all energies.

5.3 Correction

Because of the isotropic flux of UHECRs, it is expected that all ten bins are filled with the same number of entries and that equal numbered entries correspond to the same energy. But in reality, the number N_i of entries has statistical fluctuations and additionally a sine like fluctuation, as it is visible in Figure 5.3. The number of entries varies between 1830 and 2108. The sine like fluctuation is discussed by the Bariloche group [49], but not understood yet. Because it would go beyond the scope of this thesis, the reason for these fluctuation is not discussed in this section. It is still necessary to correct for this fluctuations, to be sure to deal with equal intensities. To achieve this, the number of entries is normalised to the average $\overline{N}$ of the ten bins. The average is given by:

$$\overline{N} = \frac{\sum_{i=1}^{10} N_i}{10} = 1989.5. \tag{5.7}$$

The correction factor p_N, to correct for the fluctuations, is calculated as follows:

$$p_{N_i} = \frac{N_i}{\overline{N}}. \tag{5.8}$$

The corrected bin entry number N_{CIC}:

$$N_{\mathrm{CIC}} = p_{N_i} \cdot N_{\mathrm{cut}}. \tag{5.9}$$

As an example $N_{\mathrm{cut}} = 1030$ is the chosen entry number. In the first bin the correction factor is given by $p_{N_i} = \frac{N_i}{\overline{N}} = \frac{1887}{1989.5} = 0.948$ and accordingly entry

$$N_{\mathrm{CIC}} = p_{\mathrm{N_i}} \cdot N_{\mathrm{cut}} = 0.948 \cdot 1030 = 976$$

is the corrected entry number, corresponding to to a chosen energy.

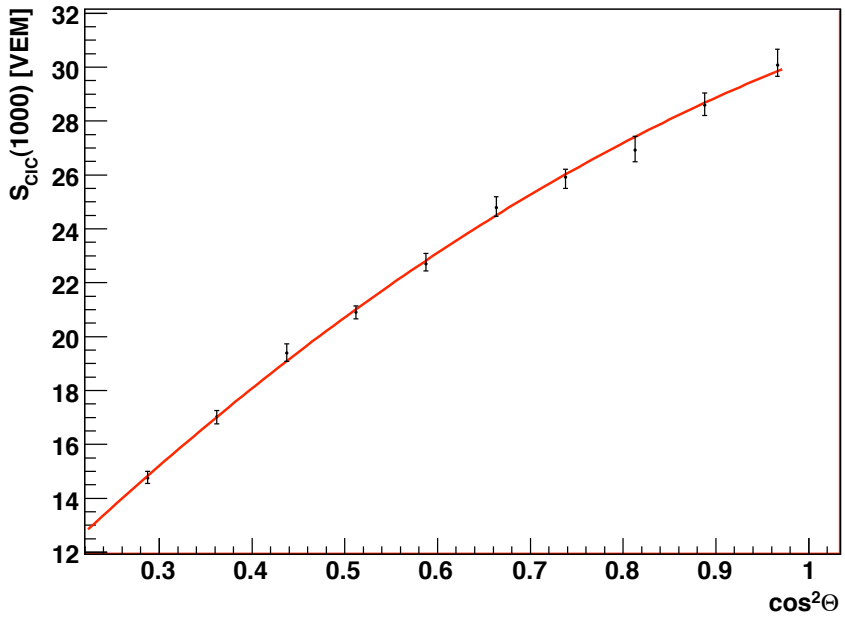

Figure 5.5: $S_{\mathrm{CIC}}(1000)$ in dependence of $\cos^2\Theta$. For this cut entry number $N_{\mathrm{cut}} = 1030$ is chosen. The correction for fluctuations leads to $N_{\mathrm{CIC}} = p_{N_i} \cdot N_{\mathrm{cut}}$.

In Figure 5.5 the corrected $S_{\mathrm{CIC}}(1000)$ values are plotted in dependence of $\cos^2\Theta$. It becomes obvious, that the corrected $S_{\mathrm{CIC}}(1000)$ are closer to the fit, than in Figure 5.4. The correction has no visible effect on the error $\Delta^{\pm} S_{\mathrm{CIC}}(1000)$.

5.4 Statistical error estimation of $S_{\mathrm{CIC}}(1000)$

In this section, the errors of the curve $S_{\mathrm{CIC}}(1000)$ are estimated. $S_{\mathrm{CIC}}(1000)$ is influenced by three errors:

1. The error of the statistical fluctuations in each bin.
2. The influence of $\Delta S(1000)$, which results from the reconstruction.
3. The influence of $\Delta\Theta$, which results from the reconstruction.

The total error $\Delta S_{\mathrm{CIC}}(1000)$ is calculated using error propagation.

5.4.1 Influence of statistical fluctuations

It is essential to estimate an error for the statistical fluctuations in each bin. The number N_i of entries in each bin has the statistical error $\sqrt{N_i}$. Therefore, corrected values N_{CIC} are calculated for $N_i \pm \sqrt{N_i}$:

1. $p_{N^+} = \frac{N_i+\sqrt{N_i}}{\overline{N}} \quad \Rightarrow \quad N^+_{\mathrm{CIC}} = p^+_N \cdot N_{\mathrm{cut}}.$
2. $p_{N^-} = \frac{N_i-\sqrt{N_i}}{\overline{N}} \quad \Rightarrow \quad N^-_{\mathrm{CIC}} = p^-_N \cdot N_{\mathrm{cut}}.$

For each bin, three values are available: N_{CIC}, N^+_{CIC} and N^-_{CIC}. N^+_{CIC} and N^-_{CIC} lead to asymmetric error components of $S_{\mathrm{CIC}}(1000)$:

$$\sigma^+_{\mathrm{fluc}} = S(1000)(N^+_{\mathrm{CIC}}) - S(1000)(N_{\mathrm{CIC}}), \tag{5.10}$$
$$\sigma^-_{\mathrm{fluc}} = S(1000)(N^-_{\mathrm{CIC}}) - S(1000)(N_{\mathrm{CIC}}). \tag{5.11}$$

The values of $\sigma^{\pm}_{\mathrm{fluc}}$ are listed in Table 5.2.

5.4.2 Influence of $\Delta S(1000)$

The measurements of S(1000) have an averaged uncertainty of around 10%. A deviation of the $S(1000)$ value can change the order of events in the corresponding bin. Therefore a fluctuation study with real data events is performed.

All $S(1000)$ values are sorted into the ten zenith angle bins. Each entry in each bin is shuffled according to a Gaussian distribution, the mean value of the Gaussian distribution is $S(1000)$ and the width is given by the corresponding error $\Delta S(1000)$ of the reconstruction. After the shuffling, all values in a bin are sorted in increasing order and numbered from the higher $S(1000)$ values to the lower ones, as usual. This procedure is repeated 1000 times for each bin entry in all ten bins and consequently for all bins 1000 lists of sorted $S(1000)$ values have been generated. From each list and for each bin, the entry with the number N_{CIC} is selected, and for each bin, a distribution of the 1000 selected

$S_{\mathrm{CIC}}(1000)$ values is created. They are Gaussian distributed and the FWHM gives the statistical error of this $S_{\mathrm{CIC}}(1000)$ value:

$$\mathrm{FWHM} = 2\sqrt{2\ln 2}\sigma \approx 2.35\sigma_{S(1000)} \quad \longrightarrow \quad \sigma_{S(1000)} \approx \frac{\mathrm{FWHM}}{2.35}. \tag{5.12}$$

$\sigma_{S(1000)}$ is the taken uncertainty. In Figure 5.6 the Gaussian distribution of the first bin is shown, in Figure A.1 in Appendix A the distributions of all ten bins are illustrated.

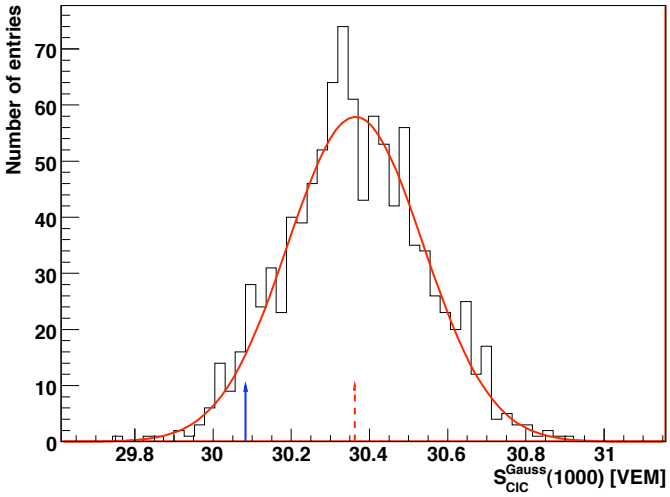

Figure 5.6: The Gaussian distributions of the first bin. The solid arrow marks the $S_{\mathrm{CIC}}(1000)$ data value, the dashed arrow denotes the mean value of the Gaussian distribution. The FWHM is the error $\sigma_{S(1000)}$.

It becomes obvious, that in all ten bins the Gaussian generated $S_{\mathrm{CIC}}^{\mathrm{Gauss}}(1000)$ values are shifted to higher values, because the data value (solid arrow) is always lower, than the mean value of generated values (dashed arrow). To check, if the whole $S^{\mathrm{Gauss}}(1000)$ spectrum is shifted, the difference of the original data value $S^{\mathrm{data}}(1000)$ and the resulting Gauss generated $S^{\mathrm{Gauss}}(1000)$ of each entry in each bin is calculated. Here, not the sorted $S^{\mathrm{Gauss}}(1000)$ lists are used, because the aim of these plots is to show, how the generated $S^{\mathrm{Gauss}}(1000)$ deviates in comparison to the corresponding original data value $S^{\mathrm{data}}(1000)$. The N_i differences of every bin are summed up and divided by the number of bin entries N_i.

$$S_{\mathrm{offset}} = \frac{\sum_0^{N_i}(S^{Gauss}(1000) - S^{data}(1000))}{N_i}. \tag{5.13}$$

This average is produced a 1000 times for each bin, because 1000 lists of generated values are existing. The 1000 values of the first bin are shown in Figure 5.7. The Gaussian distributions of $S_{\mathrm{offset}}(1000)$ for all ten bins are shown in Figure A.2 in Appendix A . All mean values of the distributions are compatible with zero. The average difference

$S_{\text{offset}}(1000) = (0.002 \pm 0.003)$ VEM and, hence, there is no noticeable offset of the $S^{\text{Gauss}}(1000)$ spectrum.

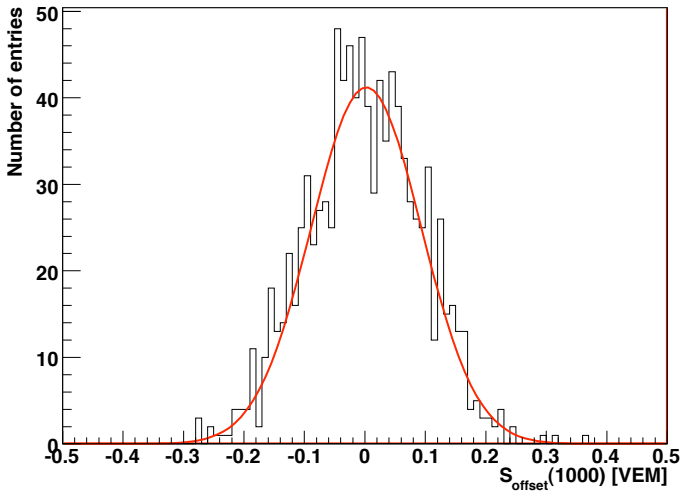

Figure 5.7: First bin: Distribution of $S_{\text{offset}}(1000)$. The mean value is compatible with zero, the $S^{\text{Gauss}}(1000)$ spectrum is not shifted to higher values.

Another possible explanation for the difference between the data value $S^{\text{data}}_{\text{CIC}}(1000)$ and the mean value of the Gauss distribution $S^{\text{Gauss}}_{\text{CIC}}(1000)$ could be a widening of the $S^{\text{Gauss}}(1000)$ spectrum. To test this assumption, all generated $S(1000)$ lists are sorted according to their values and equal numbered entries are compared. For each bin entry N the average of all 1000 generated values $S^{\text{Gauss}}_i(1000,N)$ is calculated. Afterwards the differences between the averages and the equal numbered data values $S^{\text{data}}_i(1000,N)$ are estimated. This procedure is performed for all ten bins.

$$S_{\text{diff}}(1000,N) = \frac{\sum_{i=1}^{1000} S^{\text{Gauss}}_i(1000,N)}{1000} - S^{\text{data}}(1000,N). \tag{5.14}$$

In Figure 5.8, $S_{\text{diff}}(1000)$ of the first bin is plotted against the number N of the bin entry, numbered from the high $S(1000)$ values to the lower ones. In Appendix A, the plots of all bins are shown in Figure A.3. As guessed, the $S(1000)$ spectrum is broadened. In the first bin, all $S_{\text{diff}}(1000)$ with numbers N higher than 1476 are negative, the average of $S^{\text{Gauss}}_N(1000)$ is lower than $S^{\text{data}}_N(1000)$. The reason for this effect is the Gaussian shuffling. $S(1000)$ values corresponding to an energy around 3 EeV can fall below the 3 EeV cut, but, due to the event selection, there are no events with energies smaller than 3 EeV, that are able to cross this cut. All $S_{\text{diff}}(1000)$ with numbers between 338 and 1476 are positive, that means that the generated $S^{\text{Gauss}}_N(1000)$ values are higher than the data values. This is caused by the fact, that the density of events decreases with growing energy. Therefore, more generated events with lower $S(1000)$ can be shifted to a higher $S(1000)$, than the other way around, which causes a general shift to higher values. Bin entries smaller than 338 fluctuate around zero. Because of the high energy, the statistics

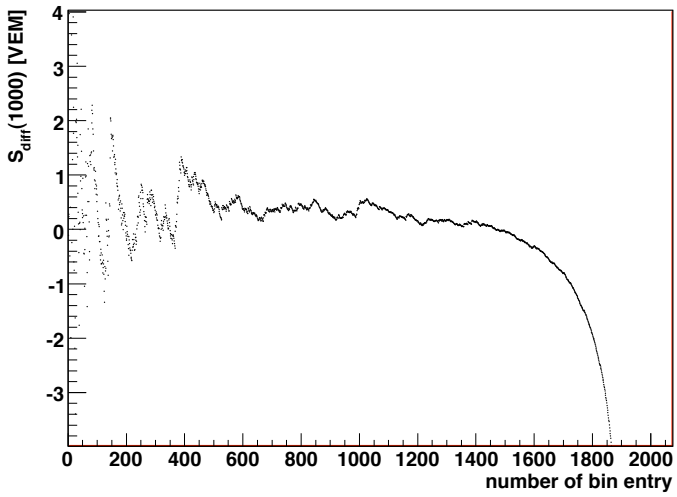

Figure 5.8: First bin: $S_{\text{diff}}(1000)$ versus bin entry number N. For low bin entries (high energies) the fluctuations are large. All $S_{\text{diff}}(1000)$ with numbers between 338 and 1476 are positive, for higher entries (low energy) $S_{\text{diff}}(1000)$ becomes negative.

are low and the $S(1000)$ values are not close to each other. The change of two events, because of the sorting, can cause high fluctuations of $S_{\text{diff}}(1000)$. These effects are also visible in the plots of the other nine bins.

In Figure 5.9 the average $\overline{S}_i^{\text{Gauss}}(1000,N) = \frac{\sum_{i=1}^{1000} S_i^{\text{Gauss}}(1000)}{1000,N}$ is compared with $S^{\text{data}}(1000,N)$ and fitted with the following function:

$$\overline{S}_i^{\text{Gauss}}(1000,N) = p_0 + p_1 \cdot S^{\text{data}}(1000,N), \tag{5.15}$$

with the y axis intercept p_0 and the slope p_1. $\overline{S}_i^{\text{Gauss}}(1000,N)$ for all ten bins is shown in Figure A.4 in Appendix A. Values higher than entry number $N = 1476$ are not considered, because the aim of this plot is to show how much the values between entry 338 and 1476 are shifted. At ≈ 20 VEM there is a bend, caused by the boarder effect at the 3 EeV cut, as described before, in Figure 5.8. After this bend the gradient of the curve is

$$p_1 = 1.0064 \pm 0.0007.$$

Therefore the Gaussian generated values are 0.64% higher than the data values.

The Gaussian distribution of the generated $S_{\text{CIC}}^{\text{Gauss}}(1000)$ is only fitted to the data to determine the error $\sigma_{S(1000)}$. The influence of the shift of the $S_{\text{CIC}}^{\text{Gauss}}(1000)$ values on the error $\sigma_{S(1000)}$ is estimated. Therefore, a second data value $S_{CIC_>}^{\text{data}}(1000)$ with a higher entry number $N_{CIC_>} > N_{\text{CIC}}$ is chosen, whose mean value of the generated $S_{CIC_>}^{\text{Gauss}}(1000)$ distribution is equal to the first data value $S_{\text{CIC}}^{\text{data}}(1000)$. The widths $\sigma_{S(1000)}$ of the two distributions of $S_{\text{CIC}}^{\text{Gauss}}(1000)$ and $S_{CIC_>}^{\text{Gauss}}(1000)$ are compared and $\sigma_{S_>(1000)}$ is around 0.3% higher than the width $\sigma_{S(1000)}$ of the original distribution.

For the given example at an energy of $E \simeq 4.3$ EeV the following calculation is made for the first bin: $S_{\text{CIC}}^{\text{data}}(1000) = 30.08$ VEM corresponds to the selected entry number

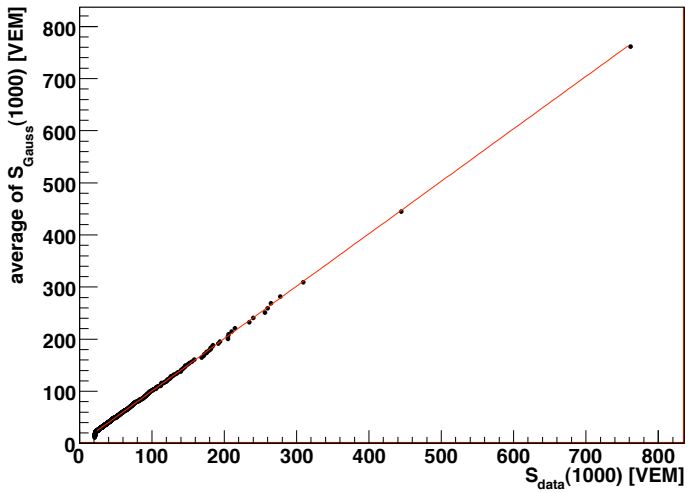

Figure 5.9: First bin: $\overline{S}_N^{\text{Gauss}}(1000)$ versus $S_N^{\text{data}}(1000)$.

$N_{\text{CIC}} = 976$. The mean value of the resulting distribution is $S_{\text{CIC}}^{\text{Gauss}}(1000) = 30.36$ VEM and the width is $\sigma_{S(1000)} = 0.1735$ VEM. $S_{CIC_>}^{\text{data}}(1000) = 29.69$ VEM has entry number $N_{CIC_>} = 997$. The mean value $S_{CIC_>}^{\text{Gauss}}(1000) = 30.07$ VEM is equal to the data value $S_{\text{CIC}}^{\text{data}}(1000) = 30.08$ VEM. The width of the distribution is $\sigma_{S_>(1000)} = 0.1740$ VEM and therefore the quotient is:

$$\frac{\sigma_{S_>(1000)}}{\sigma_{S(1000)}} = \frac{0.1740 \text{ VEM}}{0.1735 \text{ VEM}} = 1.00288 \simeq 1.003. \tag{5.16}$$

The following relation is obtained: $\sigma_{S_>(1000)} = 1.003 \cdot \sigma_{S(1000)}$.

The influence of the shift of Gaussian generated values is negligible for this error estimation. Therefore, the calculated value $\sigma_{S(1000)}$ can be used as a statistical error of $S_{\text{CIC}}(1000)$.

5.4.3 Influence of $\Delta\Theta$

In this section, the influence of the zenith angle uncertainty on $S_{\text{CIC}}(1000)$ values is studied. Taking their uncertainty $\Delta\Theta$, given by the reconstruction, into account, events, which are close to a bin edge, may cross over to a neighbouring bin. Hence, the consideration of $\Delta\Theta$ can result in a new order of the bin entries, caused by the exchange of events between neighbouring bins. To evaluate the order of magnitude of this effect, real events are shuffled using a Gaussian distribution. The mean value of this distribution is given by Θ and the width σ by the error $\Delta\Theta$ of the reconstruction. All events are fluctuated once and afterwards they are sorted into the ten bins. This procedure is repeated a 1000 times. For every bin, 1000 different lists of entries, sorted according to their $S(1000)$ value in increasing order, are available. To investigate the effect on a particular $S_{\text{CIC}}(1000)$ value, all entries with bin number N_{CIC} of these 1000 lists are selected and plotted in a histogram.

The resulting distribution is fitted with a Gaussian distribution, whose width gives the error σ_Θ on the chosen $S_{\mathrm{CIC}}(1000)$ data point. This is done for all ten bins. The Gaussian distribution of the first bin corresponding to $S^{\Theta}_{\mathrm{CIC}}(1000)$ is shown in Figure 5.10. The mean values of the distribution fluctuate randomly around the original data value. No systematic error becomes obvious. The Gaussian distributions of all ten bins are shown in Figure A.5 in Appendix A.

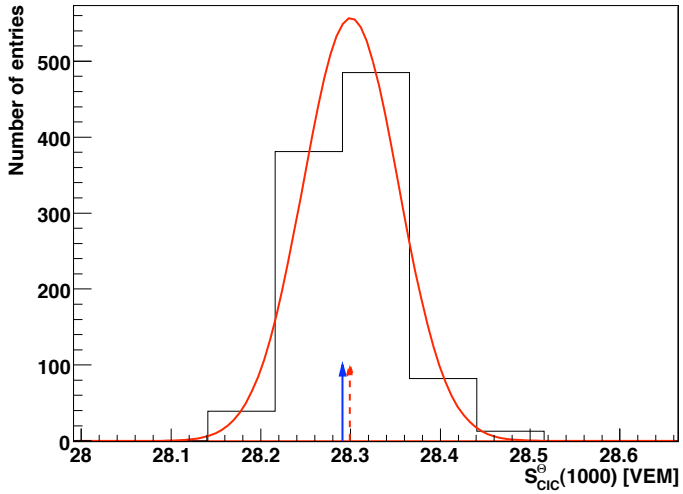

Figure 5.10: First bin: Distribution of $S^{\Theta}_{\mathrm{CIC}}(1000)$. The solid arrow marks the $S_{\mathrm{CIC}}(1000)$ data value, the dashed arrow the mean value of the Gaussian distribution of $S^{\Theta}_{\mathrm{CIC}}(1000)$.

In the $S_{\mathrm{CIC}}(1000)$ plot, $S_{\mathrm{CIC}}(1000)$ is plotted against $\cos^2\Theta$. For each bin, the average value of all Θ entries is calculated. Here it is analysed, if the average of the generated events differs from the average of data values. The average values of all 1000 lists per bin are calculated and the difference to the data average is built:

$$\Theta_{\mathrm{offset}} = \overline{\Theta}_{Gauss} - \overline{\Theta}_{data}. \tag{5.17}$$

Θ_{offset} for the first two bins is plotted in histogram Figure 5.11 and fitted with a Gaussian distribution. The other histograms are illustrated Figure A.6 in Appendix A. All mean values of the Gaussian distribution, except the first and the second bin, are compatible with zero, the mean average values $\overline{\Theta}_{Gauss}$ of the generated events correspond to the average $\overline{\Theta}_{data}$ of the real data. Only the mean value of the distribution of Θ_{offset} in the first bin is negative, which implies that the generated values Θ_{Gauss} are smaller than the data values Θ_{data}. The reason for this is a border effect, caused by the shape of the Θ spectrum, which is proportional to $\sin(\Theta)\cos(\Theta)$. The Θ spectrum starts at zero and has a very high gradient. Therefore, in the first bin are less low Θ values that are able to fluctuate to higher values than high Θ values that may fluctuate to lower values. The average Θ value in the first bin is shifted to lower angles. The shuffling of events causes a systematic error. The Θ spectrum is broadened. Zenith angles below the maximum of the spectrum are shifted to lower values and angles above the maximum are shifted to higher values. This effect is largest in the first bin.

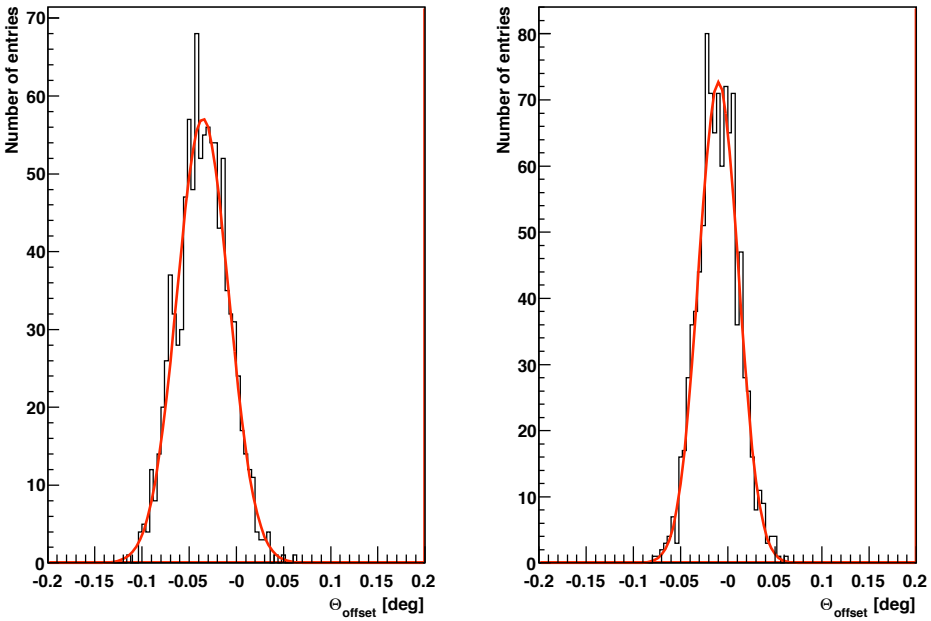

Figure 5.11: First and second bin: The Θ_{offset} distribution of the first bin (on the left) is shifted to lower angles. The effect of broadening is very small in the second bin.

5.4.4 Error estimation of $S_{\text{CIC}}(1000)$

The error of $S_{\text{CIC}}(1000)$ consists of three parts: $\sigma^{\pm}_{\text{fluc}}$, $\sigma_{S(1000)}$ and σ_{Θ}. $\Delta S_{\text{CIC}}(1000)$ is calculated using error propagation:

$$\Delta^{\pm} S_{\text{CIC}}(1000) = \sqrt{(\sigma^{\pm}_{\text{fluc}})^2 + (\sigma_{S(1000)})^2 + (\sigma_{\Theta})^2}. \tag{5.18}$$

In Table 5.2, the error components and the resulting errors $\Delta^{\pm} S_{\text{CIC}}(1000)$ are given for the cut at entry number $N_{\text{CIC}} = 1030 \cdot p_N$, which corresponds to an energy of $E \simeq 4.3$ EeV.

5.4.5 Error estimation of the attenuation function $f_{\text{CIC}}(\cos^2\Theta)$

$S(1000)$ is given by Equation 5.5:

$$S_{\text{CIC}}(1000) = S_{38^\circ}(E) \cdot (1 + ax + bx^2) = S_{38^\circ}(E) + a^* x + b^* x^2, \tag{5.19}$$

with $a^* = a \cdot S_{38^\circ}(E)$ and $b^* = b \cdot S_{38^\circ}(E)$. Therefore the attenuation function $f_{\text{CIC}}(\cos^2\Theta)$ is given by

$$f_{\text{CIC}}(\cos^2\Theta) = \frac{S_{\text{CIC}}(1000)}{S_{38^\circ}}. = 1 + \frac{a^*}{S_{38^\circ}} x + \frac{b^*}{S_{38^\circ}} x^2 = 1 + ax + bx^2 \tag{5.20}$$

The errors of $a = \frac{a^*}{S_{38^\circ}}$ and $b = \frac{b^*}{S_{38^\circ}}$ are calculated from the covariance matrix of the $S_{\text{CIC}}(1000)$ curve, because the parameters are correlated. The covariance matrix is:

Bin i	$S_{\mathrm{CIC}}(1000)$	$\sigma^{+}_{\mathrm{fluc}}$	$\sigma^{-}_{\mathrm{fluc}}$	$\sigma_{S(1000)}$	σ_{Θ}	$\Delta^{+}S_{\mathrm{CIC}}(1000)$	$\Delta^{-}S_{\mathrm{CIC}}(1000)$
1	30.08	0.54	-0.37	0.17	0.10	0.58	-0.42
2	28.60	0.37	-0.32	0.17	0.15	0.44	-0.39
3	26.93	0.45	-0.37	0.15	0.18	0.51	-0.43
4	25.92	0.22	-0.37	0.14	0.14	0.30	-0.42
5	24.79	0.35	-0.25	0.14	0.14	0.40	-0.32
6	22.70	0.34	-0.18	0.13	0.12	0.39	-0.25
7	20.91	0.17	-0.20	0.12	0.07	0.22	-0.25
8	19.40	0.29	-0.27	0.11	0.10	0.33	-0.31
9	17.03	0.20	-0.24	0.09	0.06	0.23	-0.26
10	14.76	0.20	-0.18	0.08	0.08	0.23	-0.21

Table 5.2: $S_{\mathrm{CIC}}(1000)$, its error components and the resulting errors $\Delta^{\pm}S_{\mathrm{CIC}}(1000)$ for a constant intensity cut at $N_{\mathrm{cut}} = 1030$. All values are given in VEM.

$$V = \begin{pmatrix} \sigma^2_{S_{38^\circ}} & cov(S_{38^\circ}, a^*) & cov(S_{38^\circ}, b^*) \\ cov(a^*, S_{38^\circ}) & \sigma^2_{a^*} & cov(a^*, b^*) \\ cov(b^*, S_{38^\circ}) & cov(b^*, a^*) & \sigma^2_{b^*} \end{pmatrix}. \tag{5.21}$$

The error is calculated from the general formula:

$$\sigma^2 = \sum_{i=1}^{m} \sum_{j=1}^{m} \frac{\partial f}{\partial a_i} \frac{\partial f}{\partial a_j} V_{ij}, \tag{5.22}$$

with $m = 3$. In this case, the errors σ_a and σ_b are:

$$\sigma_a = \sqrt{\frac{(a^*)^2}{S^4_{38^\circ}} \sigma^2_{S_{38^\circ}} + \frac{1}{S^2_{38^\circ}} \sigma^2_{a^*} - 2\frac{a^*}{S^3_{38^\circ}} cov(S_{38^\circ}, a^*)}, \tag{5.23}$$

$$\sigma_b = \sqrt{\frac{(b^*)^2}{S^4_{38^\circ}} \sigma^2_{S_{38^\circ}} + \frac{1}{S^2_{38^\circ}} \sigma^2_{b^*} - 2\frac{b^*}{S^3_{38^\circ}} cov(S_{38^\circ}, b^*)}. \tag{5.24}$$

The uncertainties of the $f_{\mathrm{CIC}}(\cos^2\Theta)$ curve are illustrated by an error band, given by the extremal values of the parameters a and b. In the following four curves the parameters a and b are changed against $a \pm \sigma_a$ and $b \pm \sigma_b$. The index $+-$, for example, means parameter a plus σ_a and parameter b minus σ_b:

$$f_{\mathrm{CIC}}(\cos^2\Theta)_{++} = 1 + (a+\sigma_a)x + (b+\sigma_b)x^2, \tag{5.25}$$

$$f_{\mathrm{CIC}}(\cos^2\Theta)_{+-} = 1 + (a+\sigma_a)x + (b-\sigma_b)x^2, \tag{5.26}$$

$$f_{\mathrm{CIC}}(\cos^2\Theta)_{-+} = 1 + (a-\sigma_a)x + (b+\sigma_b)x^2, \tag{5.27}$$

$$f_{\mathrm{CIC}}(\cos^2\Theta)_{--} = 1 + (a-\sigma_a)x + (b-\sigma_b)x^2. \tag{5.28}$$

For every value of $f_{\mathrm{CIC}}(\cos^2\Theta)$, the maximum and minimum of these four curves are calculated. This extrema are the borders of the error band. The resulting attenuation function $f_{\mathrm{CIC}}(\cos^2\Theta)$ is:

$$f_{\mathrm{CIC}}(\cos^2\Theta) = 1 + (0.94 \pm 0.02)x - (0.50 \pm 0.10)x^2. \tag{5.29}$$

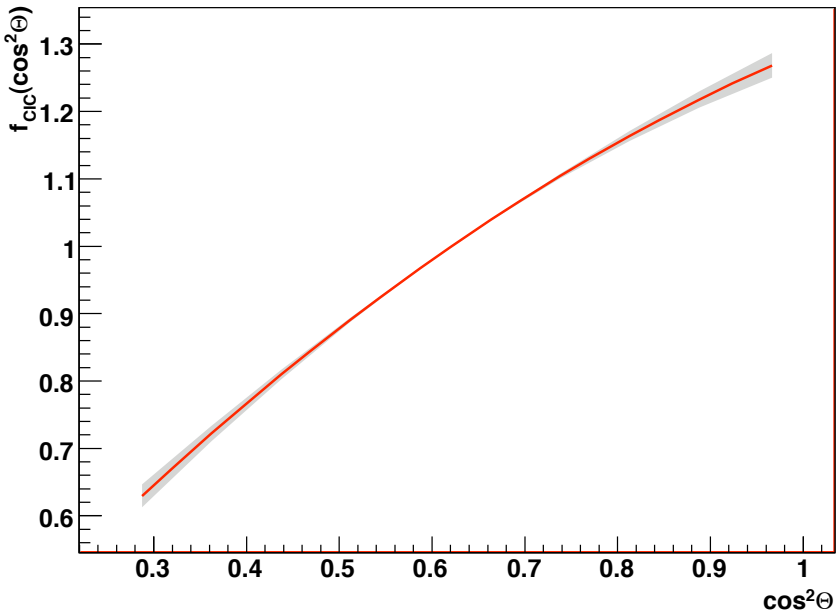

Figure 5.12: Attenuation function $f_{\mathrm{CIC}}(\cos^2\Theta)$ in dependence on $\cos^2\Theta$. The band illustrates the margin of error.

5.5 Systematic studies

5.5.1 Systematic study of Θ

In order to estimate the effect of a systematic displacement of the zenith angle Θ, caused by improper reconstruction, a systematic study is performed in this section. All Θ values are shifted once by $+1^\circ$ and once by -1°, because this shift is the range of the angular accuracy of 1.2°, and then are sorted into the ten equally sized Θ bins:

1. Displacement by $+1^\circ$: $\Theta_+ = \Theta + 1^\circ$.

2. Displacement by -1°: $\Theta_- = \Theta - 1^\circ$.

The zenith angle shift to $\Theta_- = \Theta - 1^\circ$ causes an increase of the total number of bin entries from 19895 to 20227. Zenith angles Θ of the first bin can become negative. The

arrival direction of an event with a negative zenith angle corresponds to the arrival direction of the positive zenith angle, but with a shift of the azimuth angle ϕ of 180°. For this reason events with $\Theta_- < 0°$ are sorted to the first bin. Therefore and because many events change from the second into the first bin, the number of entries in the first bin increases from 1887 to 2111.

After Θ shifting to $\Theta_+ = \Theta + 1°$, all modified zenith angles are sorted into the ten Θ bins. The number of entries in each bin and the shape of the distribution changes. In the first bin the number of entries changes from $N_1 = 1887$ to $N_1^+ = 1665$. The first bin is a special case. Because no events can change from lower zenith angles into the first, but 12% of the values change into the second bin. In the other bins, this effect is not as strong as in the first bin, because entries enter the bins as well as entries leave the bins. In total the number of events decreases from 19895 to 19519. The distributions of the number of events in the equally sized Θ bins are shown in Figure 5.13.

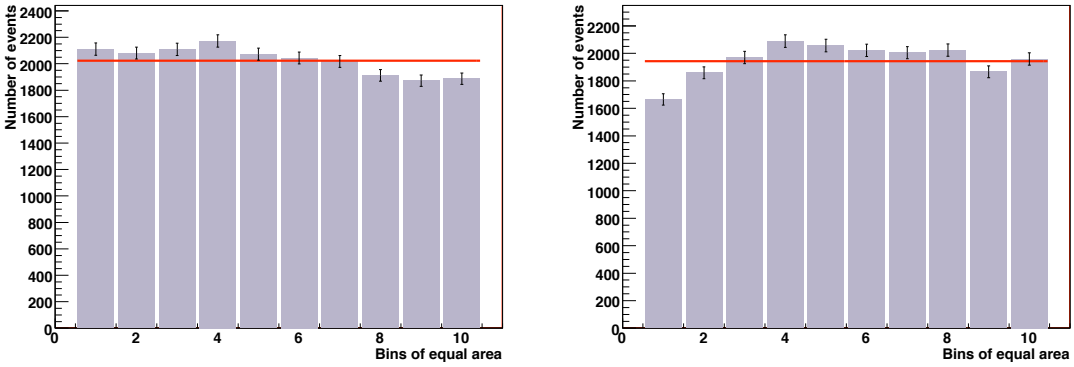

Figure 5.13: Number of events in the equally sized Θ bins. On the left: $\Theta_+ = \Theta + 1°$. The total number of events is 20227. The line illustrates the average value $\overline{N^-} = 2022.7$ of the number of bin entries N_i^-. On the right: $\Theta_- = \Theta - 1°$. The total number of events is 19519, the average value of N_i^+ is $\overline{N^+} = 1951.9$.

The procedure of the constant intensity cut method, as explained before, is performed with the shifted Θ values, for this systematic study. In Figure 5.5.1, $S_{\mathrm{CIC}}(1000)$ is plotted against $cos^2\Theta$ for Θ, Θ_+ and Θ_-, and in Figure 5.15 the attenuation curves $f(cos^2\Theta)$ for the three different cases of zenith angles Θ_-, Θ and Θ_+ are compared. In Table 5.3, the parameters a and b and the energy estimator $S_{38°}$ are given. Because the CIC method depends on the zenith angle Θ, the shift of Θ to Θ_+ or Θ_- is expected to have an influence on the attenuation function $f(cos^2\Theta)$. The curves are tilted with respect to each other. For zenith angles $\Theta > 38°$, the energy estimator $S_{38°} = \frac{S(1000)}{f_{\mathrm{CIC}}(cos^2\Theta)}$ is calculated higher for Θ_+ and lower for Θ_- than the data values Θ and for zenith angles $\Theta < 38°$ the other way around.

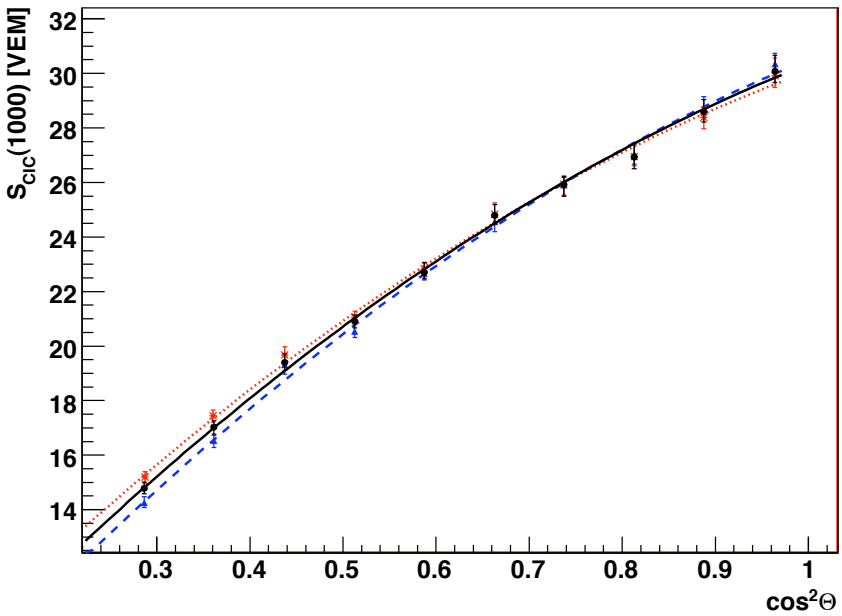

Figure 5.14: $S_{\mathrm{CIC}}(1000)$ in dependence of $cos^2\Theta$, plotted for Θ data values (black, solid line and dots), Θ_+ values (red, dotted line and stars) and Θ_- values (blue, dashed line and triangles). The intensity cut is made at bin entry $N_{\mathrm{cut}} = 1030$.

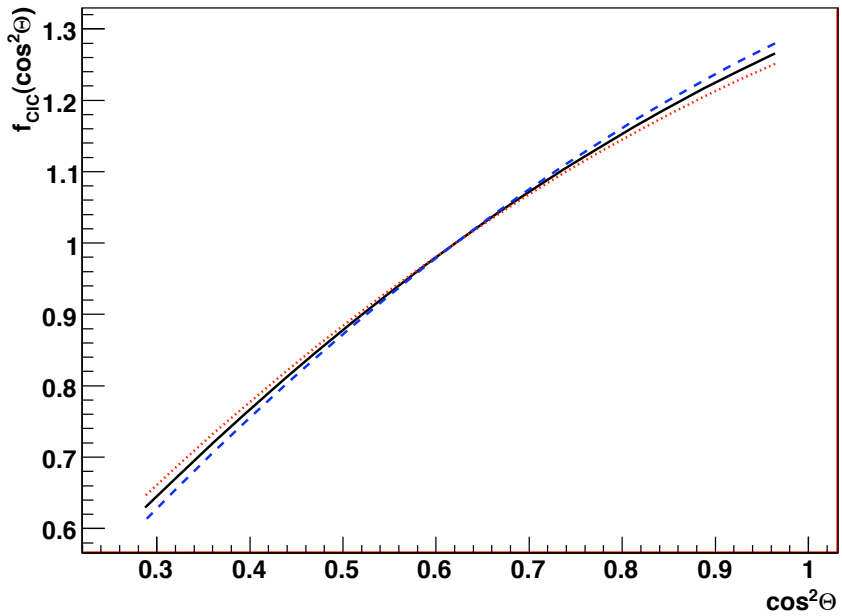

Figure 5.15: Attenuation function $f_{\mathrm{CIC}}(cos^2\Theta)$ in dependence of $cos^2\Theta$, plotted for Θ data values (black, solid line), Θ_+ values (red, dotted line) and Θ_- values (blue, dashed line). The intensity cut is made at bin entry $N_{\mathrm{cut}} = 1030$. The error bands are left out, because they superimpose each other. The attenuation functions of Θ_+ and Θ_- with error band are shown in Appendix A in Figures A.7 and A.8.

Θ	a	σ_a	b	σ_b	S_{38° [VEM]	$\sigma_{S_{38^\circ}}$ [VEM]
Θ_-	0.993	0.022	-0.517	0.098	23.43	0.14
Θ	0.944	0.022	-0.504	0.099	23.58	0.15
Θ_+	0.899	0.021	-0.488	0.097	23.67	0.13

Table 5.3: The parameters a and b of the attenuation function $f_{\mathrm{CIC}}(cos^2\Theta) = 1 + ax + bx^2$ are listed for Θ, Θ_+ and Θ_-. The energy estimator S_{38° is also given. The intensity cut is made at bin entry $N_{\mathrm{cut}} = 1030$ which corresponds to $E \approx 4.3$ EeV.

5.5.2 Systematic study of the binning

The subdivision into ten bins is chosen, to obtain both, enough entries per bin to provide enough statistics and, at the same time, to provide enough data points to fit a curve. In order to make sure, that the binning has no major influence on the result, two different binnings are investigated in this section: Eleven and 25 equally sized bins. The fragmentation into eleven bins is selected, because with one more bin the number N_i of events in each bin decreases by about 10% and the loss of statistics in each bin is low. In case the Θ values of the bin edges have any influence on the number of entries in each bin and if the shape of the bin entry distribution changes, this systematic study should reveal it. The subdivision into 25 bins is studied to investigate, if a higher number of $S_{\mathrm{CIC}}(1000)$ data points results in a more precise $S_{\mathrm{CIC}}(1000)$ curve and attenuation function $f_{\mathrm{CIC}}(\cos^2\Theta)$. The number of entries in each bin is smaller by 60% than for the fragmentation into ten bins and the relative statistical error on each $S_{\mathrm{CIC}}(1000)$ value is higher by 58%. In Figure 5.3, the histogram of the ten bins and in Figure 5.16 the histograms for the fragmentation in eleven and 25 bins, respectively, are illustrated.

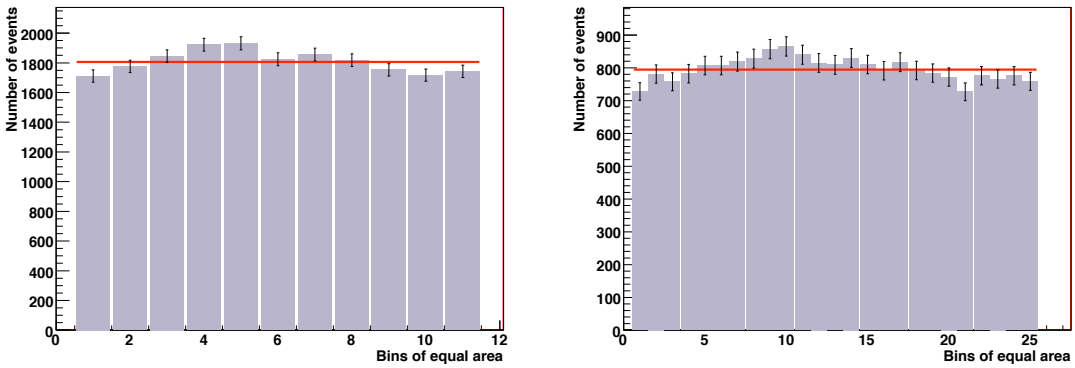

Figure 5.16: Number of events in the equally sized Θ bins. The shape of the distributions does not change noticeably with different binnings. On the left: Fragmentation into eleven bins. Average number of bin entries $\overline{N}_{11} = 1808.6$. On the right: Fragmentation into 25 bins, with the average number of bin entries $\overline{N}_{25} = 795.8$.

The sine-like shape of the distribution is independent of the binning. The positions of the bin edges do not influence the constant intensity cut method. The fluctuation error $\sqrt{N_i}$

of the number of bin entries is higher for the segmentation into 25 bins. In Figures 5.17, 5.18 and 5.19, the $S_{\mathrm{CIC}}(1000)$ curves and the attenuation functions $f_{\mathrm{CIC}}(\cos^2\Theta)$ of the different binnings are compared. The parameters a and b of the attenuation functions are given in Table 5.4. The attenuation functions of the systematic binning study agree with the chosen fragmentation into ten bins. The parameters a and b and S_{38° are consistent within 1σ. Also the errors are basically independent of the binning. The binning has no influence on the resulting attenuation function $f_{\mathrm{CIC}}(cos^2\Theta)$. Therefore, the chosen segmentation into ten bins is used for the following studies.

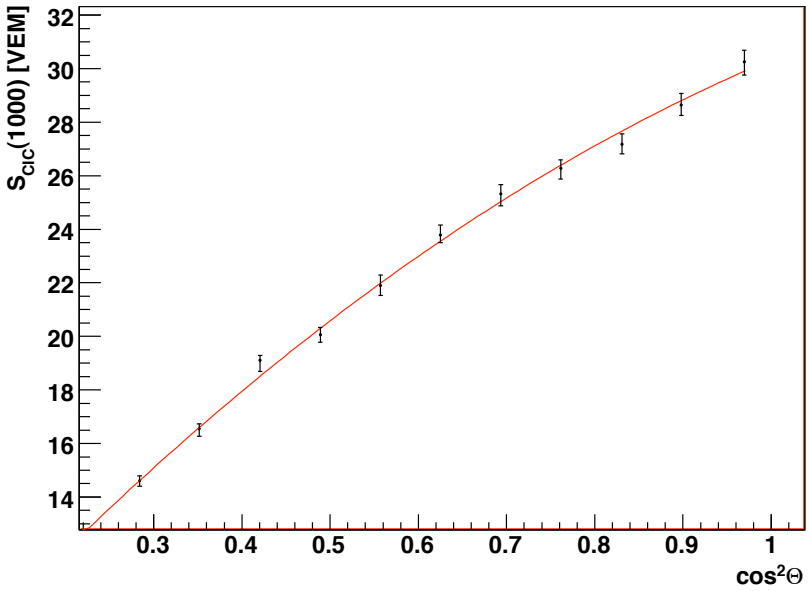

Figure 5.17: Fragmentation into eleven bins: $S_{\mathrm{CIC}}(1000)$ versus $\cos^2\Theta$. Average number of bin entries $\overline{N}_{11} = 1808.6$. The constant intensity cut method is performed with a corresponding energy of 4.3 EeV

Number of bins	a	σ_a	b	σ_b	S_{38° [VEM]	$\sigma_{S_{38^\circ}}$ [VEM]
10	0.944	0.022	-0.504	0.099	23.58	0.15
11	0.956	0.022	-0.489	0.101	23.46	0.15
25	0.917	0.024	-0.625	0.106	23.61	0.14

Table 5.4: The attenuation function is given by $f(cos^2\Theta) = 1 + ax + bx^2$, with the parameters a and b of the three different binnings. The constant intensity cut method is performed with an energy of $E \propto 4.3$ EeV.

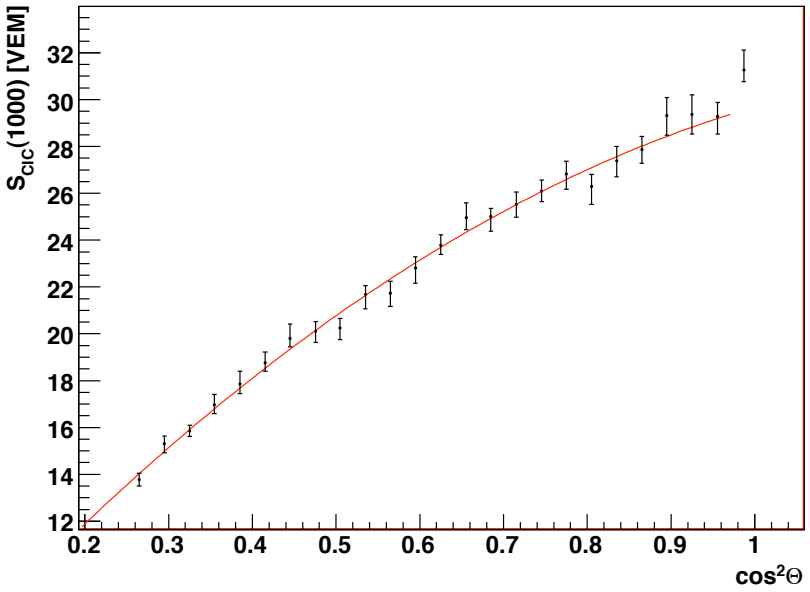

Figure 5.18: Fragmentation into 25 bins: $S_{\mathrm{CIC}}(1000)$ versus $\cos^2\Theta$. Average number of bin entries $\overline{N}_{25} = 795.8$. The constant intensity cut method is performed with a corresponding energy of 4.3 EeV

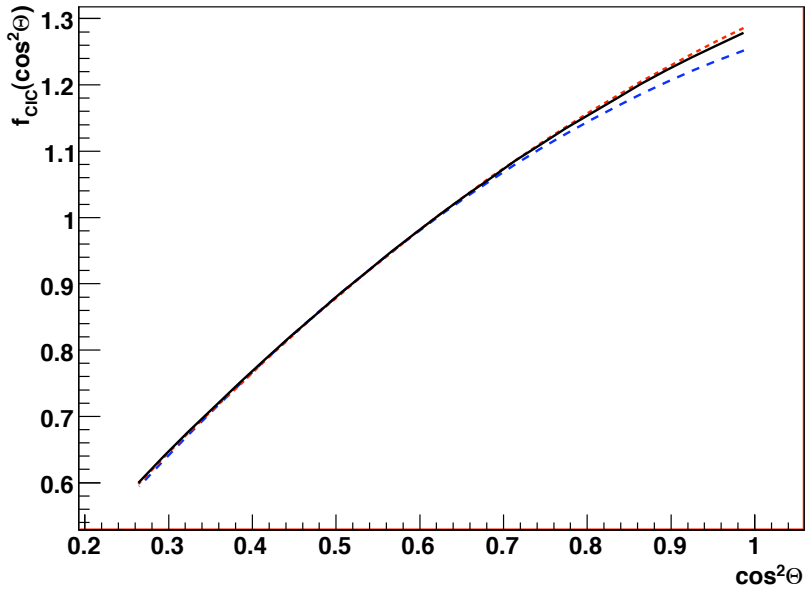

Figure 5.19: Comparison of the attenuation functions $f_{\mathrm{CIC}}(cos^2\Theta)$ of the fragmentation into ten (solid line), eleven (dotted line) and 25 bins (dashed line). The error bands are left out, because they superimpose each other. The attenuation functions with error band are shown in Figures A.9 and A.10 in the Appendix A.

Chapter 6

Constant intensity cut studies

In this chapter it is investigated, if the constant intensity cut method results are influenced by external effects, i.e. temperature, humidity, pressure, density or the distance between the central surface detector station and the shower core. Because the constant intensity cut method is used to determine the energy estimator S_{38°, it should be independent of external effects.

First the constant intensity cut method is performed for two different intensity cuts, corresponding to the energies $E \approx 4.3$ EeV and $E \approx 7.0$ EeV. Afterwards it is tested, if the attenuation function $f_{\mathrm{CIC}}(\cos^2\Theta)$ is only a function of the zenith angle Θ and not of the energy E. For the following studies, the constant intensity cut method and the error estimation are performed, like described in Chapter 5. The intermediary steps of the correction and the error estimation are not discussed here any more. Only the conclusions are shown. Except for the energy study, all analyses are performed with intensity cuts corresponding to the energies $E \approx 4.3$ EeV and $E \approx 7$ EeV, respectively. These cuts are chosen in order to analyse if external effects influence low and high energy events in a different way. The cut at $E \approx 4.3$ EeV is selected to avoid the ankle, which is supposed to be at approximately $E \approx 4.0$ EeV. In order to eliminate all possibilities of ankle effects, the cut at $E \approx 4.3$ EeV is used. The cut at 7 EeV is performed to investigate the constant intensity cut method at a high energy. This cut is chosen to account for both, a high energy E and enough statistics to apply the constant intensity cut method.

To use the reconstructed energy for the adopted cuts is an anticipation, because the aim of this method is to calibrate the energy. The corresponding energy is only given in order to get an impression of the order of magnitude.

6.1 Analysis of the attenuation function for different intensity cuts

In this section, the constant intensity cut method is performed for two different intensities, given by the entry numbers $N_{\mathrm{cut}} = 1030$ and $N_{\mathrm{cut}} = 452$ times the correction factor p_{N_i} for each bin i. The corresponding energies are $E \approx 4.3$ EeV and $E \approx 7$ EeV, respectively. In Table 6.1, the correction factor p_{N_i} and the cut numbers N_{CIC_i} of the entry numbers

$N_{\text{cut}} = 1030$ and $N_{\text{cut}} = 452$ are given.

Bin i	p_{N_i}	N_{CIC_i} of $N_{\text{cut}} = 1030$	N_{CIC_i} of $N_{\text{cut}} = 452$
1	0.948	976	428
2	0.989	1018	447
3	1.023	1053	462
4	1.076	1108	486
5	1.035	1066	468
6	1.027	1058	464
7	1.023	1053	462
8	0.966	994	436
9	0.946	974	427
10	0.966	994	436

Table 6.1: The correction factors p_{N_i} and the resulting intensity cuts N_{CIC_i} for $N_{\text{cut}} = 1030$ and $N_{\text{cut}} = 452$, respectively.

The resulting $S_{\text{CIC}}(1000)$ plot of the intensity cut at $N_{\text{cut}} = 452$ is shown in Figure 6.1 and the error components and the resulting errors $\Delta^{\pm}S_{\text{CIC}}(1000)$ are listed in Table 6.2. The $S_{\text{CIC}}(1000)$ plot at $N_{\text{cut}} = 1030$ is shown in Figure 5.5 and the errors in Table 5.2 in Section 5.4.4.

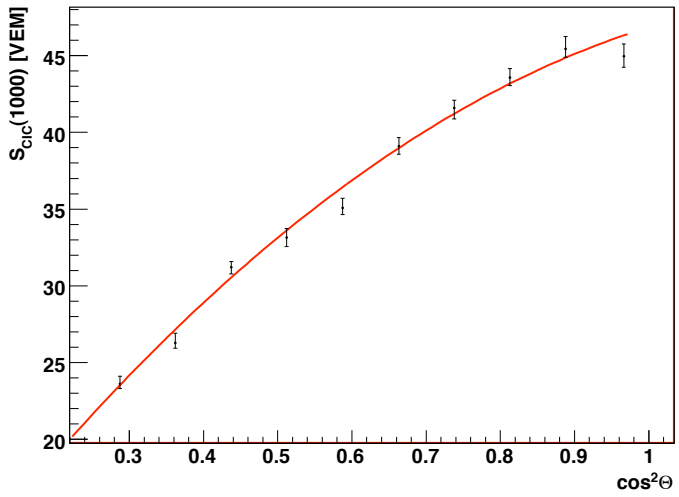

Figure 6.1: $S_{\text{CIC}}(1000)$ in dependence on $\cos^2\Theta$. For this cut, entry number $N_{\text{CIC}_i} = p_{N_i} \cdot N_{\text{cut}} = p_{N_i} \cdot 452$ is chosen.

The errors $\Delta^{\pm}S_{\text{CIC}}(1000)$ for the intensity cut at $N_{\text{CIC}_i} = p_{N_i} \cdot 452$ are 68% higher than the errors at $N_{\text{CIC}_i} = p_{N_i} \cdot 1030$. This increase of the error is caused by low statistics at high energies. The fit in Figure 6.1 agrees with the $S_{\text{CIC}}(1000)$ values and their errors. The resulting attenuation curves are shown in Figures 6.2 and in Section 5.3, Figure 5.12.

Bin i	$S_{\mathrm{CIC}}(1000)$	$\sigma^{+}_{\mathrm{fluct}}$	$\sigma^{-}_{\mathrm{fluct}}$	$\sigma_{\mathrm{S(1000)}}$	σ_{Θ}	$\Delta^{+}S_{\mathrm{CIC}}(1000)$	$\Delta^{-}S_{\mathrm{CIC}}(1000)$
1	44.96	0.65	-0.56	0.36	0.26	0.79	-0.71
2	45.43	0.66	-0.25	0.36	0.31	0.82	-0.54
3	43.58	0.40	-0.33	0.34	0.25	0.58	-0.53
4	41.59	0.35	-0.64	0.29	0.19	0.49	-0.73
5	39.10	0.42	-0.38	0.29	0.22	0.55	-0.52
6	35.08	0.55	-0.32	0.25	0.19	0.63	-0.45
7	33.14	0.47	-0.47	0.24	0.25	0.58	-0.59
8	31.20	0.25	-0.32	0.25	0.14	0.38	-0.43
9	26.27	0.61	-0.25	0.19	0.12	0.64	-0.33
10	23.60	0.46	-0.22	0.17	0.09	0.50	-0.29

Table 6.2: $S_{\mathrm{CIC}}(1000)$, its error components and the resulting errors $\Delta^{\pm}S_{\mathrm{CIC}}(1000)$ for a constant intensity cut at $N_{\mathrm{cut}} = 452$. All values are given in VEM.

The error bands illustrate the maximum possible deviation. The attenuation functions and the energy estimators S_{38° of the two intensity cuts are:

$E \approx 4.3$ EeV:

$$f_{\mathrm{CIC}}(\cos^2\Theta) = 1 + (0.94 \pm 0.02)x - (0.50 \pm 0.10)x^2, \quad (6.1)$$

$$S_{38^\circ} = (23.58 \pm 0.14)\ \mathrm{VEM}. \quad (6.2)$$

$E \approx 7.0$ EeV:

$$f_{\mathrm{CIC}}(\cos^2\Theta) = 1 + (0.90 \pm 0.02)x - (0.66 \pm 0.10)x^2, \quad (6.3)$$

$$S_{38^\circ} = (37.60 \pm 0.27)\ \mathrm{VEM}. \quad (6.4)$$

with $x = \cos^2\Theta - \cos^2 38^\circ$.

6.2 Energy behaviour of the constant intensity cut method results

One of the main assumptions of the constant intensity cut method is, that the attenuation function $f_{\mathrm{CIC}}(\cos^2\Theta)$ only depends on the zenith angle and not on the energy. If this condition is not fulfilled, the energy estimator S_{38° does not contain the complete energy dependence. In this section, the attenuation functions for the energies $E \approx 4$ EeV, 5 EeV, 6 EeV, 7 EeV, 8 EeV, 9 EeV and 10 EeV are calculated and compared. Because it is the aim of the constant intensity cut method to estimate the energy, this energy cuts are only performed to check the method. In Figure 6.3, the attenuation functions of all seven different energy cuts are plotted. All $S_{\mathrm{CIC}}(1000)$ plots and attenuation functions $f_{\mathrm{CIC}}(\cos^2\Theta)$ including error bands are shown in Appendix B (Figures B.1 to B.14).

In Table 6.3, the parameters a and b for all intensity cuts are listed. The errors σ_a and σ_b of the parameters increase marginally with increasing energy, because the number of

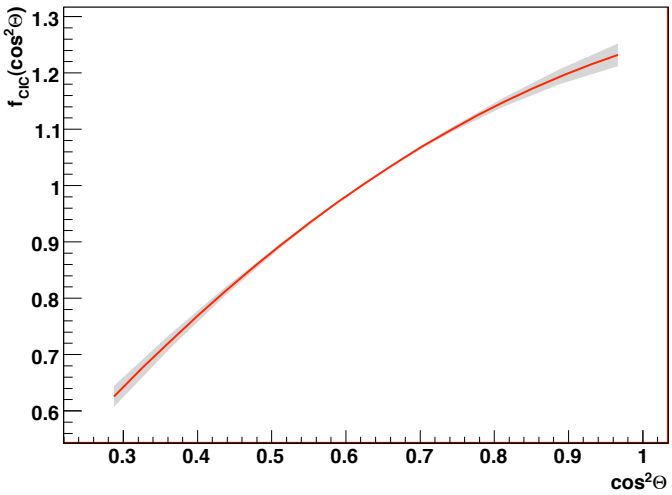

Figure 6.2: $f_{\mathrm{CIC}}(\cos^2\Theta)$ in dependence on $\cos^2\Theta$. The band illustrates the margin of error.

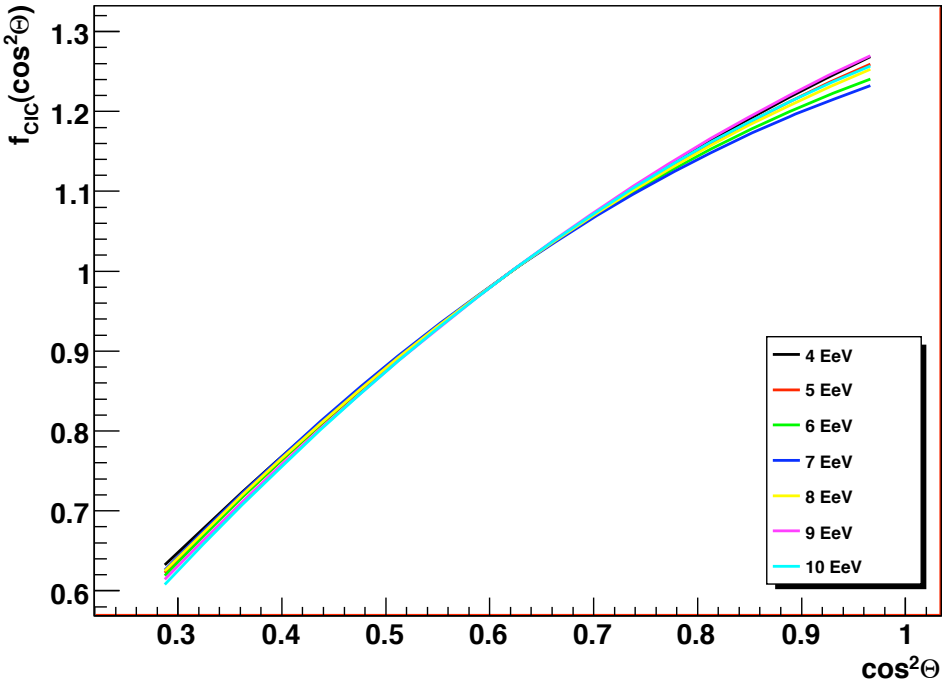

Figure 6.3: Attenuation function $f_{\mathrm{CIC}}(\cos^2\Theta)$ of the energies $E \approx 4$ EeV, 5 EeV, 6 EeV, 7 EeV, 8 EeV, 9 EeV and 10 EeV. The error bands are not shown, because they superimpose each other.

events decreases. For higher energies (e.g. in Figures B.9, B.11 and B.13) the fitted curve does not fit to the $S_{\mathrm{CIC}}(1000)$ data points as precise as for low energies. But the influence of the errors $\sigma^{\pm}_{S_{\mathrm{CIC}}(1000)}$ on σ_a and σ_b is very low. The errors σ_a and σ_b are calculated from Equations 5.23 and 5.24. S_{38° is the denominator in these equations and because S_{38° increases with the energy, the increase of σ_a and σ_b is marginal.

E [EeV]	a	σ_a	b	σ_b	S_{38° [VEM]	$\sigma_{S_{38^\circ}}$ [VEM]
4	0.943	0.020	-0.478	0.090	22.137	0.129
5	0.945	0.020	-0.563	0.094	27.151	0.176
6	0.923	0.022	-0.660	0.120	32.120	0.250
7	0.901	0.022	-0.663	0.103	37.596	0.269
8	0.932	0.022	-0.579	0.100	41.645	0.274
9	0.972	0.024	-0.554	0.107	47.298	0.317
10	0.964	0.022	-0.636	0.101	52.164	0.366

Table 6.3: The attenuation function is given by $f_{\mathrm{CIC}}(cos^2\Theta) = 1 + ax + bx^2$, with $x = \cos^2\Theta - \cos^2 38^\circ$ and the parameters a and b are given in dependence on the energy E.

As expected, the attenuation curves $f_{\mathrm{CIC}}(\cos^2\Theta)$ are independent of the energy E. In Figure 6.3 no energy dependence is visible. The attenuation curves are not ordered by their energies, but ranged randomly. The differences are due to fluctuations and low statistics. It would be meaningful to evaluate an average curve of the seven attenuation curves. But because the attenuation curves depend on each other, this is very complicated. In Figure 6.4, the parameters a and b are plotted against the energy E. An energy dependence is not visible here either. In order to obtain weighted mean values, the parameters a and b are fitted with constants, in consideration of their errors σ_a and σ_b. The resulting values are:

$$\overline{a} = 0.939 \pm 0.008, \tag{6.5}$$

$$\overline{b} = -0.58 \pm 0.04. \tag{6.6}$$

The errors $\sigma_{\overline{a}}$ and $\sigma_{\overline{b}}$ of the mean values $\overline{a}$ and $\overline{b}$ are underestimated, because the correlations between the attenuation functions at different energies are not considered. Since the parameters a, measured at different energies, are correlated, the error $\sigma_{\overline{a}}$ of the mean value $\overline{a}$ has to be calculated with

$$\sigma^2_{\overline{a}} = \sum_{i=1}^{m}\sum_{j=1}^{m} \frac{\partial f}{\partial_{x_i}}\frac{\partial f}{\partial_{x_j}} V^a_{ij}. \tag{6.7}$$

The same is necessary for the error $\sigma_{\overline{b}}$ of the mean value $\overline{b}$.

Only the diagonal entries σ_a and σ_b of the covariance matrixes V^a_{ij} and V^b_{ij} are known. The determination of the non diagonal entries of the covariance matrixes is very complex and is beyond the scope of this thesis. Due to the fact that the non diagonal entries of the

covariance matrixes make a contribution to the errors $\sigma_{\overline{a}}$ and $\sigma_{\overline{b}}$, these errors are strongly underestimated.

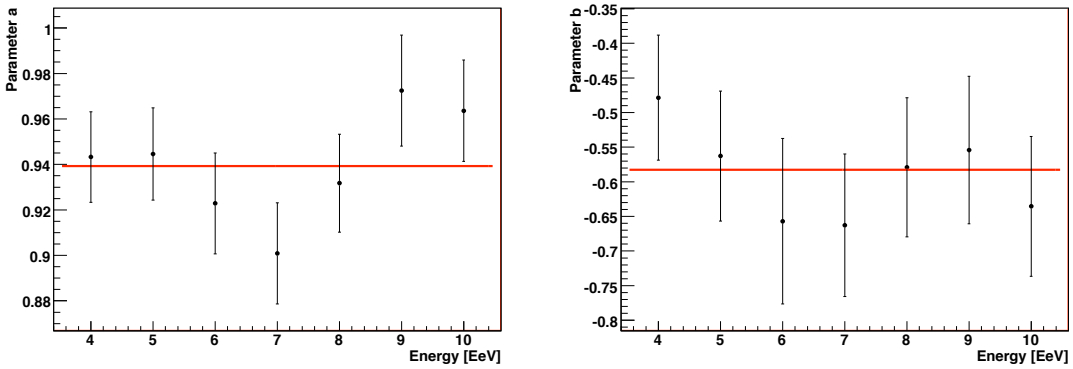

Figure 6.4: Parameters a (left) and b (right) of the attenuation function $f_{\mathrm{CIC}}(\cos^2\Theta)$ in dependence on the energy E.

6.3 Seasonal dependency on the constant intensity cut method results

The development of the extensive air shower depends strongly on the composition of the atmosphere. Atmosphere layers with higher densities ρ result in a faster decrease of the shower, because the secondary particles have to pass through a larger number of radiation lengths. The structure of the atmosphere is mainly affected by the seasons. Because only weather data from the detector level is available, the analysis of seasonal effects is the only possibility to analyse the parameters of the atmosphere, like temperature, pressure and humidity. Unfortunately, only the sum of these attributes can be studied and the influence of each parameter is not visible separately. In order to investigate, if the constant intensity cut method depends on seasonal effects, data of the summer months December, January and February and of the winter months June, July and August are compared, to deal with extremal values. Figure 6.5 shows the number of events in each bin for both data periods. The shape of the distributions differs from the shape of the distribution of the full data set in Figure 5.3. The total number of events of each period is $N = 4944$ and thus much lower than the total data set. Therefore, the histograms are more sensitive to fluctuations. It is not possible to make a statement about whether the shape depends on seasonal effects or not.

In Figure 6.6, the $S_{\mathrm{CIC}}(1000)$ values of the winter and summer periods are plotted against $\cos^2\Theta$. Because the data set contains approximately one quarter of the total data, the intensity cut is made at $N_{\mathrm{cut}} = 256$, which corresponds to an energy of $E \approx 4.3$ EeV. The difference of the plots is very small, with respect to the errors. No systematic effect becomes obvious. In Figure 6.7, the same plots are shown for an intensity cut at $N_{\mathrm{cut}} = 112$ corresponding to an energy of $E \approx 7.0$ EeV. The errors of these values are larger, but the

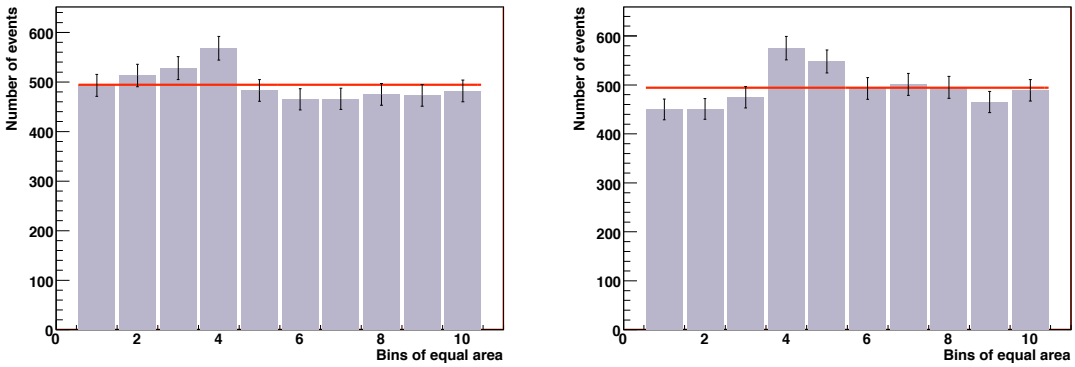

Figure 6.5: Number of events in the equally sized Θ bins. On the left: Summer, the total number of events is 4965. The horizontal line illustrates the average value $\overline{N} = 496.5$ of number of bin entries N_i. On the right: Winter, the total number of events is 4936. The line horizontal illustrates the average value $\overline{N} = 493.6$.

curves fit the data values very well. Because of the lower statistics at higher intensities, the sorted $S(1000)$ values in a bin are not as close to each other as they are at lower intensities, and the fluctuations are larger. The curves differ marginally. Figures 6.8 and 6.9 show the attenuation functions of $E \approx 4.3$ EeV and $E \approx 7.0$ EeV, respectively. The attenuation functions $f_{\mathrm{CIC}}(\cos^2\Theta)$ of $E \approx 4.3$ EeV are also almost equal, which is expected because of the similar $S(1000)$ curves. The difference of $f_{\mathrm{CIC}}(\cos^2\Theta)$ is higher, but in consideration of the errors, no seasonal effect is visible. The resulting parameters a and b and the energy estimator S_{38° are listed in Table 6.4. The parameters of the attenuation curves and the values of S_{38° agree within their errors.

E [EeV]	season	a	σ_a	b	σ_b	S_{38° [VEM]	$\sigma_{S_{38^\circ}}$ [VEM]
4.3	winter	0.898	0.046	-0.56	0.19	23.72	0.28
4.3	summer	0.897	0.044	-0.49	0.21	23.54	0.30
4.3	all data	0.944	0.022	-0.50	0.10	23.58	0.15
7.0	winter	0.894	0.046	-0.21	0.21	36.39	0.53
7.0	summer	0.824	0.053	-0.51	0.24	37.86	0.56
7.0	all data	0.901	0.022	-0.66	0.10	37.60	0.27

Table 6.4: Comparison between summer and winter: The attenuation function is given by $f_{\mathrm{CIC}}(x) = 1 + ax + bx^2$, with the parameters a and b in dependence on the season and the energy E. The energy estimator S_{38° is also listed.

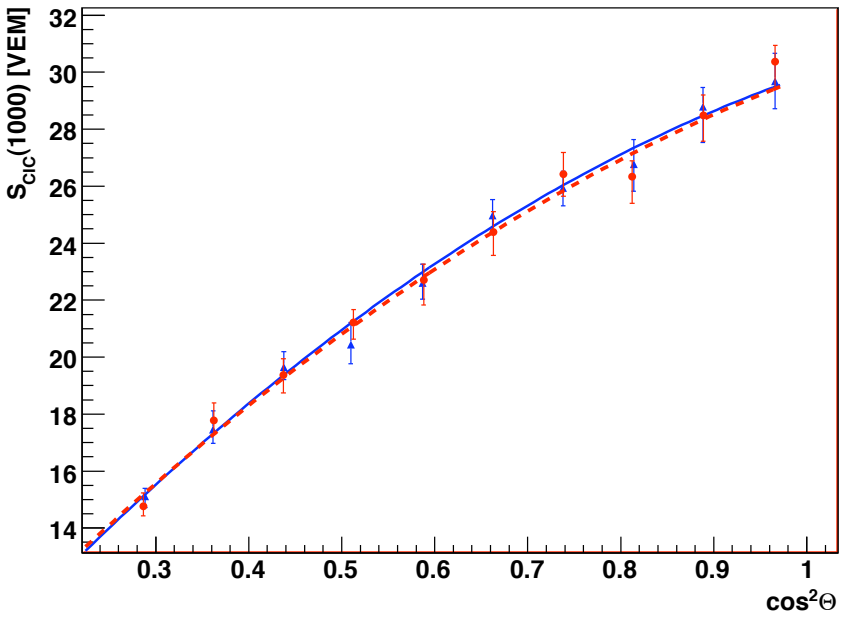

Figure 6.6: $S_{\mathrm{CIC}}(1000)$ in dependence on $\cos^2\Theta$. The values of the winter months (triangles and solid line) are compared to the values of the summer months (circles and dashed line). The cut is made at $N_{\mathrm{cut}} = 256$, which corresponds to an energy of $E \approx 4.3$ EeV.

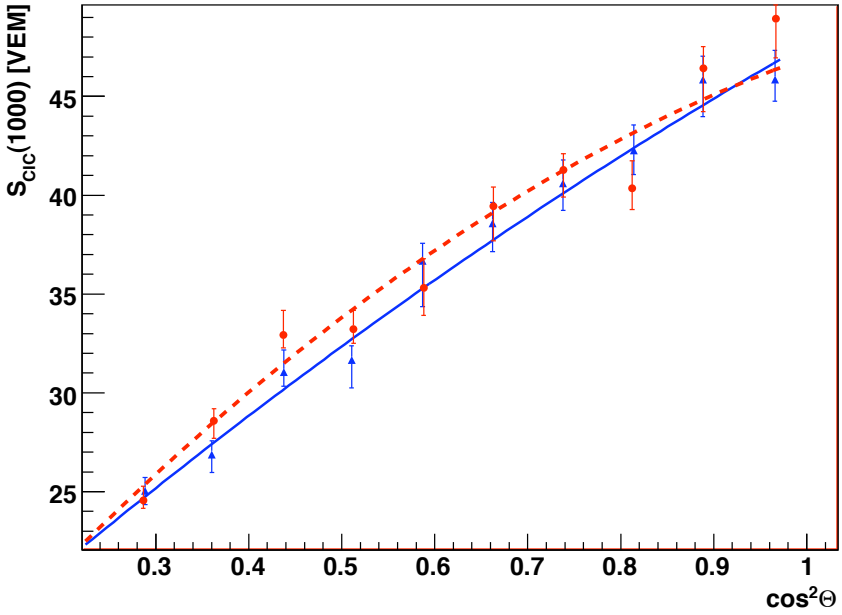

Figure 6.7: $S_{\mathrm{CIC}}(1000)$ in dependence on $\cos^2\Theta$. The values of the winter months (triangles and solid line) are compared to the values of the summer months (circles and dashed line). The cut is made at $N_{\mathrm{cut}} = 112$, which corresponds to an energy of $E \approx 7.0$ EeV.

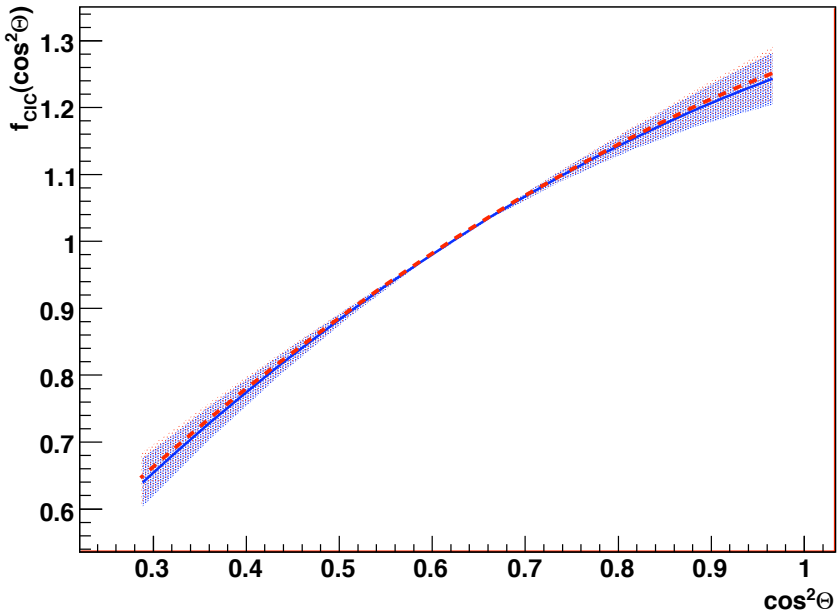

Figure 6.8: Attenuation functions $f_{\mathrm{CIC}}(\cos^2\Theta)$ for winter (solid line) and summer (dashed line) in dependence on $\cos^2\Theta$. The bands illustrate the margins of error. The corresponding energy is $E \approx 4.3$ EeV.

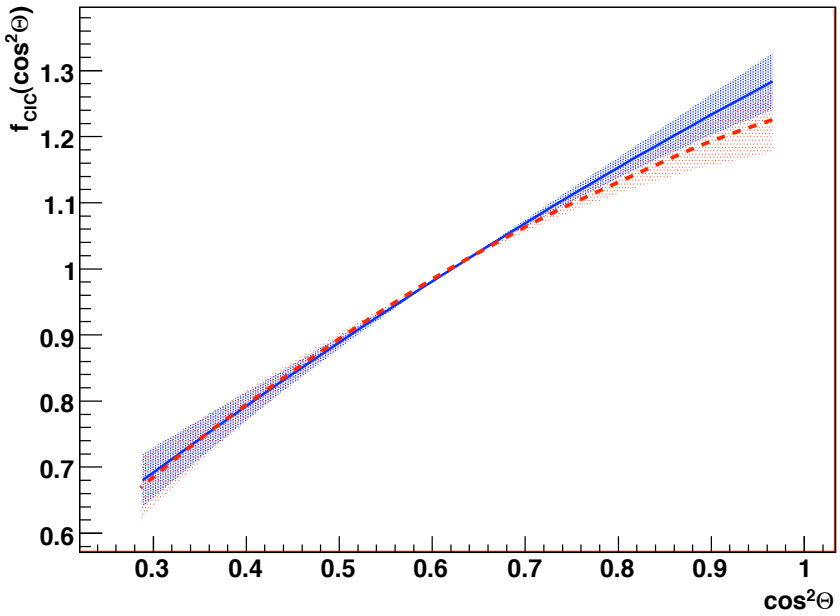

Figure 6.9: Attenuation functions $f_{\mathrm{CIC}}(\cos^2\Theta)$ for winter (solid line) and summer (dashed line) in dependence on $\cos^2\Theta$. The bands illustrate the margins of error. The corresponding energy is $E \approx 7.0$ EeV.

6.4 Weather dependency of the constant intensity cut method results

Because no weather data at higher altitudes is available, the only weather information which can be used are ground data. In this section, the influence of the temperature T, relative humidity H, pressure P and density ρ at ground level on the attenuation function $f_{\mathrm{CIC}}(\cos^2\Theta)$ is analysed. Because of a weather data quality cut, which excludes weather information created by long time interpolation, the number of events analysed decreases to 18261.

The constant intensity cut method is performed with $S(1000)$ data values and additionally with weather corrected S(1000) values, using a method developed in Bariloche [50]. The weather influence on the surface detector and fluorescence detector signals of hybrid events is studied. The influence of the weather on fluorescence detector signals is well known and it is possible to correct for this. But it is much more complicated to correct the surface detector events on weather effects. Therefore the $S(1000)$ of a surface detector event is recalculated to a signal which would have been measured by the fluorescence detector, if the shower had been a hybrid event. The $S(1000)$ signal of the surface detector is converted to the $S(1000)$ at the reference values P_0 and ρ_0. The pressure P_0 and the density ρ_0 are the average values of the whole data taking period. With a calibration curve, the surface detector reference signal is converted into the corresponding fluorescence detector signal, which can be corrected for weather influences. After the weather correction, it is recalculated to $S_{\mathrm{corr}}(1000)$ of the surface detector. The weather corrected $S_{\mathrm{corr}}(1000)$ values can be calculated from the following formula:

$$S_{\mathrm{corr}}(1000) = S_0(1000)\left[1+\alpha_P(P-P_0)+\alpha_\rho(\rho_d-\rho_0)+\beta_\rho(\rho-\rho_d)\right], \tag{6.8}$$

with the signal S_0, measured at reference conditions P_0 and ρ_0 and the daily average value ρ_d.

6.4.1 Temperature

In order to analyse the temperature dependence of the constant intensity cut method results, the data set is sorted concerning their temperatures. Afterwards the data set is divided into three parts, each containing the same number of entries. In Figure 6.10, the temperature distribution of the data set used is shown. The arrows mark the borders of the data subsets, at $T \leq 6.6$ °C and $T \geq 15.5$ °C. Events with temperatures $T \leq 6.6$ °C are compared to $T \geq 15.5$ °C, in order to achieve a maximal effect. The whole data set contains 18261 events, 6087 events are one third. To allow theoretically for the same number of entries in each bin, the first and the third data subsets contain 6090 events, the second, unused data set contains only 6081 events. The histograms of the bin entry numbers are shown in Figure 6.11. The shapes of the distributions differ from each other. Because the statistics of the subsets are lower than of the whole data set, the fluctuations are higher. No temperature dependence is visible.

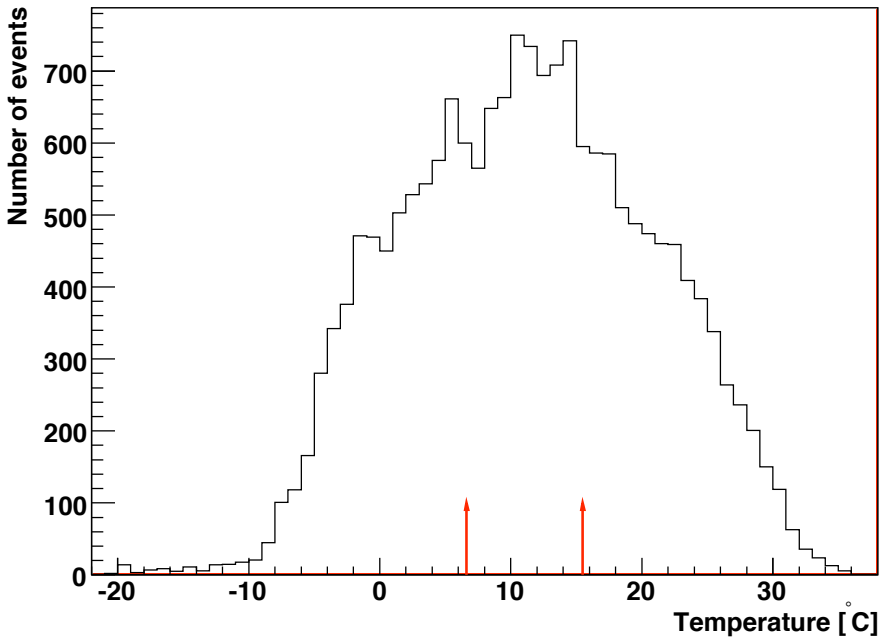

Figure 6.10: Temperature distribution of the data set used. The arrows divide the data set into three equal sized sets.

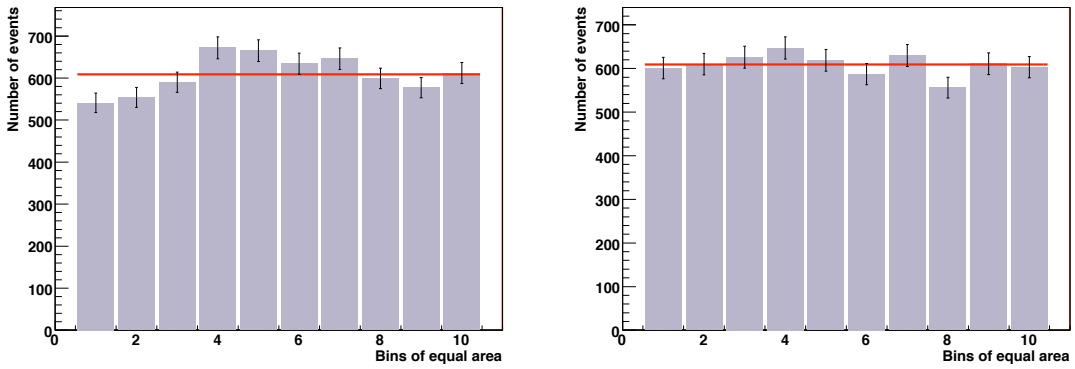

Figure 6.11: Number of events in the equally sized Θ bins. The total number of events is 6090. The lines illustrates the average value $\overline{N} = 609.0$. On the left: Events with temperatures $T \leq 6.6$ °C. On the right: Events with temperatures ≥ 15.5 °C.

The intensity cuts are made at $N_{\text{cut}} = 315$, which corresponds to an energy of $E \approx 4.3$ EeV and at $N_{\text{cut}} = 138$ with the corresponding energy of $E \approx 7.0$ EeV. In Figure 6.12 the attenuation functions of low and high temperature data are plotted for $N_{\text{cut}} = 315$, in Figure 6.14 for $N_{\text{cut}} = 138$, respectively. The divergence between the low and high temperature curves is very small, they agree considering their error bands. Obviously, the temperature has no effect on the constant intensity cut method results of these data subsets. In Table 6.5, the parameters a, b and the error estimator $\sigma_{S_{38^\circ}}$ are listed, in Figures B.15 and B.17 the $S_{\text{CIC}}(1000)$ curves are shown. The same analysis is repeated for the weather corrected signals S_{corr} with the same intensity and temperature cuts. In Figures 6.13 and 6.15, the attenuation functions for $N_{\text{cut}} = 315$ and $N_{\text{cut}} = 138$ are plotted, the parameters are listed in Table 6.6 and the $S_{\text{CIC}}(1000)$ curves are in Appendix B (Figures B.16 and B.18). The weather correction influences $f_{\text{CIC}}(\cos^2\Theta)$ marginally. It is not possible to evaluate, whether the weather correction improves the $S(1000)$ values.

E [EeV]	T [°C]	a	σ_a	b	σ_b	S_{38° [VEM]	$\sigma_{S_{38^\circ}}$ [VEM]
4.3	≤ 6.6	0.987	0.042	-0.11	0.18	22.94	0.27
4.3	≥ 15.5	0.961	0.034	-0.51	0.17	23.39	0.29
4.3	all data	0.944	0.022	-0.50	0.10	23.58	0.15
7.0	≤ 6.6	0.955	0.038	-0.46	0.16	37.52	0.39
7.0	≥ 15.5	0.875	0.043	-0.60	0.19	36.93	0.40
7.0	all data	0.901	0.022	-0.66	0.10	37.60	0.27

Table 6.5: Comparison between low and high temperature events: The attenuation function is given by $f_{\text{CIC}}(x) = 1 + ax + bx^2$, with the parameters a and b in dependence on the temperature T and the energy E. The energy estimator S_{38° is also listed. The constant intensity cut method is performed with $S(1000)$ data values.

E [EeV]	T [°C]	a	σ_a	b	σ_b	S_{38° [VEM]	$\sigma_{S_{38^\circ}}$ [VEM]
4.3	≤ 6.6	0.802	0.034	-0.43	0.18	24.42	0.28
4.3	≥ 15.5	0.748	0.041	-0.45	0.18	22.46	0.24
4.3	all data	0.766	0.025	-0.49	0.13	22.18	0.17
7.0	≤ 6.6	0.801	0.043	-0.68	0.19	38.93	0.41
7.0	≥ 15.5	0.666	0.029	-0.52	0.16	35.82	0.42
7.0	all data	0.706	0.023	-0.56	0.11	35.19	0.27

Table 6.6: Same as Table 6.5, but the constant intensity cut method is performed with weather corrected S(1000) values.

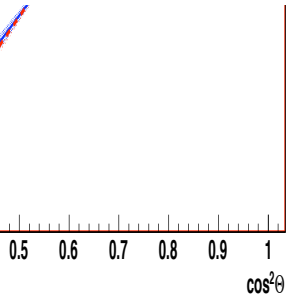

arison of temperature $T \leq 6.6\,^{\circ}\mathrm{C}$ (solid line) and 5.5 °C (dashed line): Attenuation functions of bin $N_{\mathrm{cut}} = 315$, performed with $S(1000)$ data values.

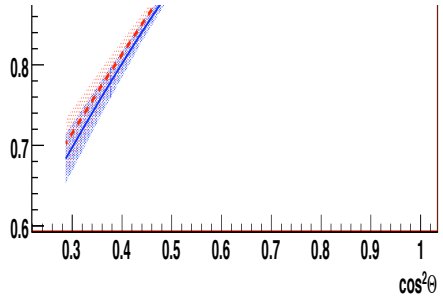

Figure 6.13: Same as Figure 6.12, but performed with weather corrected $S(1000)$ values.

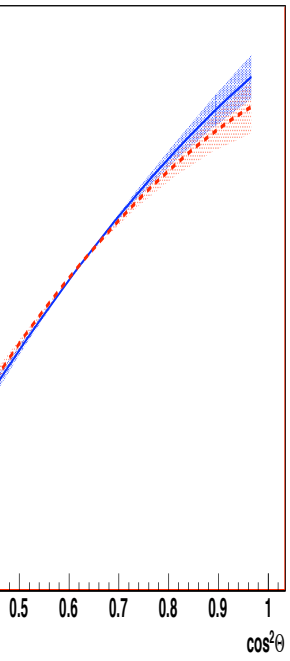

arison of temperature $T \leq 6.6\,^{\circ}\mathrm{C}$ (solid line) and 5.5 °C (dashed line): Attenuation functions of bin $N_{\mathrm{cut}} = 138$, performed with $S(1000)$ data values.

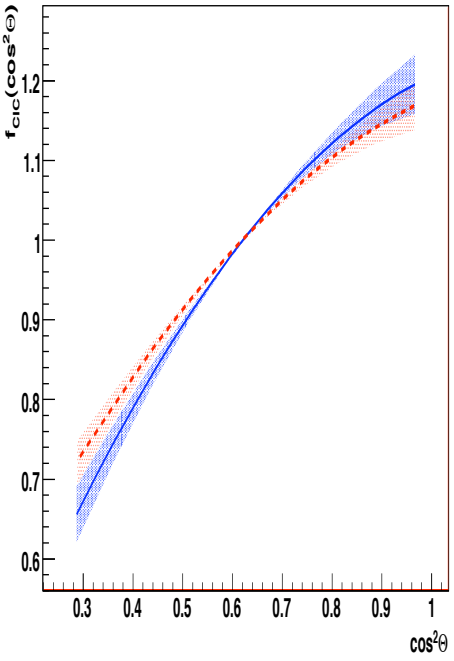

Figure 6.15: Same as Figure 6.14, but performed with weather corrected $S(1000)$ values.

6.4.2 Humidity

The relative humidity is the ratio of the partial pressure of water vapor to the saturated partial pressure of water vapor at the same temperature. It influences the atmospheric depth and therefore the development of the shower. In Figure 6.16, the event distribution is plotted in dependence on the humidity. To analyse the influence of the humidity, the data set is divided into three equally sized subsets. The events with a relative humidity $H \leq 34.92\%$ and events with $H \geq 76.80\%$ are compared. The number of low humidity and high humidity events is 6090, because of the same reasons mentioned in Section 6.6. In Figure 6.17 the number of entries in each bin is illustrated. The distributions differ marginally.

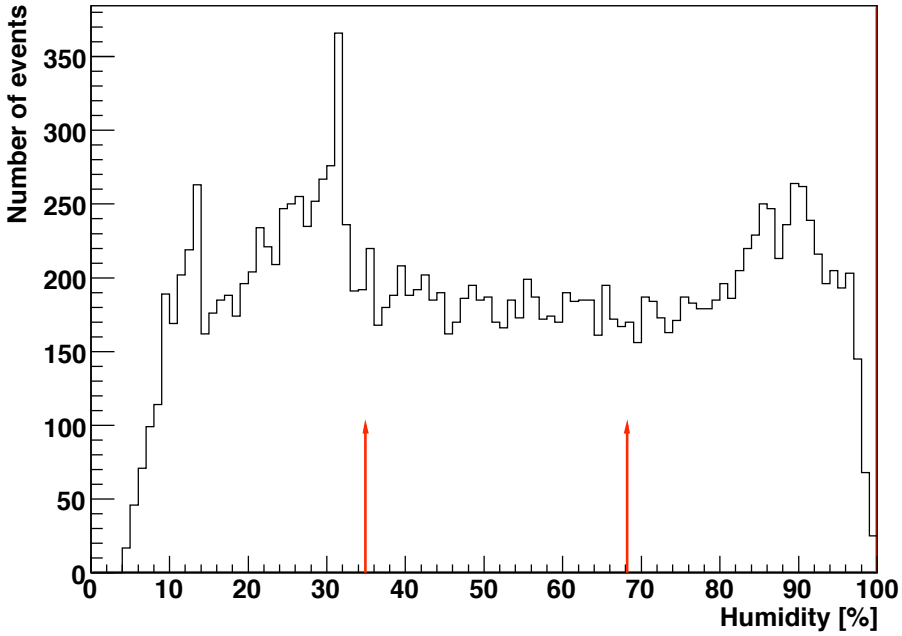

Figure 6.16: Humidity distribution of the data set used. The arrows divide the data set into three equal sized sets.

In Figures 6.18 and 6.20, the attenuation functions of $S_{\mathrm{CIC}}(1000)$ data values are illustrated. The differences between low and high humidity curves are low. In Table 6.7, there are no high divergences, either. Because of low statistics and the resulting errors it is not possible to see any humidity dependence. The same is obtained for the weather corrected values, as shown in Figures 6.18 and 6.20 and in Table 6.8.

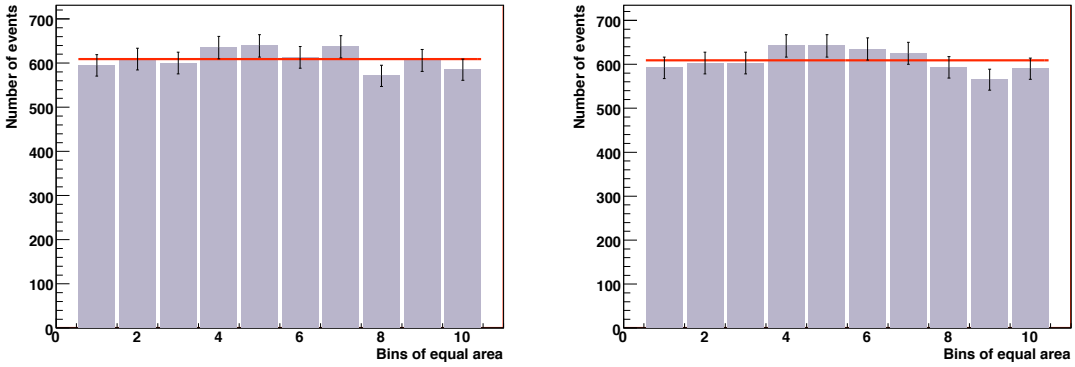

Figure 6.17: Number of events in the equally sized Θ bins. The total number of events is 6090. The horizontal line illustrates the average value $\overline{N} = 609.0$. On the left: Events with humidity $H \leq 34.92\%$. On the right: Events with humidity $H \geq 76.80\%$.

E [EeV]	H [%]	a	σ_a	b	σ_b	S_{38° [VEM]	$\sigma_{S_{38^\circ}}$ [VEM]
4.3	≤ 34.92	0.948	0.031	-0.43	0.15	23.15	0.25
4.3	≥ 76.80	1.021	0.037	-0.05	0.17	22.81	0.27
4.3	all data	0.944	0.022	-0.50	0.10	23.58	0.15
7.0	≤ 34.92	0.827	0.035	-1.07	0.15	37.39	0.40
7.0	≥ 76.80	0.990	0.030	-0.70	0.16	37.50	0.46
7.0	all data	0.901	0.022	-0.66	0.10	37.60	0.27

Table 6.7: Comparison between events of low and high humidity: The attenuation function is given by $f_{\mathrm{CIC}}(x) = 1 + ax + bx^2$, with the parameters a and b in dependence on the humidity H and the energy E. The energy estimator S_{38° is also listed. The constant intensity cut method is performed with $S(1000)$ data values.

E [EeV]	H [%]	a	σ_a	b	σ_b	S_{38° [VEM]	$\sigma_{S_{38^\circ}}$ [VEM]
4.3	≤ 34.92	0.754	0.033	-0.66	0.15	22.83	0.21
4.3	≥ 76.80	0.759	0.037	-0.38	0.19	23.73	0.26
4.3	all data	0.766	0.025	-0.49	0.13	22.18	0.17
7.0	≤ 34.92	0.674	0.028	-0.75	0.17	34.36	0.49
7.0	≥ 76.80	0.780	0.033	-0.76	0.15	38.38	0.35
7.0	all data	0.706	0.023	-0.56	0.11	35.19	0.27

Table 6.8: Same as Table 6.7, but the constant intensity cut method is performed with weather corrected S(1000) values.

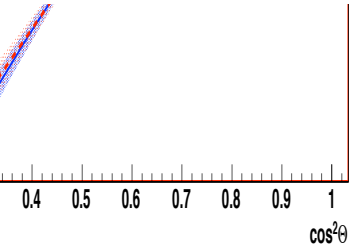

Comparison of humidity $H \leq 34.92\%$ (solid line) and $H \geq 76.80\%$ (dashed line): Attenuation functions for bin entry $N_{cut} = 315$, performed with $S(1000)$ data values.

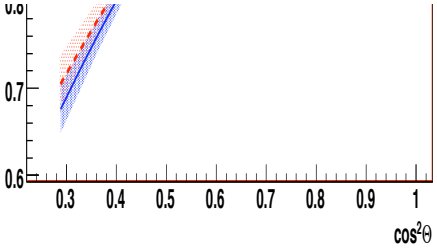

Figure 6.19: Same as Figure 6.18, but performed with weather corrected $S(1000)$ values.

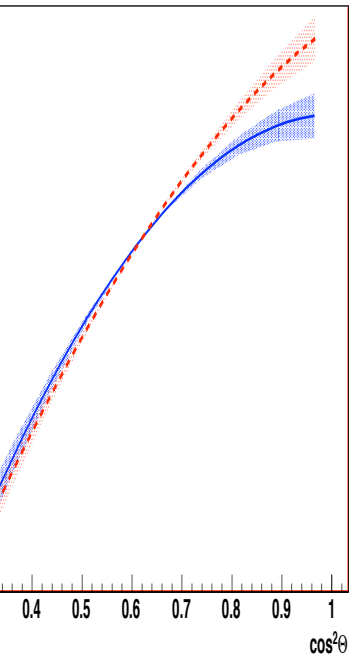

Comparison of humidity $H \leq 34.92\%$ (solid line) and $H \geq 76.80\%$ (dashed line): Attenuation functions for bin entry $N_{cut} = 138$, performed with $S(1000)$ data values.

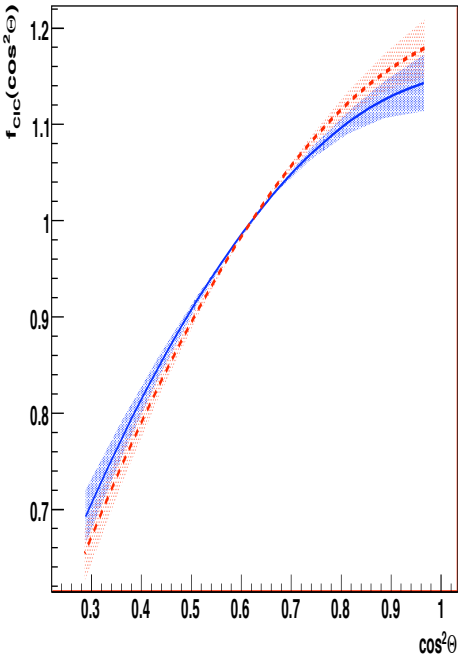

Figure 6.21: Same as Figure 6.20, but performed with weather corrected $S(1000)$ values.

6.4.3 Pressure

Figure 6.22 shows the distribution for the pressure P at ground level. The pressure P at ground level is an indicator for the density integrated over the whole atmosphere. Therefore it influences the age of a shower at ground level. In order to investigate the influence of pressure P, 6090 events with $P \leq 860.14$ hPa are compared to 6090 events with $P \geq 863.56$ hPa. In Figure 6.23 the distributions of the number of bin entries are shown, in dependence on the pressure. The differences are due to fluctuations. The constant intensity cut method is also independent of the pressure. In Figures 6.24 to 6.27 the attenuation functions are shown and in Appendix B the $S_{\mathrm{CIC}}(1000)$ curves are fitted (Figures 6.24 to 6.27). The attenuation curves agree with each other, considering their error bands. No pressure dependency is visible in the constant intensity cut method results. The parameters are given in Tables 6.9 and 6.9. Also here no noticeable deviations are visible.

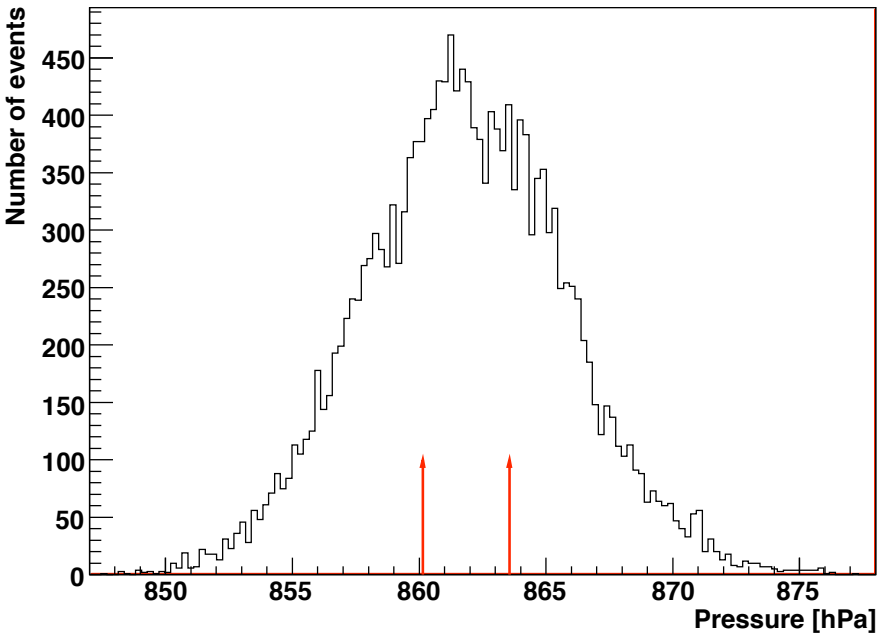

Figure 6.22: Pressure distribution of the used data set. The arrows divide the data set into three equal sized sets.

6.4.4 Density

The depth of the shower maximum X_{max} depends on the density ρ. The higher the density, the higher is the altitude of X_{max}, because the mean free path length between the atoms is smaller. In Figure 6.28, the density distribution is plotted. In order to investigate the effect of the density ρ, the data set is divided into three parts, marked by the arrows. 6090 events with $\rho \leq 1.038$ kg/m^3 and 6090 events with $\rho \geq 1.073$ kg/m^3 are compared, to get a maximum effect. In Figure 6.29 the distributions of bin entries are shown, it is no

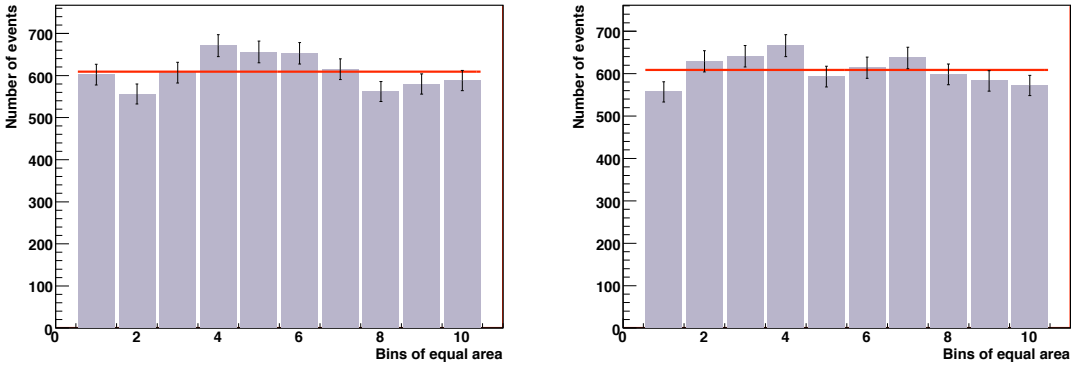

Figure 6.23: Number of events in the equally sized Θ bins. The total number of events is 6090. The horizontal line illustrates the average value $\overline{N} = 609.0$. On the left: Events with pressure $P \leq 860.14$ hPa. On the right: Events with pressure $P \leq 863.56$ hPa.

E [EeV]	P [hPa]	a	σ_a	b	σ_b	S_{38° [VEM]	$\sigma_{S_{38^\circ}}$ [VEM]
4.3	≤ 860.14	0.921	0.044	-0.63	0.21	23.30	0.29
4.3	≥ 863.56	0.947	0.044	-0.38	0.20	23.41	0.28
4.3	all data	0.944	0.022	-0.50	0.010	23.58	0.15
7.0	≤ 860.14	0.879	0.029	-1.03	0.13	37.37	0.40
7.0	≥ 863.56	0.898	0.029	-0.84	0.14	37.43	0.32
7.0	all data	0.901	0.022	-0.66	0.10	37.60	0.27

Table 6.9: Comparison between events of low and high pressure: The attenuation function is given by $f_{\mathrm{CIC}}(x) = 1 + ax + bx^2$, with the parameters a and b in dependence on the pressure P and the energy E. The energy estimator S_{38° is also listed. The constant intensity cut method is performed with $S(1000)$ data values.

E [EeV]	P [hPa]	a	σ_a	b	σ_b	S_{38° [VEM]	$\sigma_{S_{38^\circ}}$ [VEM]
4.3	≤ 860.14	0.792	0.038	-0.58	0.18	22.81	0.25
4.3	≥ 863.56	0.701	0.035	-0.46	0.20	24.02	0.27
4.3	all data	0.766	0.025	-0.49	0.13	22.18	0.17
7.0	≤ 860.14	0.755	0.035	-0.64	0.17	35.47	0.41
7.0	≥ 863.56	0.636	0.027	-0.54	0.14	37.98	0.39
7.0	all data	0.706	0.023	-0.56	0.11	35.19	0.27

Table 6.10: Same as Table 6.9, but the constant intensity cut method is performed with weather corrected S(1000) values.

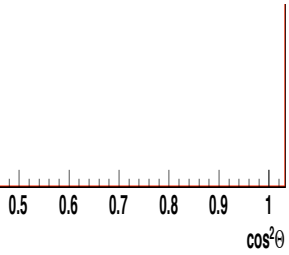

arison of pressure $P \leq 860.14$ hPa (solid line) and
63.56 hPa (dashed line): Attenuation functions
entry $N_{cut} = 315$, performed with $S(1000)$ data
.

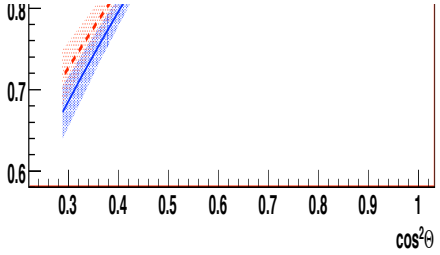

Figure 6.25: Same as Figure 6.24, but performed with weather corrected $S(1000)$ values.

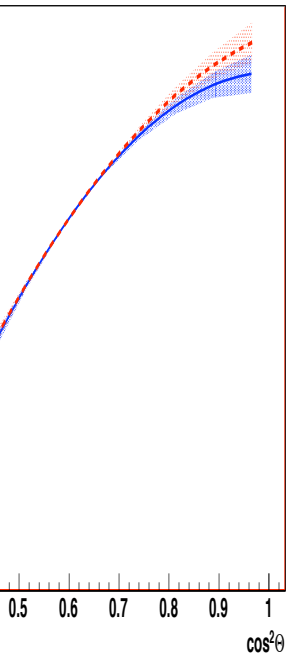

arison of pressure $P \leq 860.14$ hPa (solid line) and
63.56 hPa (dashed line): Attenuation functions
entry $N_{cut} = 138$, performed with $S(1000)$ data
.

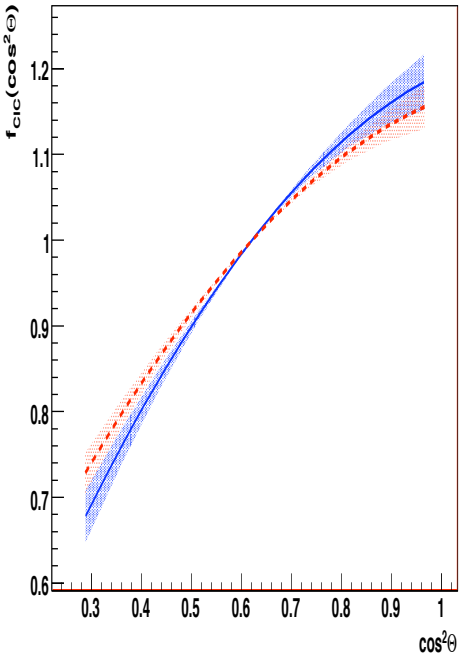

Figure 6.27: Same as Figure 6.26, but performed with weather corrected $S(1000)$ values.

abnormal shape visible. The attenuation curves, Figures 6.30 to 6.33 agree with each other, too. Considering the errors, no density dependence is noticeable. The $S_{\mathrm{CIC}}(1000)$ curves, Figures B.27 to B.30, are shown in Appendix B. The parameters a and b and the energy estimator S_{38° are listed in Tables 6.11 and 6.12. The parameter a of the weather corrected $S(1000)$ values has a difference of 2σ at energies of $E \approx 4.3$ EeV and of 4σ at energies of $E \approx 7.0$ EeV. Therefore the fluctuations of the energy estimator S_{38° are also higher. But also here no systematic density dependence is recognisable.

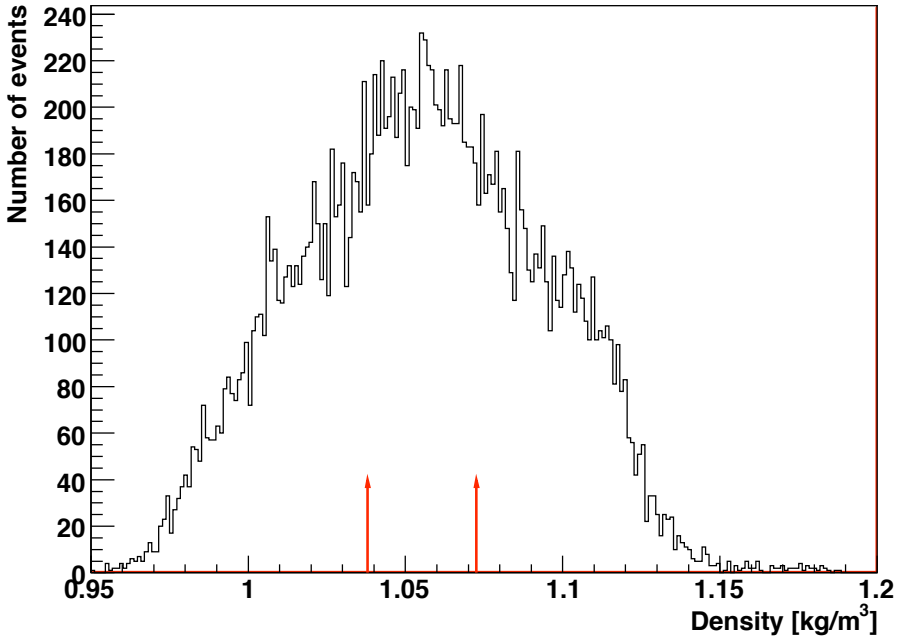

Figure 6.28: Density distribution of the data set used. The arrows divide the data set into three equally sized sets.

6.5 Distance dependency of the constant intensity cut method

6.5.1 Distance to the shower axis

Because the signal S is measured as a function of the distance to the shower axis, the distance between the central station and the shower axis can affect the quality of the LDF fit and therefore the constant intensity cut method results. In Figure 6.35, the distribution of the distance d_{axis} between the central station and the shower axis is plotted. It becomes obvious that almost no events with a distance $d_{\mathrm{axis}} \leq 100$ m are measured. The reconstruction fails for over-saturated stations and therefore events with the shower core close to a station are not reconstructed [51]. Figure 6.5.1 shows the zenith angle distributions

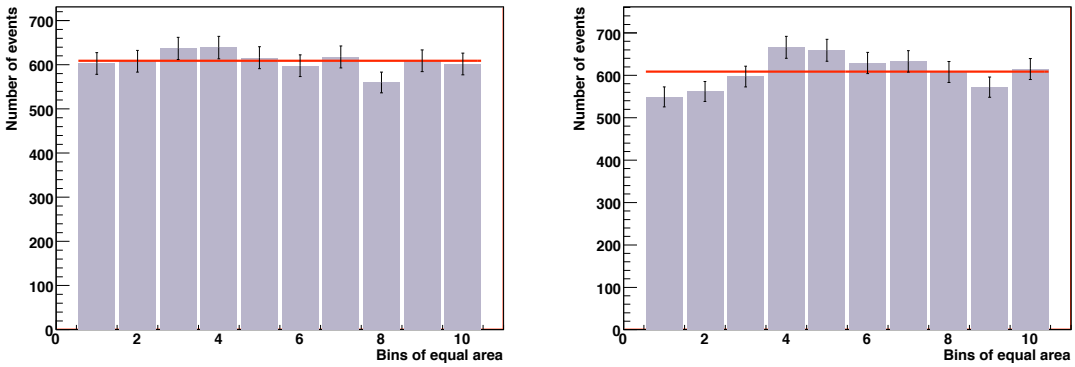

Figure 6.29: Number of events in the equally sized Θ bins. The total number of events is 6090. The line illustrates the average value $\overline{N} = 609.0$. On the left: Events with density $\rho \leq 1.038$ kg/m^3. On the right: Events with density $\rho \geq 1.073$ kg/m^3.

E [EeV]	ρ [kg/m^3]	a	σ_a	b	σ_b	S_{38° [VEM]	$\sigma_{S_{38^\circ}}$ [VEM]
4.3	≤ 1.038	0.948	0.032	-0.46	0.17	23.30	0.28
4.3	≥ 1.073	0.964	0.040	-0.16	0.18	23.00	0.25
4.3	all data	0.944	0.022	-0.50	0.10	23.58	0.15
7.0	≤ 1.038	0.930	0.037	-0.60	0.17	36.82	0.46
7.0	≥ 1.073	0.941	0.040	-0.58	0.18	37.78	0.39
7.0	all data	0.901	0.022	-0.66	0.10	37.60	0.27

Table 6.11: Comparison between events of low and high density: The attenuation function is given by $f_{\mathrm{CIC}}(x) = 1 + ax + bx^2$, with the parameters a and b in dependence on the density ρ and the energy E. The energy estimator S_{38° is also listed. The constant intensity cut method is performed with $S(1000)$ data values.

E [EeV]	ρ [kg/m^3]	a	σ_a	b	σ_b	S_{38° [VEM]	$\sigma_{S_{38^\circ}}$ [VEM]
4.3	≤ 1.038	0.765	0.037	-0.38	0.18	22.26	0.25
4.3	≥ 1.073	0.810	0.031	-0.33	0.16	23.99	0.26
4.3	all data	0.766	0.025	-0.49	0.13	22.18	0.17
7.0	≤ 1.038	0.690	0.038	-0.29	0.20	35.09	0.48
7.0	≥ 1.073	0.814	0.041	-0.58	0.19	38.51	0.51
7.0	all data	0.706	0.023	-0.56	0.11	35.19	0.27

Table 6.12: Same as Table 6.11, but the constant intensity cut method is performed with weather corrected S(1000) values.

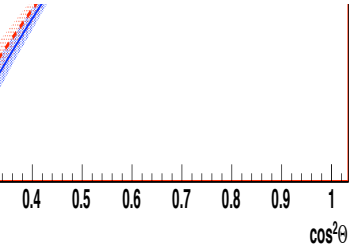

Comparison of density $\rho \leq 1.038$ kg/m^3 (solid line) and $\rho \geq 1.073$ kg/m^3 (dashed line): Attenuation functions for bin entry $N_{cut} = 315$, performed with $S(1000)$ data values.

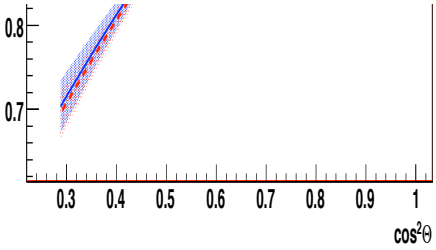

Figure 6.31: Same as Figure 6.30, but performed with weather corrected $S(1000)$ values.

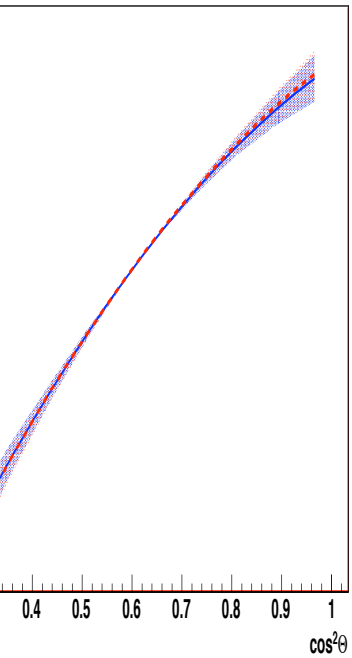

Comparison of density $\rho \leq 1.038$ kg/m^3 (solid line) and $\rho \geq 1.073$ kg/m^3 (dashed line): Attenuation functions for bin entry $N_{cut} = 138$, performed with $S(1000)$ data values.

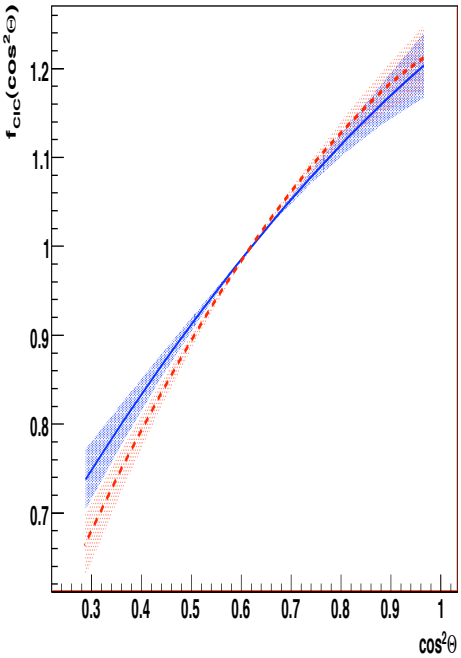

Figure 6.33: Same as Figure 6.32, but performed with weather corrected $S(1000)$ values.

of events with distances $d \leq 379.0$ m and $d \geq 563.9$ m and Figure 6.5.1 shows the corresponding numbers of bin entries in each bin. For axis distances $d \leq 379.0$ m the number of events with zenith angles between $\Theta = 38$ °C and $\Theta = 60$ °C is much higher than for events with axis distances $d \geq 563.9$ m. The reason for this is a geometrical effect, described in Figure 6.34. The distance between the central station and the shower axis is larger for a vertical event than for an event with the zenith angle $\Theta \gg 0$ and the same core position. The following relation is given:

$$d_{\text{axis}}(\Theta) = d_{\text{axis}}(\Theta = 0) \cdot \cos(\Theta). \tag{6.9}$$

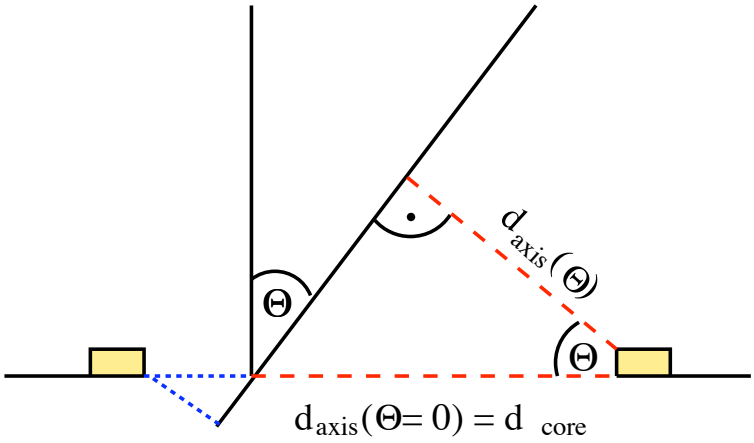

Figure 6.34: d_{axis} is the perpendicular distance between the shower axis and the tank with the highest measured signal (dotted lines). An event with a zenith angle $\Theta = 0°$ and one with $\Theta > 0°$ are illustrated. The distance d_{axis} for an inclined event is shorter by the factor of $\cos(\Theta)$ than for vertical events with the same core position.

Because of the different zenith angle distributions and the resulting differences in the number of bin entries, the constant intensity cut method does not work. It is more reasonable to analyse the influence of the distance between the central station and the shower core. The value of the core distance d_{core} follows from Equation 6.9:

$$d_{\text{core}} = d_{\text{axis}}(\Theta = 0) = \frac{d_{\text{axis}}(\Theta)}{\cos(\Theta)}. \tag{6.10}$$

6.5.2 Distance to shower core

The influence of the shower core distance d_{core}, given by Equation 6.10, on the constant intensity cut method results is analysed in this section. Figure 6.39 shows the distribution of the core distances. As explained in Section 6.5.1 almost no events with the core nearby a station are reconstructed, because of over-saturated signals. Therefore, the number of events increases for distances of $d_{\text{core}} \lesssim 100$ m. At $d_{\text{core}} \gtrsim 750$ m the number of events decreases and reaches nearly zero at 866 m. As described in Figure 6.38, the centre of a

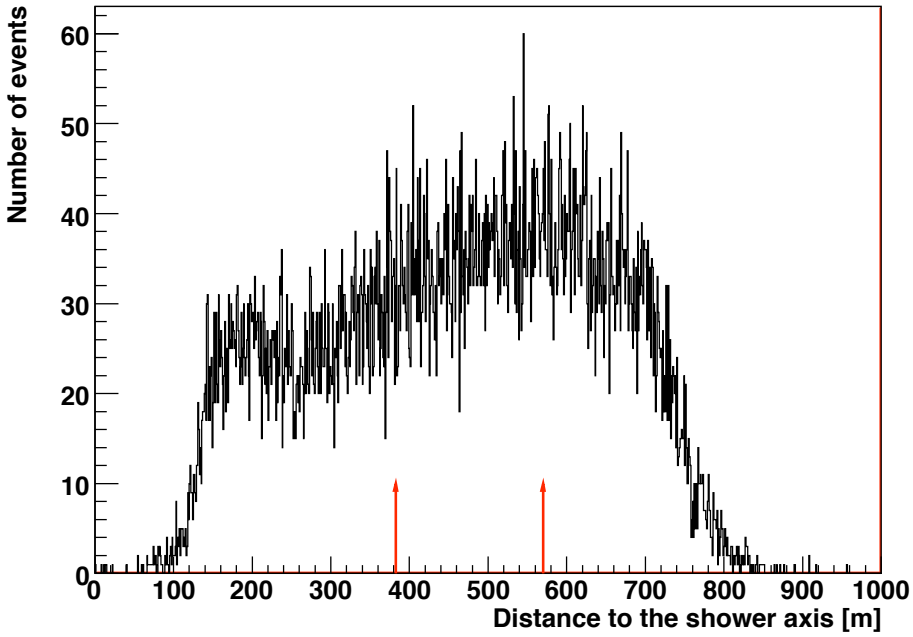

Figure 6.35: Distribution of the distance between the shower axis and the central station. The arrows divide the data set into three equally sized sets.

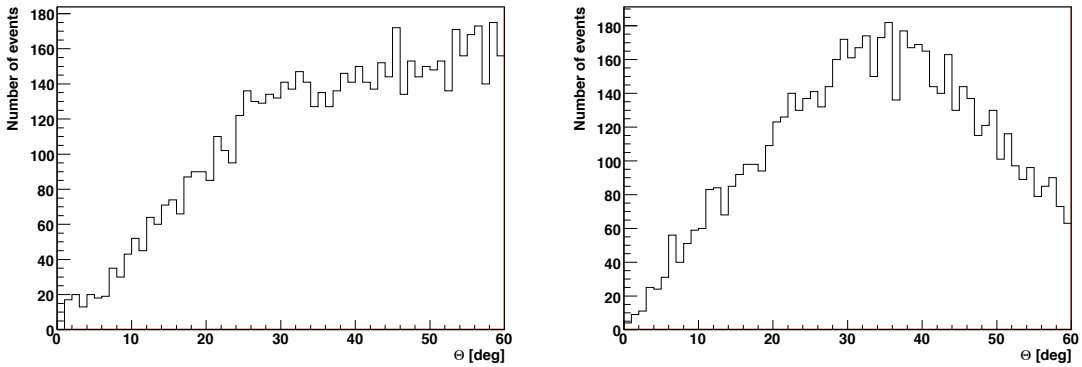

Figure 6.36: Zenith angle distribution of events with a shower axis distance $d_{\text{axis}} \leq 379.0$ m (left) and $d_{\text{axis}} \geq 563.9$ m (right).

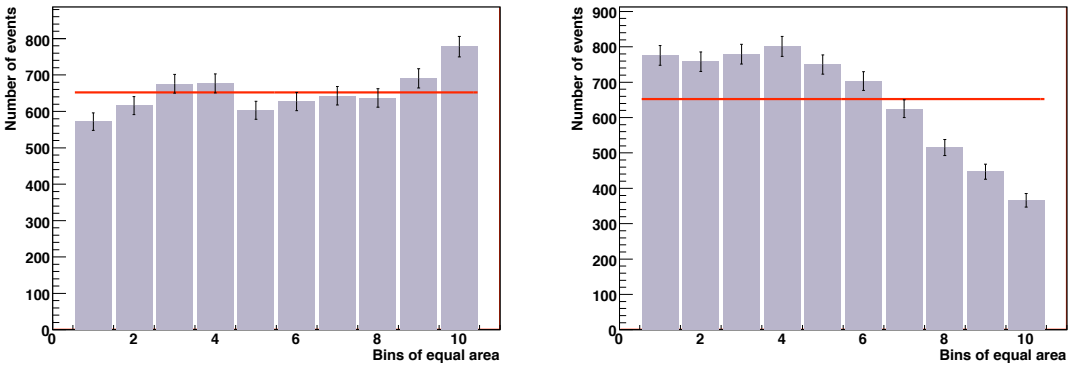

Figure 6.37: Number of events in the equally sized Θ bins. The total number of events is 6520. The horizontal line illustrates the average value $\overline{N} = 652.0$. On the left: Events with a distance to the shower axis of $d_{\text{axis}} \leq 379.0$ m: On the right: Events with a distance to the shower axis of $d_{\text{axis}} \geq 563.9$ m.

triangle of surface detectors has an ideal distance of 866 m to each station, which is the maximal distance

$$d_{\text{max}} = \frac{1500 \text{ m}/2}{\sin(60\,^\circ)} = \frac{1500 \text{ m}/2}{\cos(30\,^\circ)} = 866.025 \text{ m}. \tag{6.11}$$

The events with core distances larger than $d_{\text{core}} = 866$ m are due to fluctuations of to the 1500 m spacing. For geographic reasons, like rivers or canyons, it was not possible to install all stations with a distance of exactly 1500 m from each other. Some stations are shifted and therefore the maximal distance differs from 866 m.

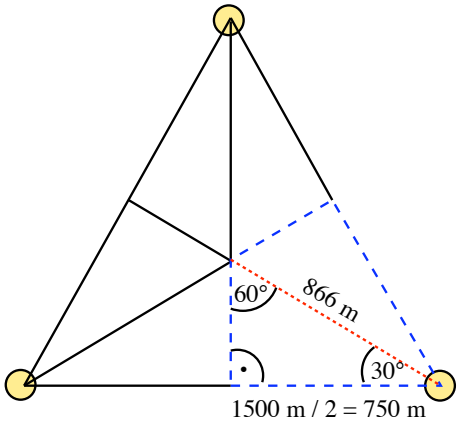

Figure 6.38: The surface detector station in the lower right corner is the nearest tank, if the core is located inside the dashed edge. The maximal core distance $d_{\text{core}} = 866$ m is marked with the dotted line.

The data set used consists of 19563 events and is divided into three parts, events with a core distance $d_{\text{core}} \leq 441.0$ m, $441.0 \text{ m} > d_{\text{core}} > 664.2$ m and $d_{\text{core}} \geq 664.2$ m. In order to get a visible effect, only events with $d_{\text{core}} \leq 441.0$ m and $d_{\text{core}} \geq 664.2$ m

are compared, both sub data sets contain 6520 events. In Figure 6.5.2 the zenith angle distributions are shown and the numbers of bin entries are illustrated in Figure 6.5.2. The Θ distributions differ from each other. The mean of the distribution of small core distances is $\overline{\Theta} = 35.5\,^{\circ}$, the mean value of high core distances is $\overline{\Theta} = 36.7\,^{\circ}$. Both distributions exhibit fluctuations, but the mean Θ value of each bins i of the low distance distribution agrees with the mean value of the corresponding bin i of the high distance distribution. Because of low differences, the constant intensity cut method can be performed.

The intensity cuts are at $N_{\mathrm{cut}} = 338$ and $N_{\mathrm{cut}} = 148$, corresponding to the energies $E \approx 4.3$ EeV and $E \approx 7.0$ EeV. In Figures 6.42 and 6.43 the attenuation functions of low core distance and high core distance events are plotted, the $S_{\mathrm{CIC}(1000)}$ curves are shown in Figures B.31 and B.32 in Appendix B. No core distance dependence is noticeable. Also the parameters a and b, as well as the energy estimator $S_{38^{\circ}}$ do not show any systematical effect. The core distance does not influence the results of the constant intensity cut method.

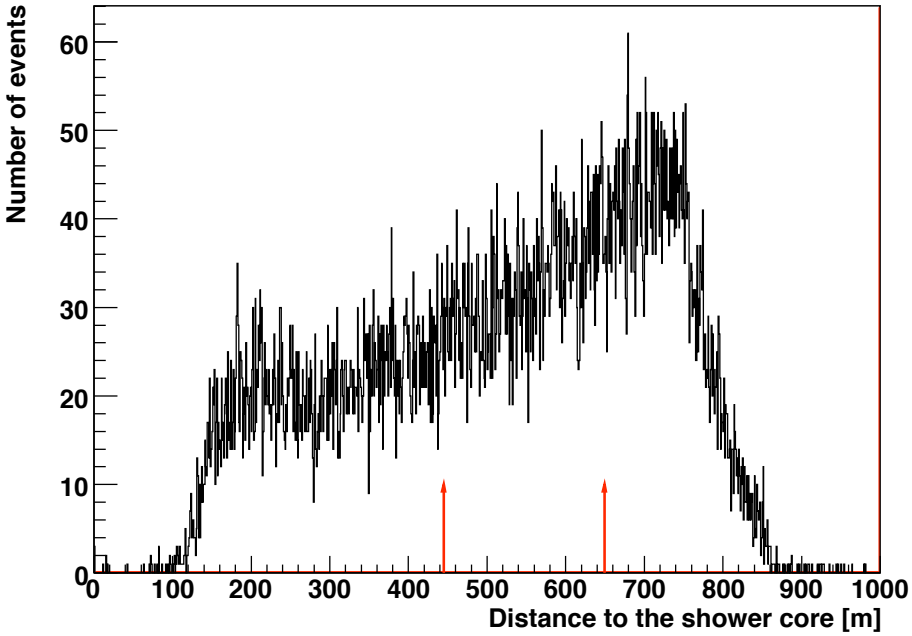

Figure 6.39: Distribution of the distance between the shower core and the central station . The arrows divide the data set into three equally sized sets.

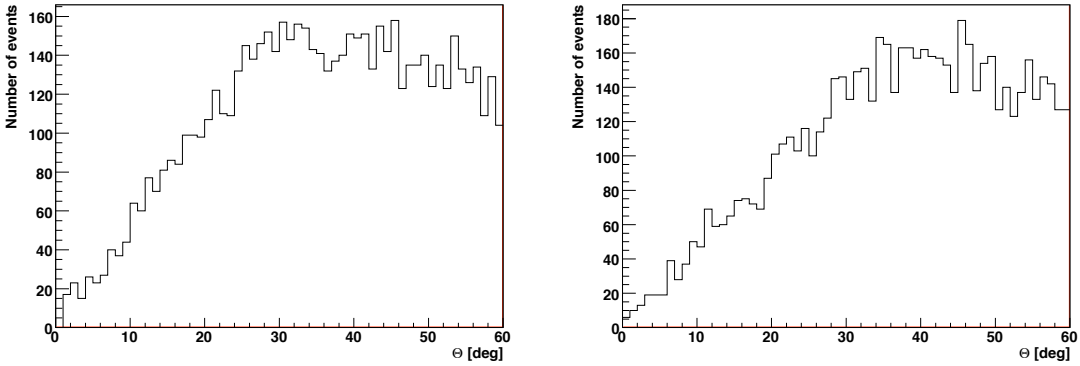

Figure 6.40: Zenith angle distribution of events with a core distance $d_{\text{core}} \leq 441.0$ m and a mean zenith angle of $\overline{\Theta} = 35.50\,^{\circ}$ (left) and $d_{\text{core}} \geq 664.2$ m and a mean zenith angle of $\overline{\Theta} = 36.78\,^{\circ}$ (right).

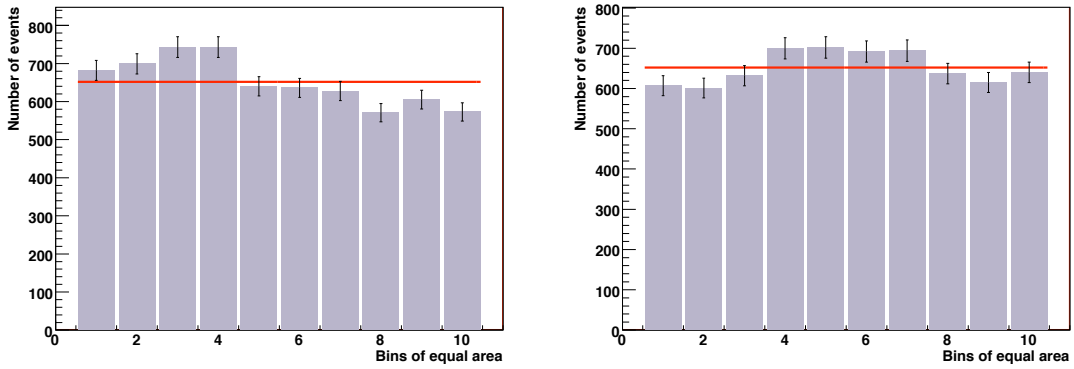

Figure 6.41: Number of events in the equally sized Θ bins. The total number of events is 6520. The horizontal line illustrates the average value $\overline{N} = 652.0$. On the left: Events with a distance to the shower core of $d_{\text{core}} \leq 441.0$ m: On the right: Events with a distance to the shower core of $d_{\text{core}} \geq 664.2$ m.

E [EeV]	d_{core} [m]	a	σ_a	b	σ_b	S_{38° [VEM]	$\sigma_{S_{38^\circ}}$ [VEM]
4.3	≤ 441.0	0.916	0.036	-0.664	0.177	23.861	0.239
4.3	≥ 664.2	0.894	0.033	-0.734	0.146	23.790	0.243
4.3	all data	0.944	0.022	-0.504	0.099	23.581	0.146
7.0	≤ 441.0	0.873	0.033	-1.282	0.179	39.065	0.521
7.0	≥ 664.2	0.837	0.033	-0.892	0.160	37.013	0.443
7.0	all data	0.901	0.022	-0.663	0.103	37.596	0.269

Table 6.13: Comparison between events of low and high core distance: The attenuation function is given by $f_{\text{CIC}}(x) = 1 + ax + bx^2$, with the parameters a and b in dependence on the pressure P and the bin entry N_{cut}. The energy estimator S_{38° is also listed.

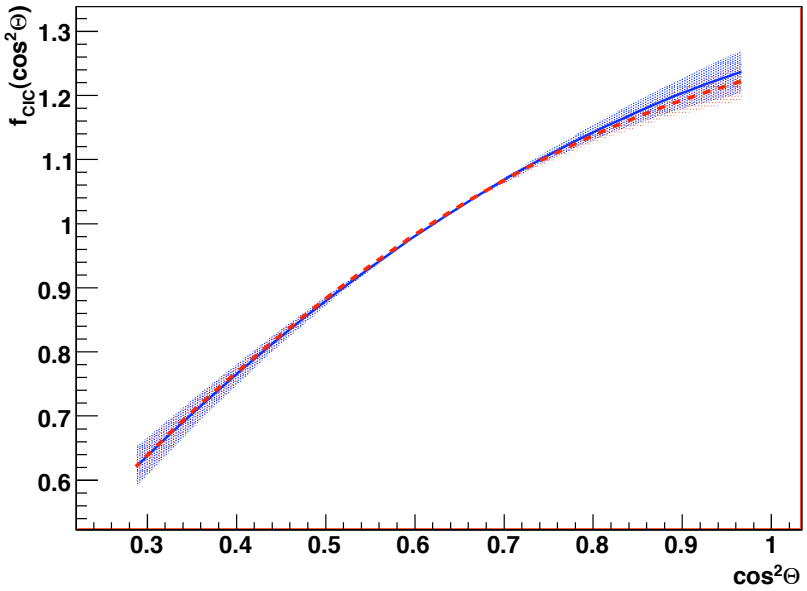

Figure 6.42: Comparison of core distance $d_{\text{core}} \leq 441.0$ m (solid line) and $d_{\text{core}} \geq 664.2$ m (dashed line): Attenuation functions of bin entry $N_{\text{cut}} = 338$.

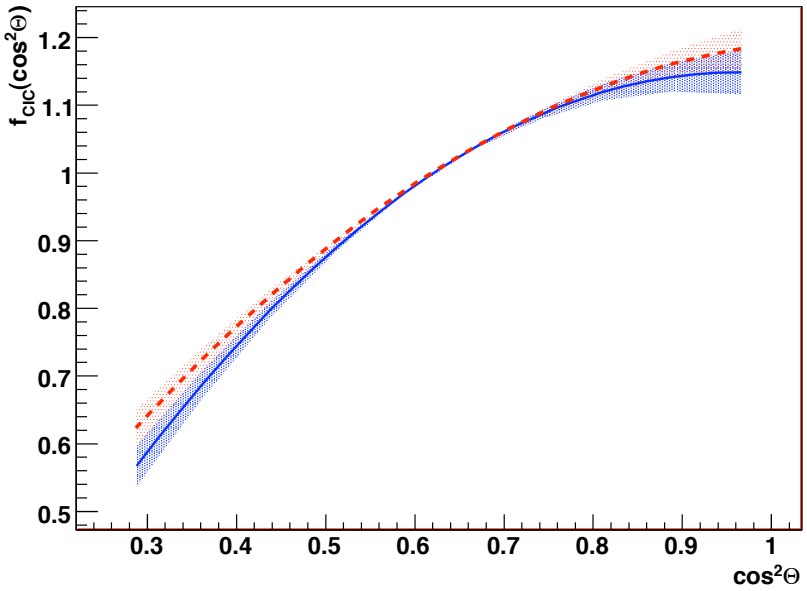

Figure 6.43: Comparison of core distance $d_{\text{core}} \leq 441.0$ m (solid line) and $d_{\text{core}} \geq 664.2$ m (dashed line): Attenuation functions of bin entry $N_{\text{cut}} = 148$.

Chapter 7

Summary and outlook

The aim of this thesis was to develop an ansatz for the constant intensity cut method, in order to calibrate the energy measured by the surface detector of the Pierre Auger Observatory. Furthermore the constant intensity cut method results have been analysed with respect to weather dependencies.

The signal $S(1000)$, measured by the surface detector, is a function of the energy E and the zenith angle Θ. In order to extract the energy information, the constant intensity cut method is performed. In Chapter 5, a new constant intensity cut method approach is developed and described in detail. Assuming an isotropic flux for all energies, the intensity is uniformly distributed by sorting the $S(1000)$ values into bins of the same area in $\cos^2\Theta$. For each bin, equally numbered $S_{\mathrm{CIC}}(1000)$ values, corresponding to a particular constant intensity, are chosen and plotted versus $\cos^2\Theta$. With this method, the surface detector signal $S(1000)$ is separated into the zenith angle Θ depending attenuation function $f_{\mathrm{CIC}}(\cos^2\Theta)$ and the energy estimator $S_{38^\circ}(E)$. The following relation allows to determine the energy estimator $S_{38^\circ}(E)$ from the signal $S(1000)$ at a given zenith angle Θ:

$$S_{38^\circ}(E) = \frac{S_{\mathrm{CIC}}(1000)}{f_{\mathrm{CIC}}(\cos^2\Theta)}.$$

Because the number of entries in the $\cos^2\Theta$ bins is not distributed uniformly, but shows a slight sine-like shape, the chosen entries are corrected regarding the average bin entry value. This correction leads to a more accurate fit. For the estimation of the statistical error of $S_{\mathrm{CIC}}(1000)$, both the influence of possible $S(1000)$ and of Θ fluctuations are taken into account. The error of the attenuation function

$$f_{\mathrm{CIC}}(\cos^2\Theta) = 1 + a(\cos^2\Theta - \cos^2 38^\circ) + b(\cos^2\Theta - \cos^2 38^\circ)^2$$

is calculated from the covariance matrix, since the parameters a, b and the energy estimator $S_{38^\circ}(E)$ are correlated.

In addition two systematic studies were performed. Any influence of the binning on the constant intensity cut method results could be excluded. The shift of the zenith angle Θ to $\Theta_+ = \Theta + 1^\circ$ or $\Theta_- = \Theta - 1^\circ$, influences the results only marginally. Within their errors, the modified attenuation functions $f_{\mathrm{CIC}}(\cos^2\Theta)$ agree with each other.

The constant intensity cut method results are analysed in Chapter 6. First of all, the energy independence of the attenuation function $f_{\mathrm{CIC}}(\cos^2\Theta)$ is investigated. As it is expected, no energy dependence is visible. The calculation of attenuation functions for several energies are used to determine the weighted mean values of the parameters a and b. The following attenuation function $f_{\mathrm{CIC}}(\cos^2\Theta)$ results from this investigation:

$$f_{\mathrm{CIC}}(\cos^2\Theta) = 1 + (0.939 \pm 0.008)x - (0.58 \pm 0.04)x^2, \tag{7.1}$$

with $x = \cos^2\Theta - \cos^2 38^\circ$. The errors of the averaged parameters $\overline{a}$ and $\overline{b}$ are strongly underestimated, because the correlations between the attenuation functions at different energies are not considered. The determination of the non diagonal entries of the covariance matrixes V^a_{ij} and V^b_{ij} is very complex and is beyond the scope of this thesis. It would be meaningful, to discuss these correlations in further studies, in order to evaluate an average attenuation function.

Since the ansatz of the constant intensity cut method differs from other constant intensity cut methods performed with Pierre Auger data before [52], it can be used to verify former results. The following attenuation function was presented in the ICRC report [53]:

$$f^{\mathrm{ICRC}}_{\mathrm{CIC}}(\cos^2\Theta) = 1 + (0.94 \pm 0.06)x - (1.21 \pm 0.27)x^2. \tag{7.2}$$

Figure 7.1 shows the comparison of both attenuation functions. Due to the underestimated errors of the determined attenuation function, the curves do not agree. If the errors $\sigma_{\overline{a}}$ and $\sigma_{\overline{b}}$ would be evaluated in the same order of magnitude like for the function given in Equation 7.2, the attenuation curves would be consistent.

In Chapter 6, events with distances $d_{\mathrm{core}} \lesssim 100$ m and $d_{\mathrm{core}} \gtrsim 750$ m are compared. It is found out, that the constant intensity cut method results are not influenced by the distance d_{core} between the shower core and the surface detector station with the highest signal.

Furthermore, the influences of different weather conditions on the constant intensity cut method results are investigated. The weather parameters analysed are temperature, humidity, pressure and density, since they are expected to affect the atmosphere's conditions and, therefore, the development of extensive air showers. The events are sorted according to the weather parameters and afterwards two different extremal subsets for each weather parameter are compared in order to obtain visible effects. In order to achieve sufficiently high statistics, the data subsets are subdivided into three parts, of which the outer two subsets actually are used. A separation into subsets with higher differences would show a larger effect, but with lower statistics. Therefore, as a compromise, the compared parameter differences are low, but with high statistics. Within these subsets, for none of the weather parameters any significant influence on the constant intensity cut method results is visible. It would be interesting to repeat these weather studies for a larger data set again. Then it would be possible to select data subsets with larger differences in the weather parameters with comparable statistics.

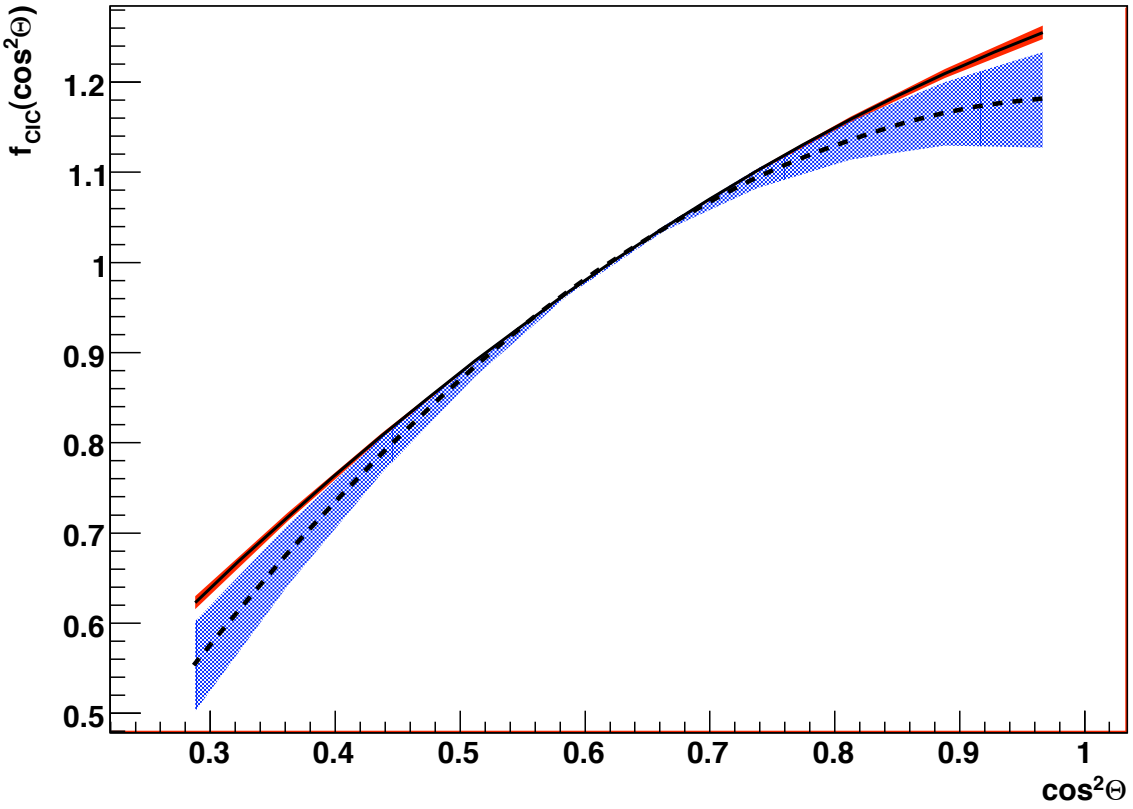

Figure 7.1: Comparison of the averaged attenuation function $f_{\mathrm{CIC}}(\cos^2\Theta)$, obtained in this thesis (solid line), and $f_{\mathrm{CIC}}^{\mathrm{ICRC}}(\cos^2\Theta)$ presented in the ICRC report [53] (dashed line). It becomes obvious, that the errors of $f_{\mathrm{CIC}}(\cos^2\Theta)$ are strongly underestimated, since the fit parameter correlations are not considered.

Appendix A

Figures of Chapter 5

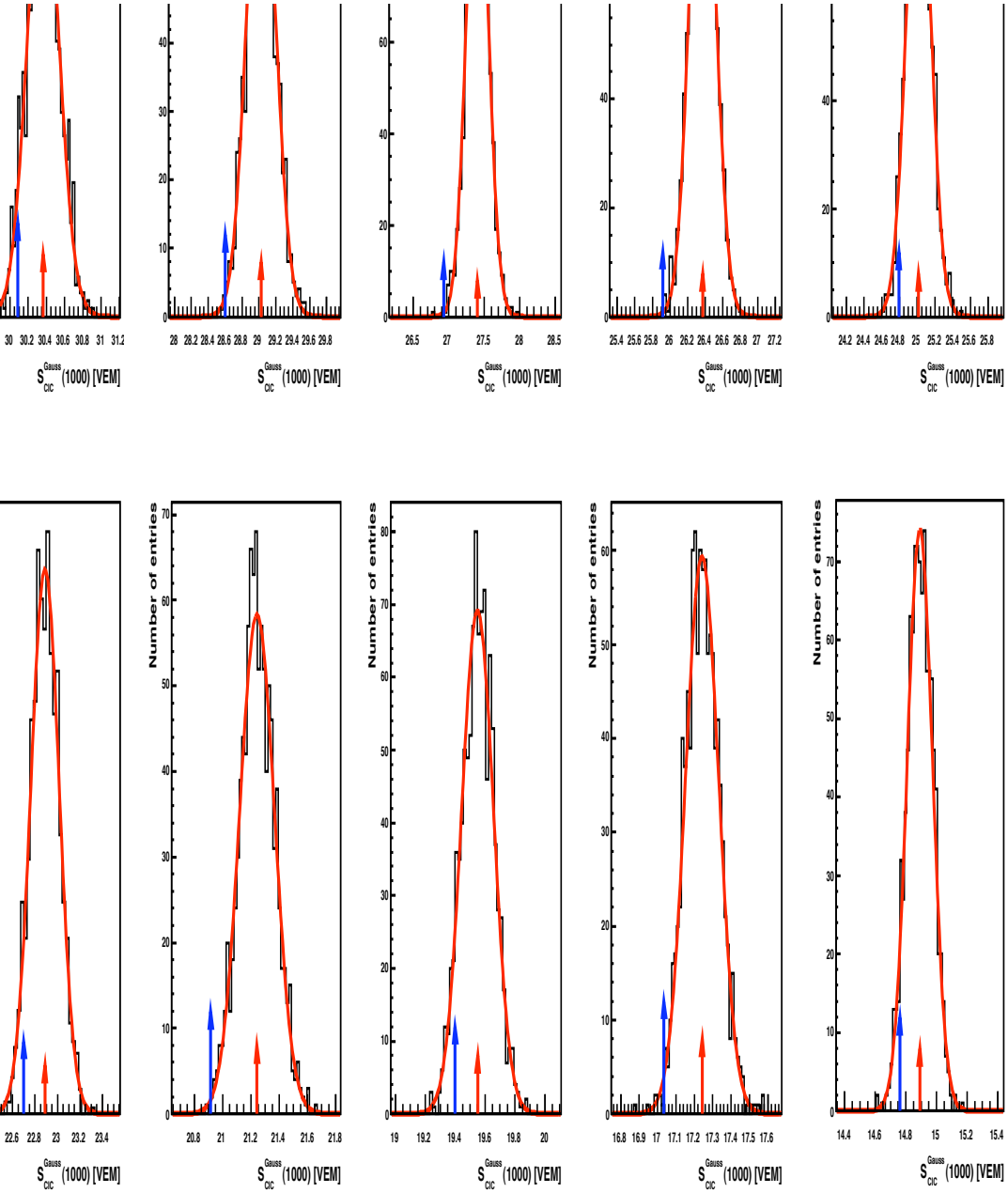

The Gaussian distributions of all ten bins. The long arrow marks the $S_{CIC}(1000)$ data value, the short arrow denotes the mean value of the Gaussian distribution.

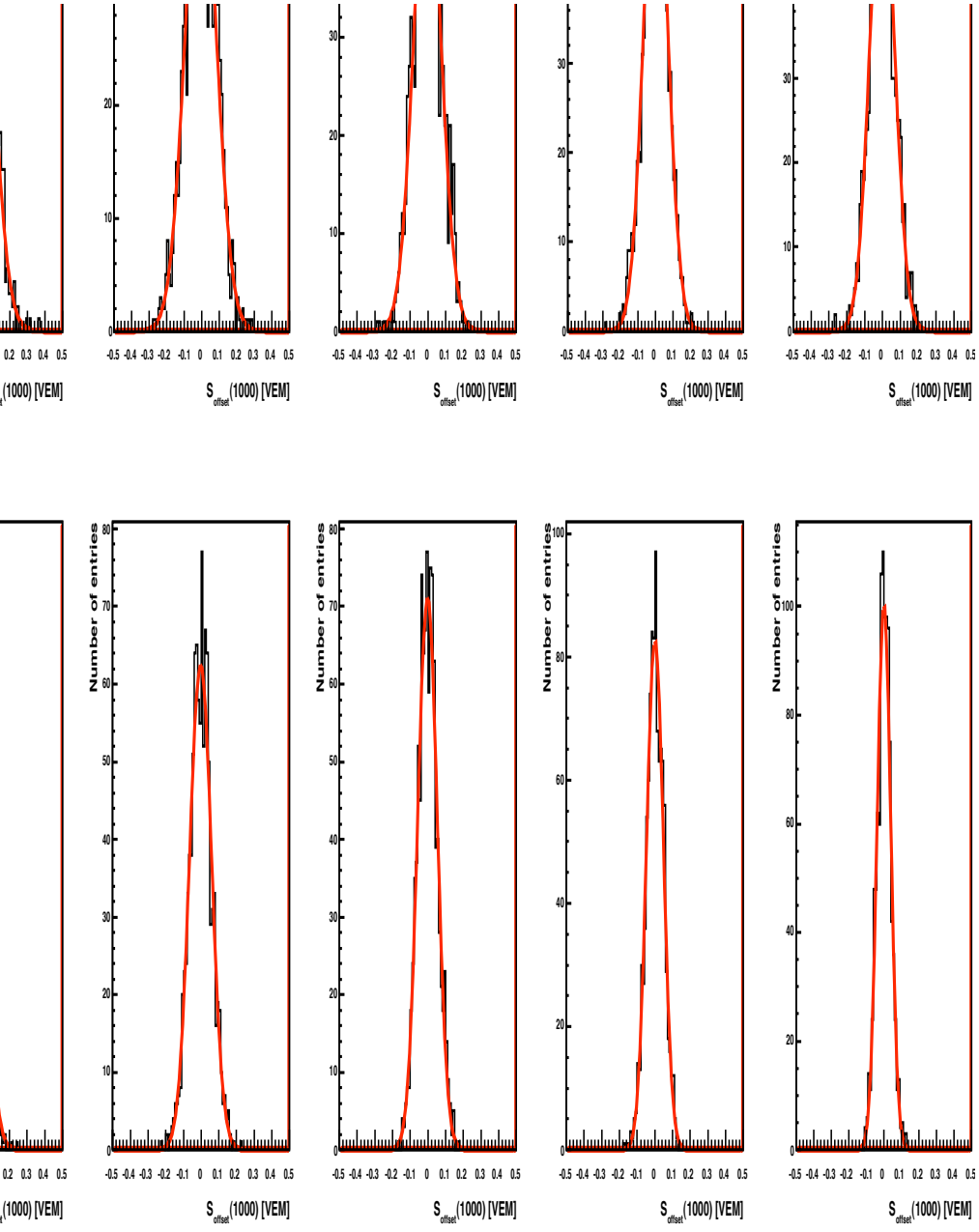

000) distribution of all ten bins. The mean values are compatible with zero, the $S^{\mathrm{Gauss}}(1000)$ spectrum is not shifted to higher

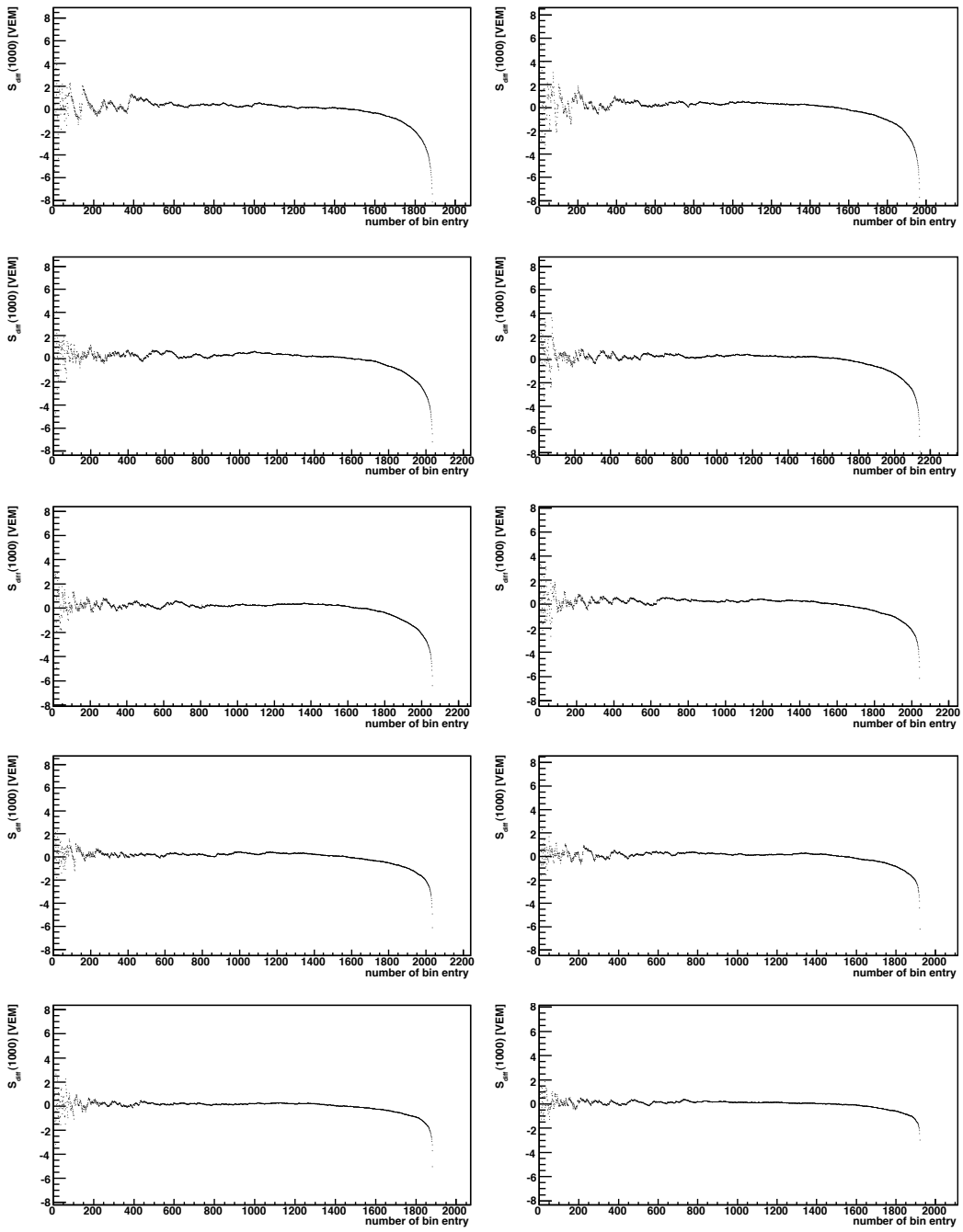

Figure A.3: $S_{\mathrm{diff}}(1000)$ versus bin entry number N for all ten bins. $S_{\mathrm{diff}}(1000)$ behaves equally for all ten bins.

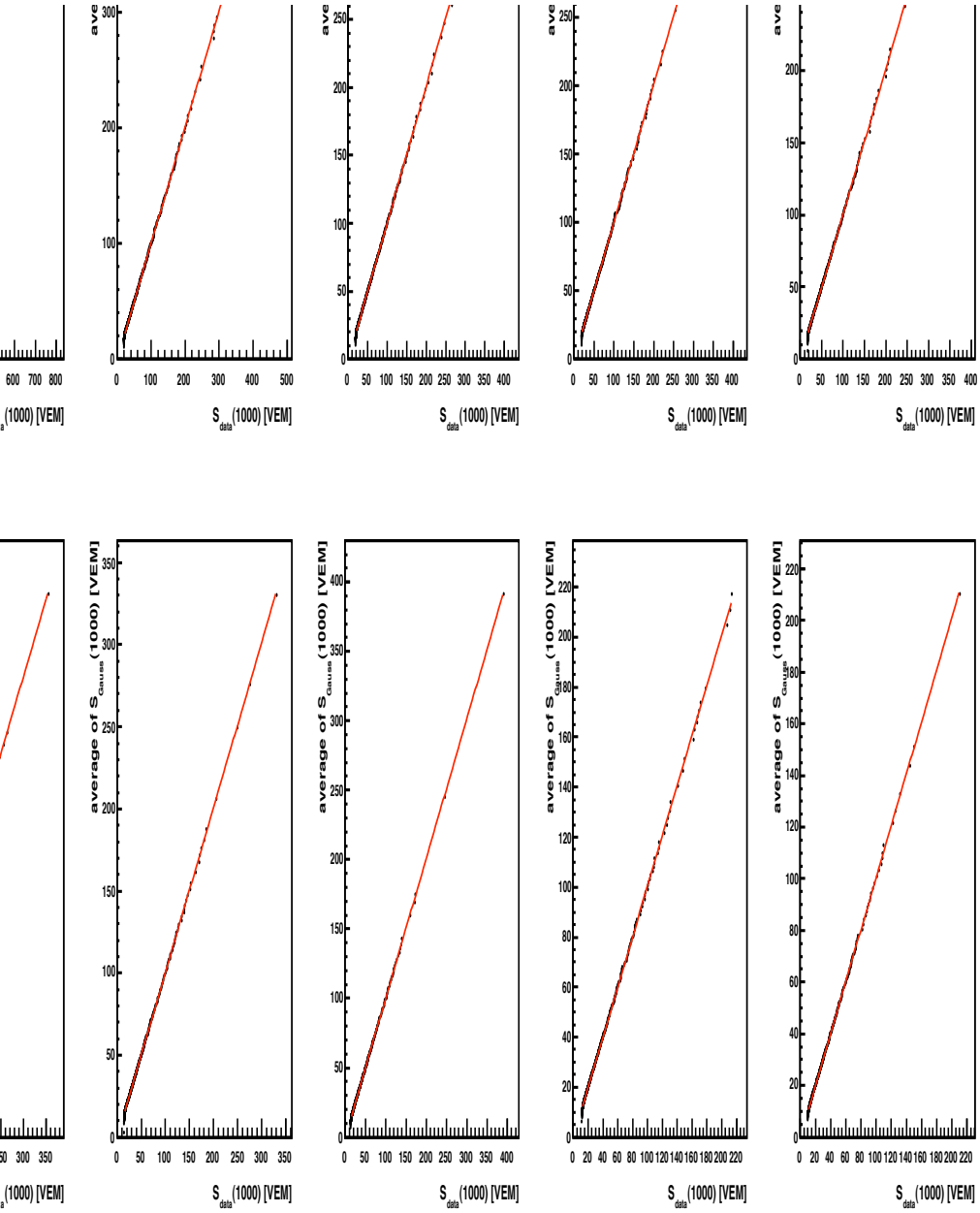

Figure A.4: All bins: $\overline{S}_N^{\text{Gauss}}(1000)$ versus $S_N^{\text{data}}(1000)$.

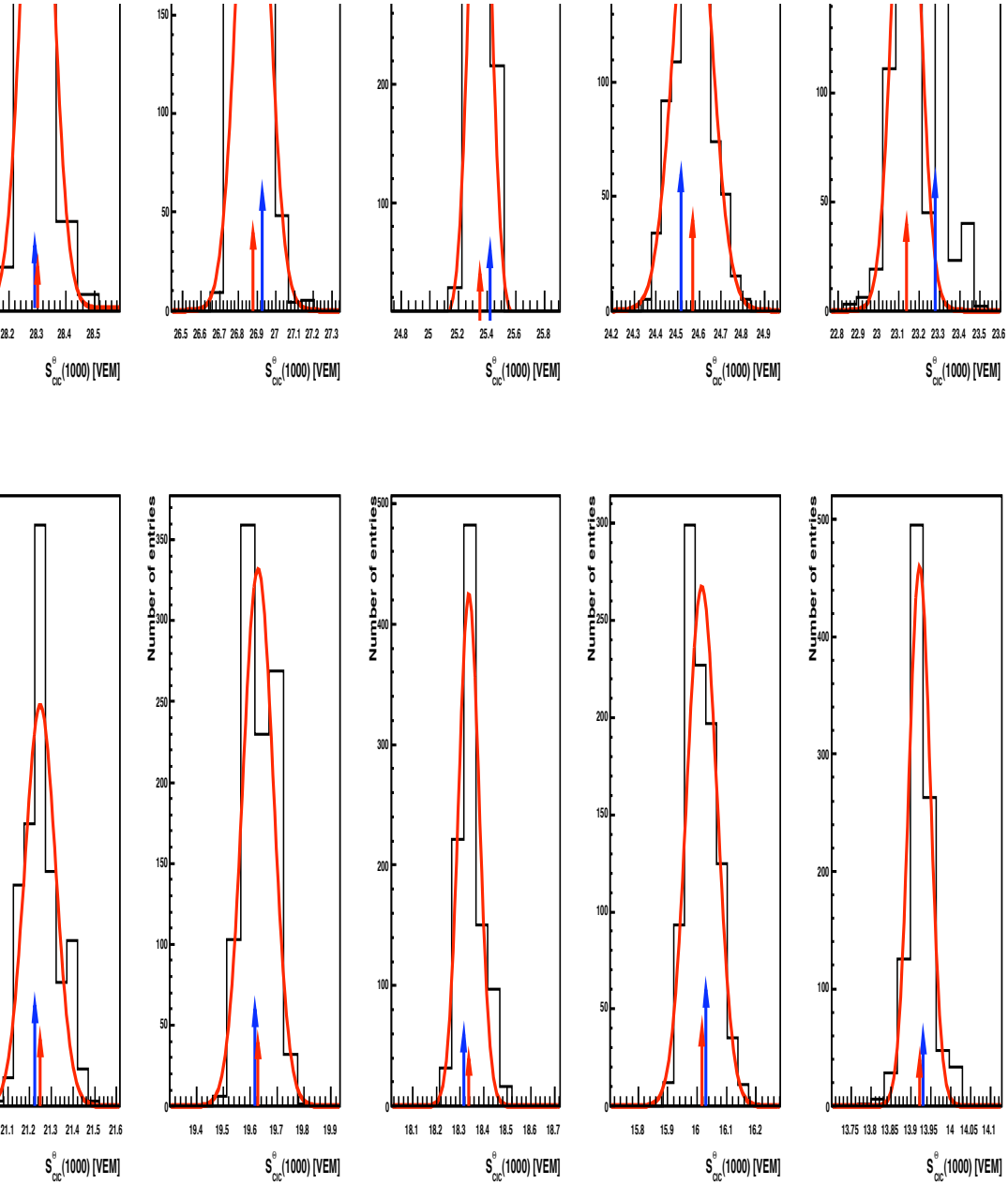

Distribution for $S^{\Theta}_{CIC}(1000)$ of all bins. The long arrow marks the $S_{CIC}(1000)$ data value, the small arrow the mean value of the Gaussian distribution of $S^{\Theta}_{CIC}(1000)$.

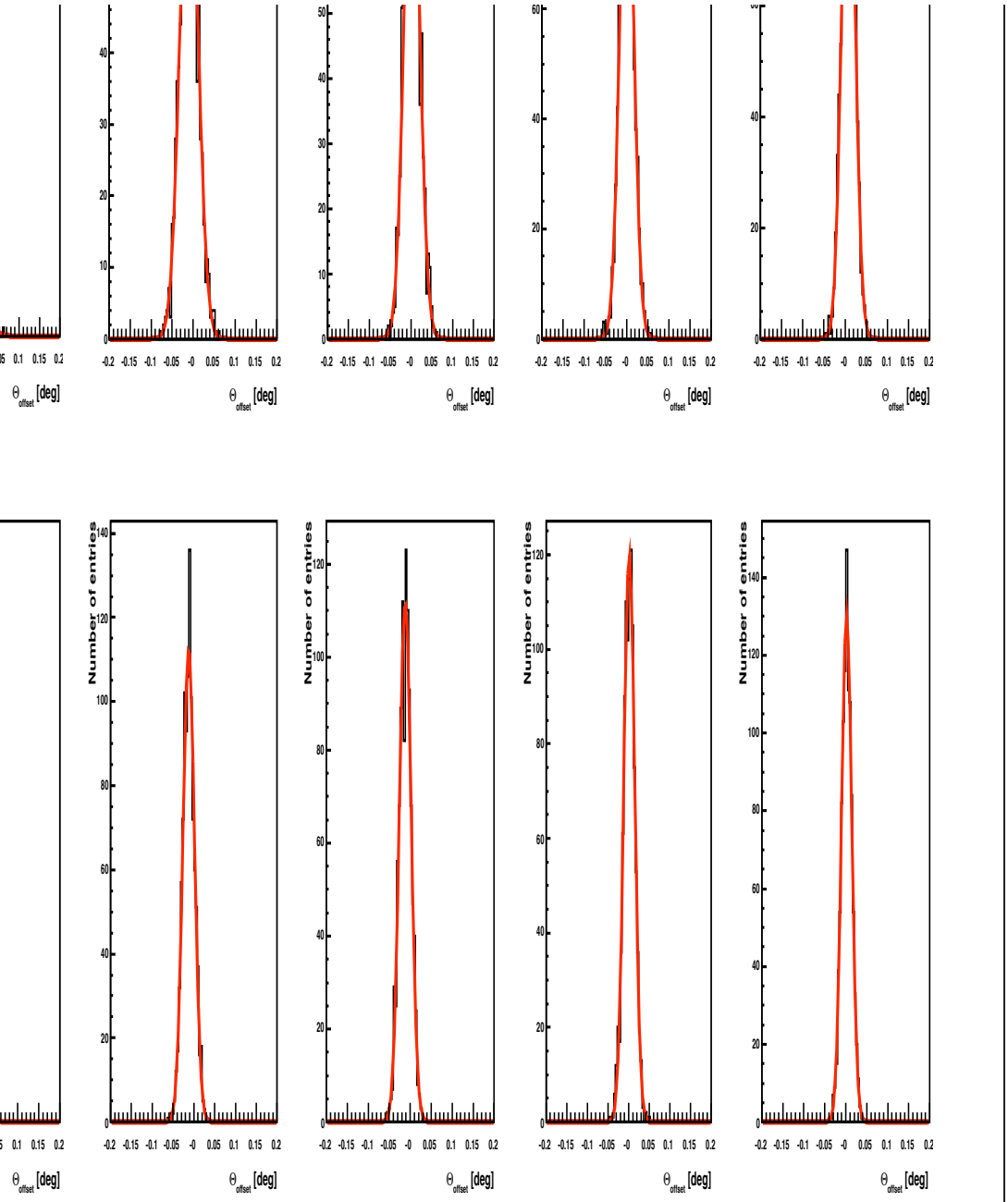

Figure A.6: The Θ_{offset} distributions for all ten bins.

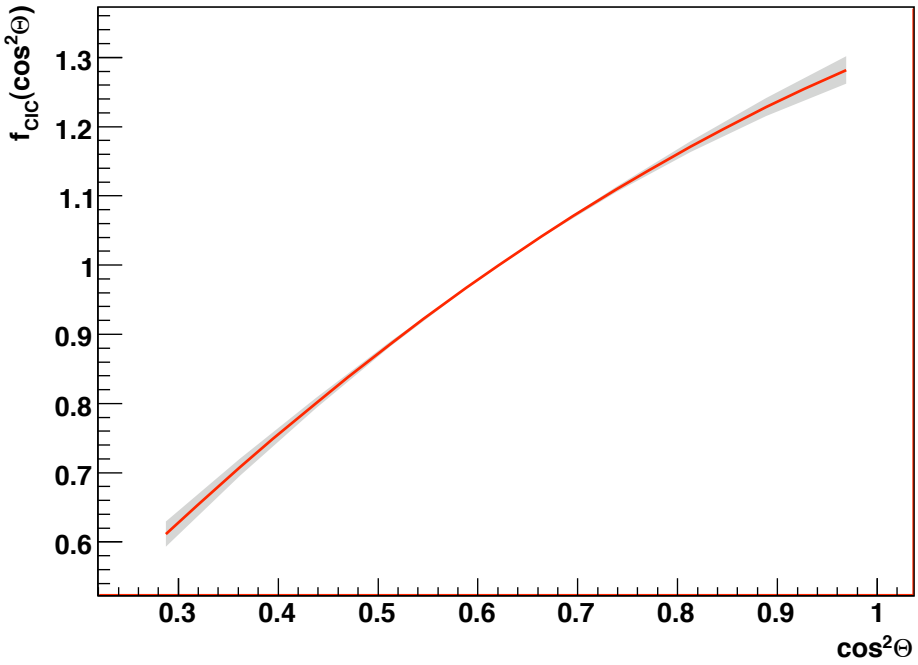

Figure A.7: Attenuation function $f(cos^2\Theta)$ in dependence of $cos^2\Theta$, plotted for Θ_- values. The intensity cut is made at bin entry $N_{\text{cut}} = 1030$.

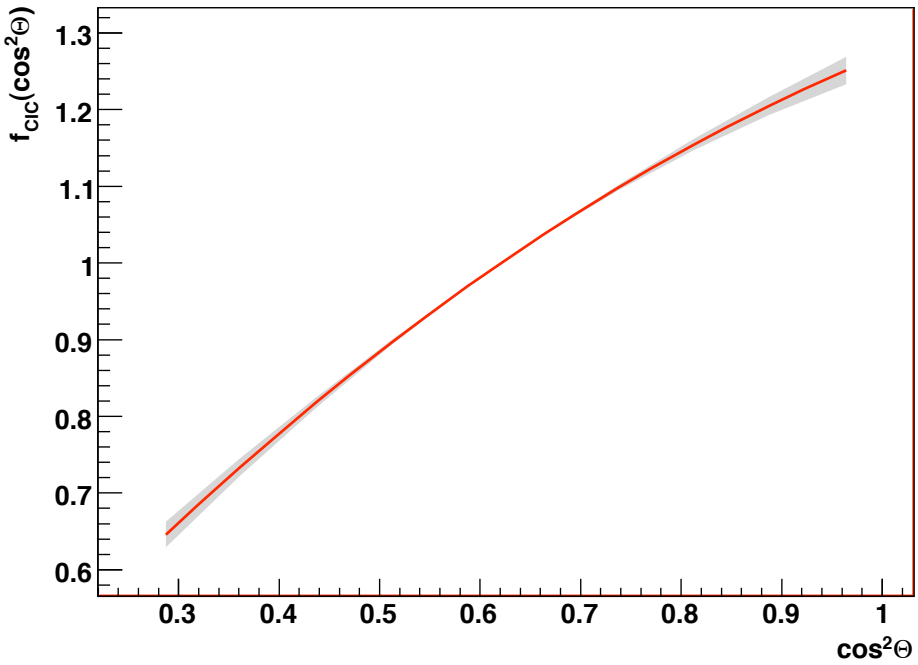

Figure A.8: Attenuation function $f(cos^2\Theta)$ in dependence of $cos^2\Theta$, plotted for Θ_+ values. The intensity cut is made at bin entry $N_{\text{cut}} = 1030$.

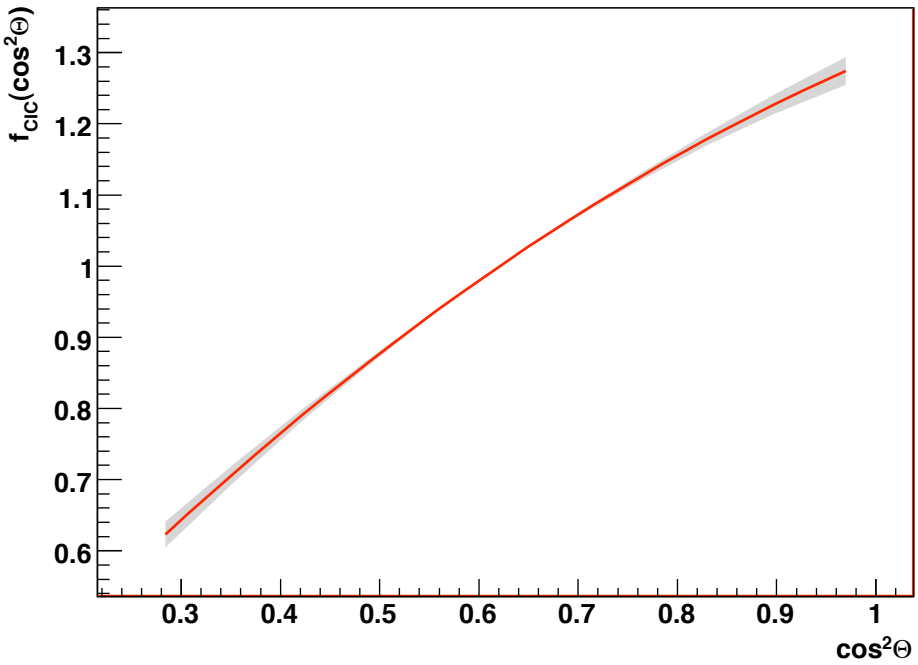

Figure A.9: $f_{\mathrm{CIC}}(cos^2\Theta)$ for the fragmentation into ten bins.

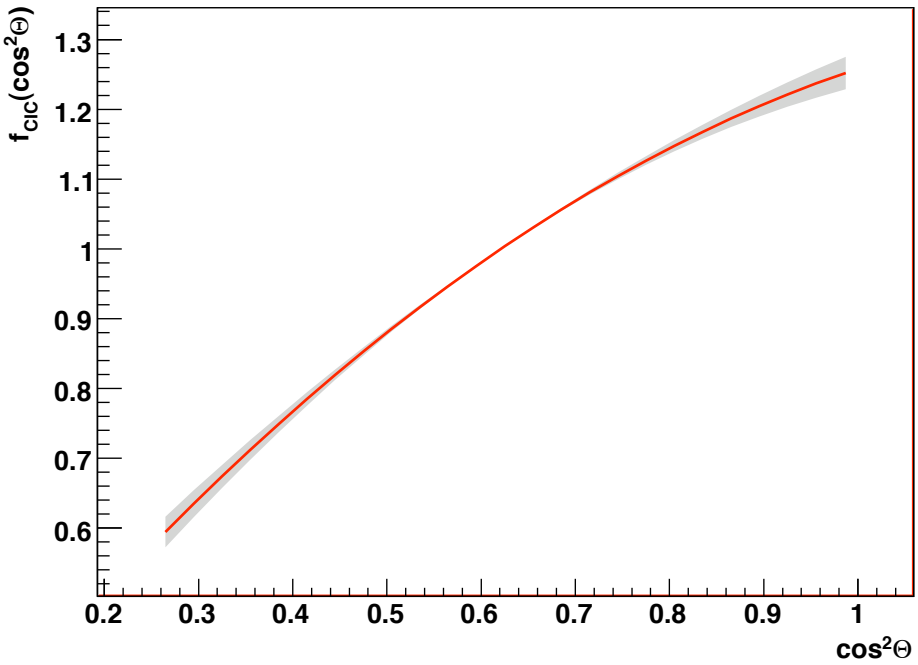

Figure A.10: $f_{\mathrm{CIC}}(cos^2\Theta)$ for the fragmentation into 25 bins.

Appendix B

Figures of Chapter 6

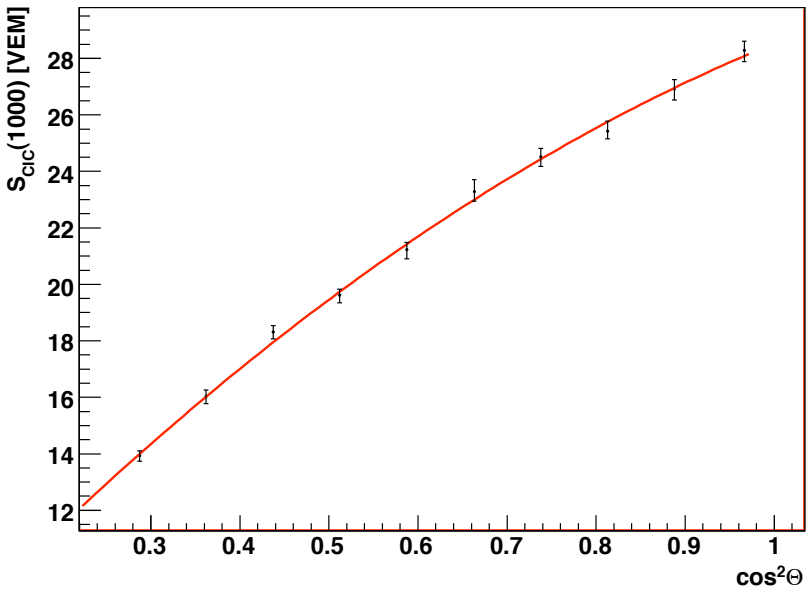

Figure B.1: $S_{CIC}(1000)$ in dependence on $\cos^2\Theta$. The intensity cut is made at $N_{\text{cut}} = 1150$ which corresponds to an energy of $E \approx 4.0$EeV.

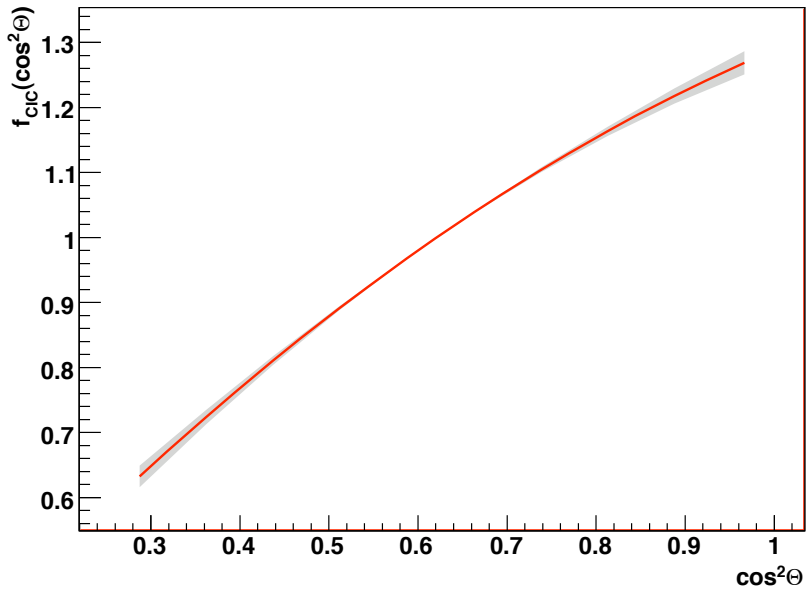

Figure B.2: $E \approx 4.0$EeV, $N_{\text{cut}} = 1150$: Attenuation function $f_{CIC}(\cos^2\Theta)$ vs. $\cos^2\Theta$.

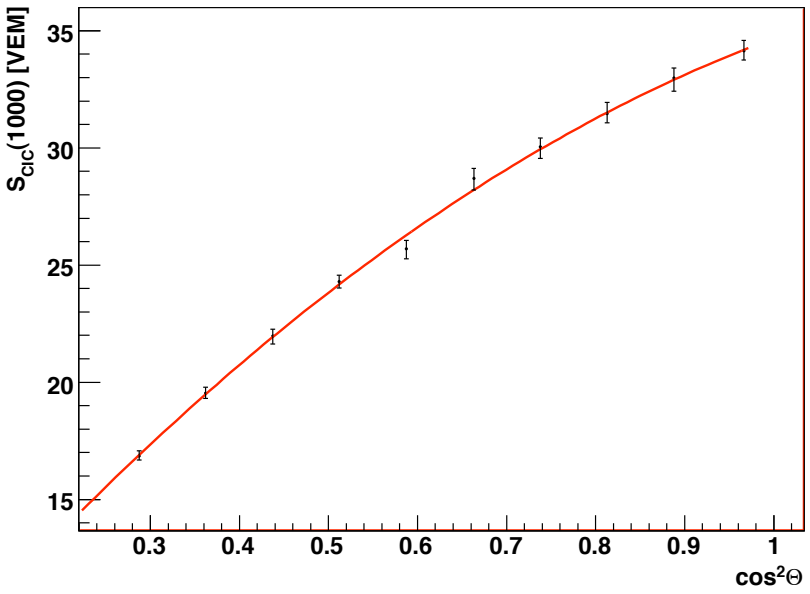

Figure B.3: $S_{CIC}(1000)$ in dependence on $\cos^2\Theta$. The intensity cut is made at $N_{\text{cut}} = 802$ which corresponds to an energy of $E \approx 5.0$EeV.

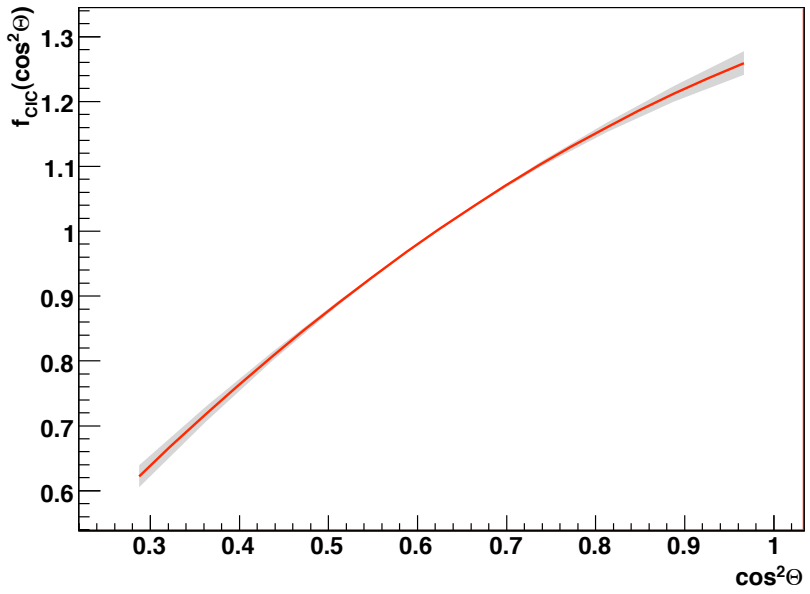

Figure B.4: $E \approx 5.0$EeV, $N_{\text{cut}} = 802$: Attenuation function $f_{CIC}(\cos^2\Theta)$ vs. $\cos^2\Theta$.

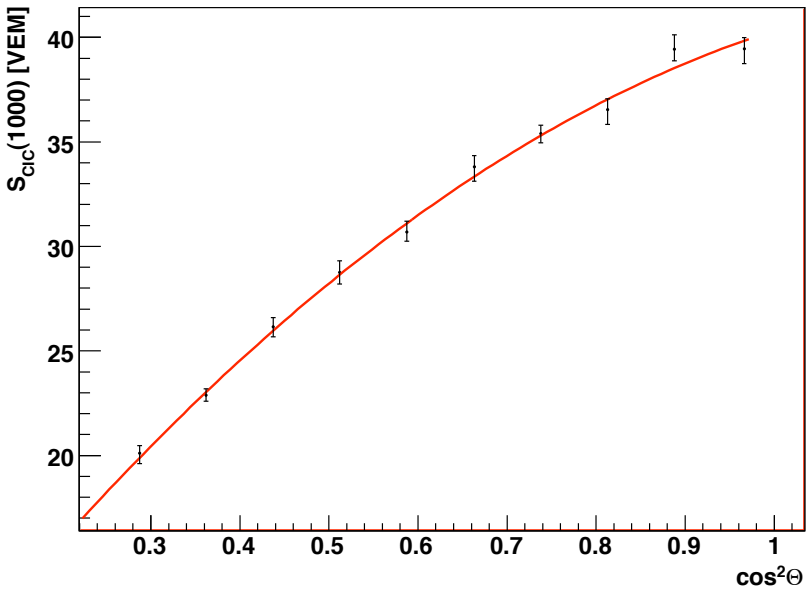

Figure B.5: $S_{CIC}(1000)$ in dependence on $\cos^2\Theta$. The intensity cut is made at $N_{\text{cut}} = 592$ which corresponds to an energy of $E \approx 6.0$EeV.

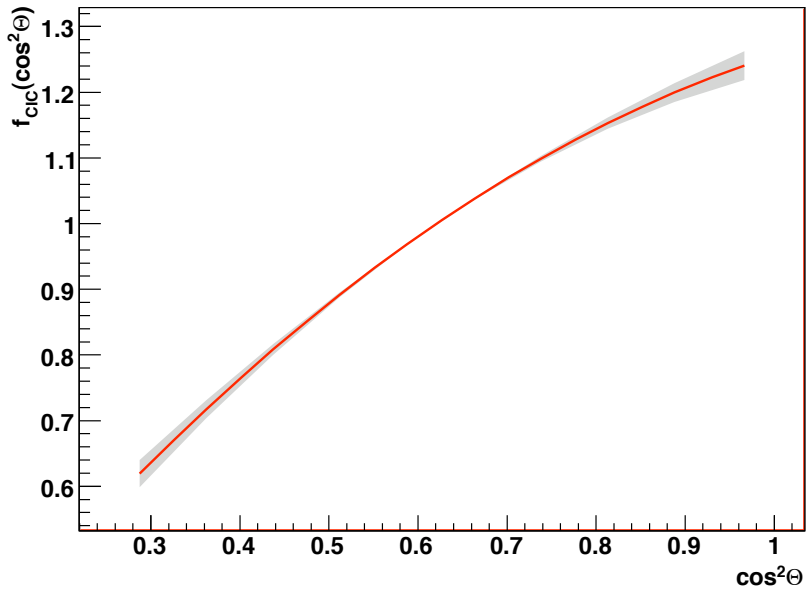

Figure B.6: $E \approx 6.0$EeV, $N_{\text{cut}} = 592$: Attenuation function $f_{CIC}(\cos^2\Theta)$ vs. $\cos^2\Theta$.

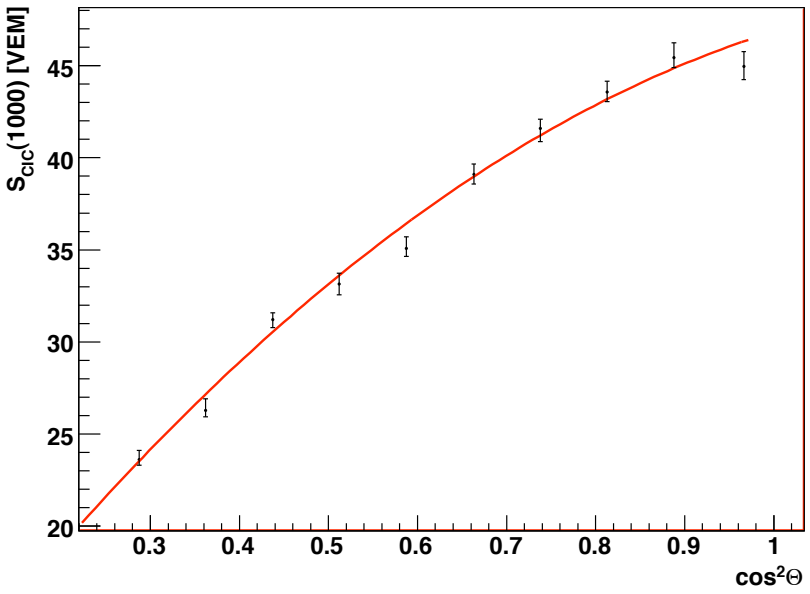

Figure B.7: $S_{CIC}(1000)$ in dependence on $\cos^2\Theta$. The intensity cut is made at $N_{\text{cut}} = 452$ which corresponds to an energy of $E \approx 7.0$EeV.

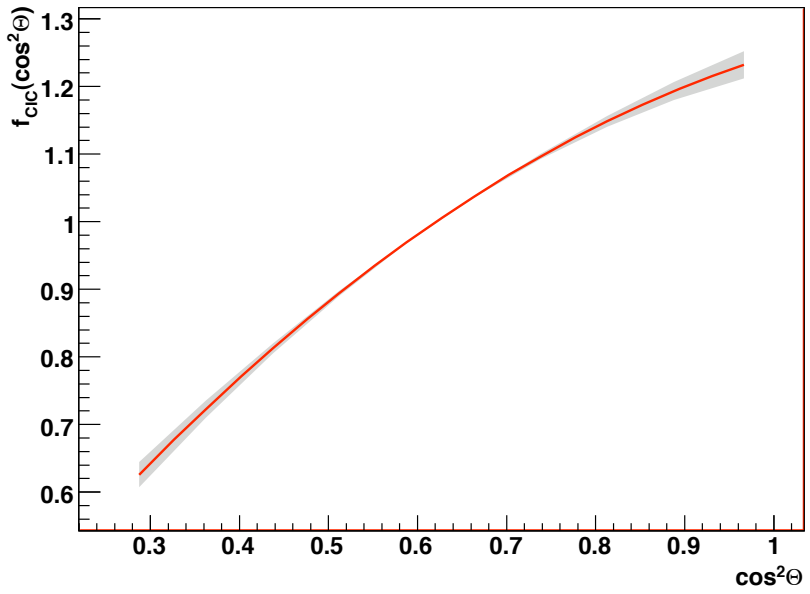

Figure B.8: $E \approx 7.0$EeV, $N_{\text{cut}} = 452$: Attenuation function $f_{CIC}(\cos^2\Theta)$ vs. $\cos^2\Theta$.

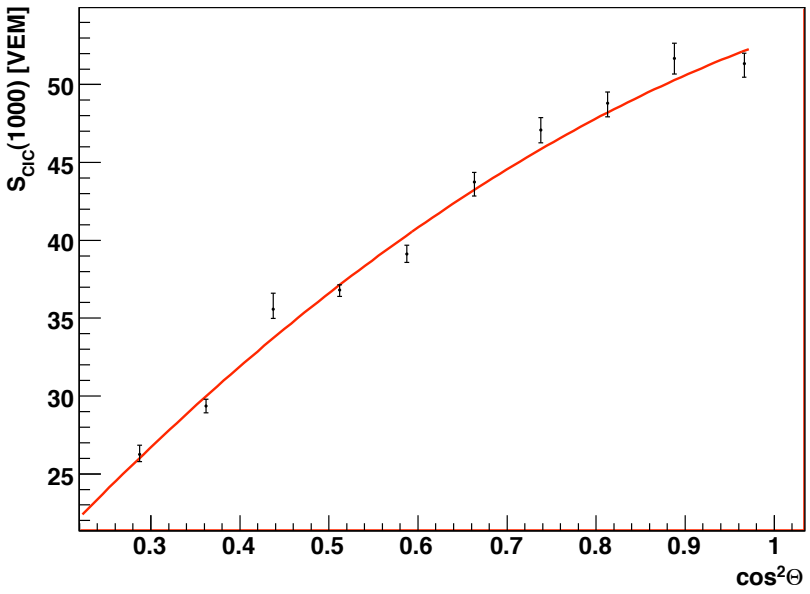

Figure B.9: $S_{CIC}(1000)$ in dependence on $\cos^2\Theta$. The intensity cut is made at $N_{\text{cut}} = 367$ which corresponds to an energy of $E \approx 8.0$EeV.

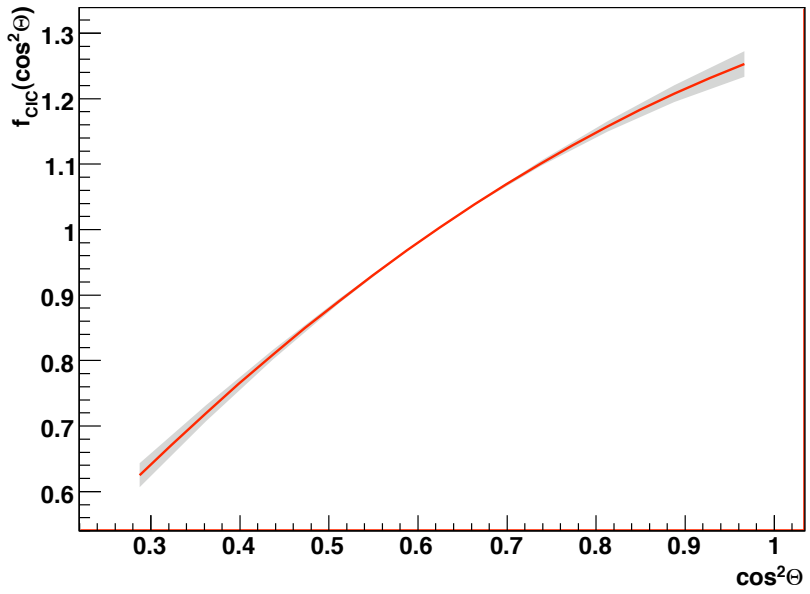

Figure B.10: $E \approx 8.0$EeV, $N_{\text{cut}} = 367$: Attenuation function $f_{CIC}(\cos^2\Theta)$ vs. $\cos^2\Theta$.

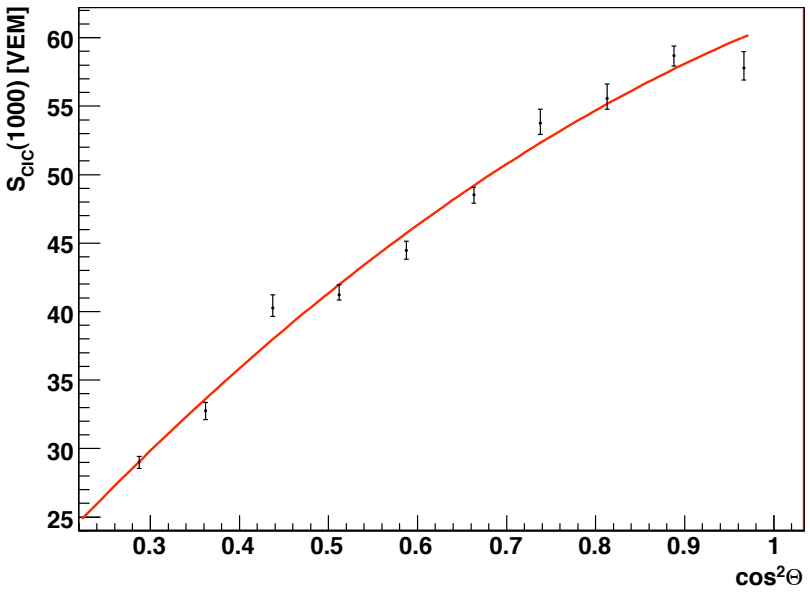

Figure B.11: $S_{CIC}(1000)$ in dependence on $\cos^2\Theta$. The intensity cut is made at $N_{\text{cut}} = 294$ which corresponds to an energy of $E \approx 9.0$EeV.

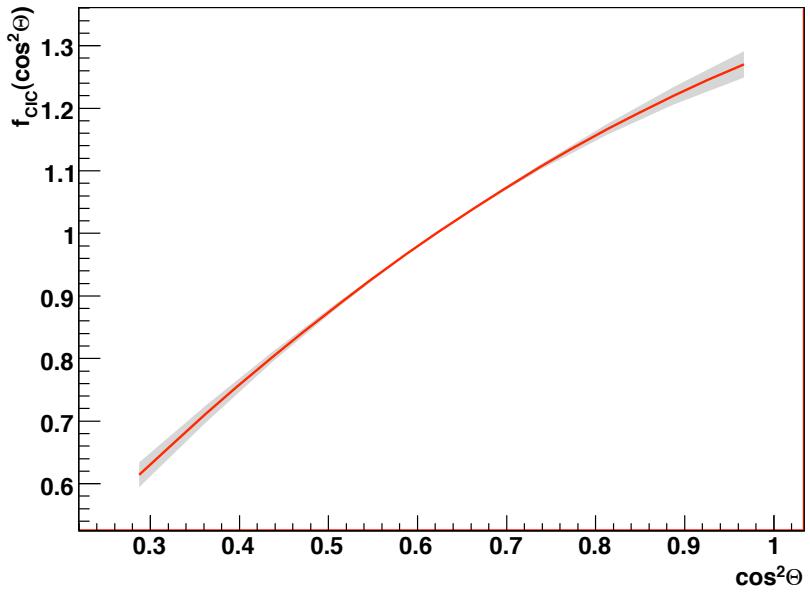

Figure B.12: $E \approx 9.0$EeV, $N_{\text{cut}} = 294$: Attenuation function $f_{CIC}(\cos^2\Theta)$ vs. $\cos^2\Theta$.

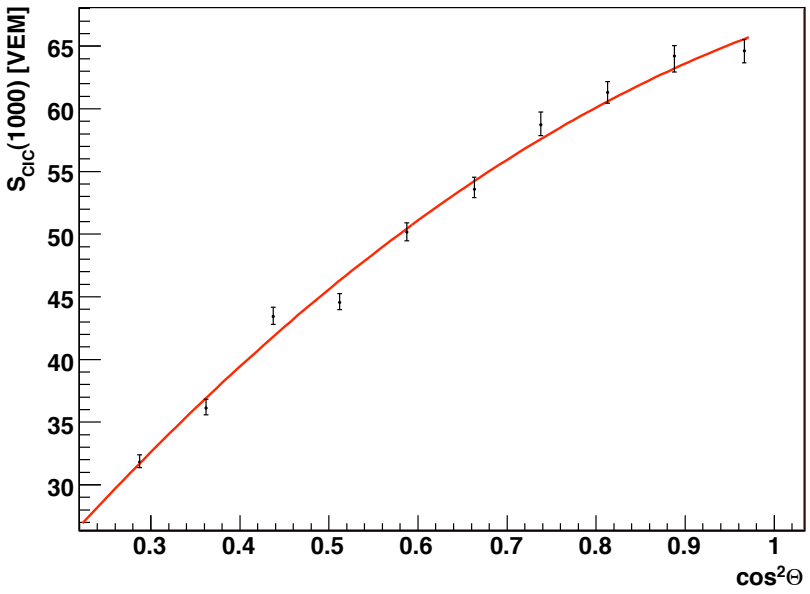

Figure B.13: $S_{CIC}(1000)$ in dependence on $\cos^2\Theta$. The intensity cut is made at $N_{\text{cut}} = 243$ which corresponds to an energy of $E \approx 10.0$EeV.

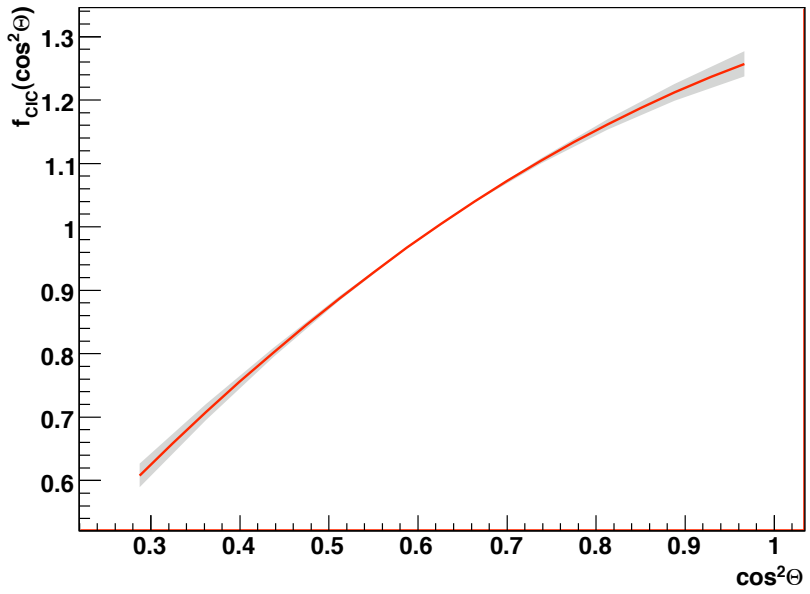

Figure B.14: $E \approx 10.0$EeV, $N_{\text{cut}} = 243$: Attenuation function $f_{CIC}(\cos^2\Theta)$ vs. $\cos^2\Theta$.

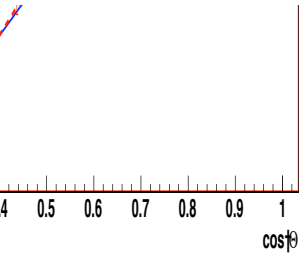

Comparison of temperature $T \leq 6.6\,^{\circ}\mathrm{C}$ (solid line) nd $T \geq 15.5\,^{\circ}\mathrm{C}$ (dashed line): $S_{CIC}(1000)$ of bin ntry $N_{\mathrm{cut}} = 315$, performed with $S(1000)$ data alues.

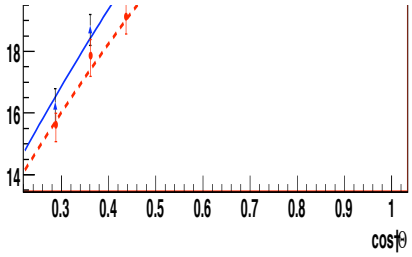

Figure B.16: Same as Figure B.15, but performed with weather corrected $S(1000)$ values.

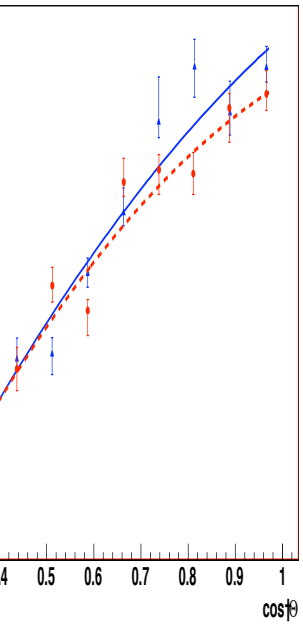

Comparison of temperature $T \leq 6.6\,^{\circ}\mathrm{C}$ (solid line) nd $T \geq 15.5\,^{\circ}\mathrm{C}$ (dashed line): $S_{CIC}(1000)$ of bin ntry $N_{\mathrm{cut}} = 138$, performed with $S(1000)$ data alues.

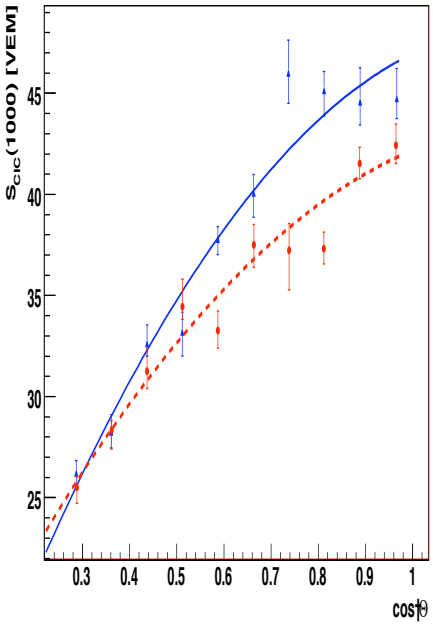

Figure B.18: Same as Figure B.17, but performed with weather corrected $S(1000)$ values.

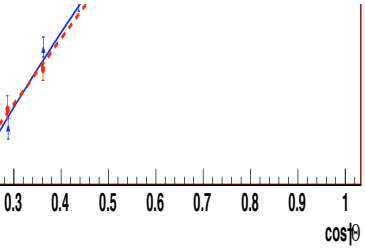

B.19: Comparison of humidity $H \leq 34.92\%$ (solid line) and $H \geq 76.80\%$ (dashed line): $S_{CIC}(1000)$ of bin entry $N_{cut} = 315$, performed with $S(1000)$ data values.

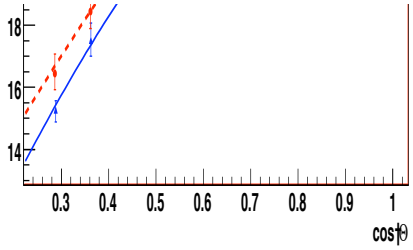

Figure B.20: Same as Figure B.19, but performed with weather corrected $S(1000)$ values.

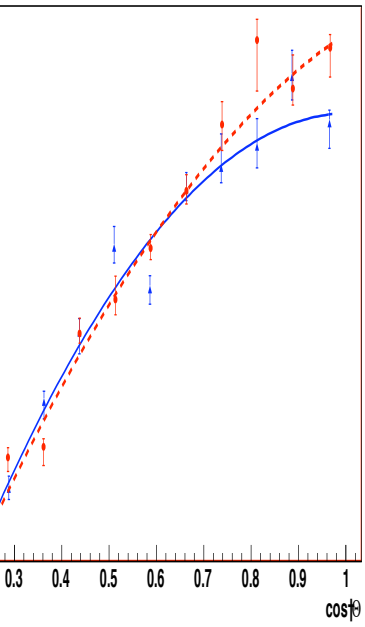

B.21: Comparison of humidity $H \leq 34.92\%$ (solid line) and $H \geq 76.80\%$ (dashed line): $S_{CIC}(1000)$ of bin entry $N_{cut} = 138$, performed with $S(1000)$ data values.

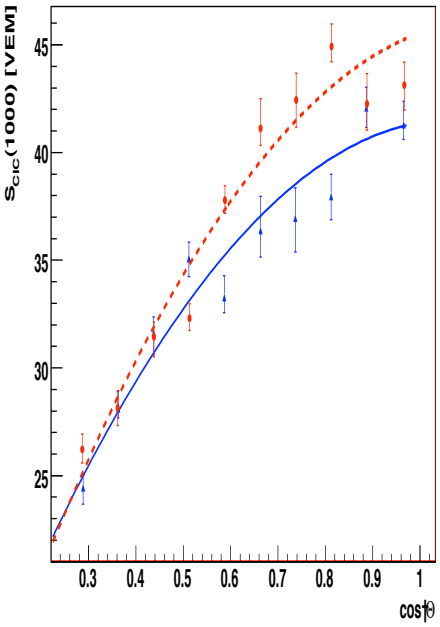

Figure B.22: Same as Figure B.21, but performed with weather corrected $S(1000)$ values.

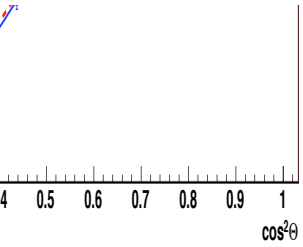

Comparison of pressure $P \leq 860.14$ hPa solid line) and $P \geq 863.56$ hPa (dashed line): $_{CIC}(1000)$ of bin entry $N_{cut} = 315$, performed ith $S(1000)$ data values.

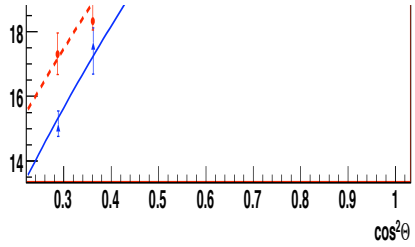

Figure B.24: Same as Figure B.23, but performed with weather corrected $S(1000)$ values.

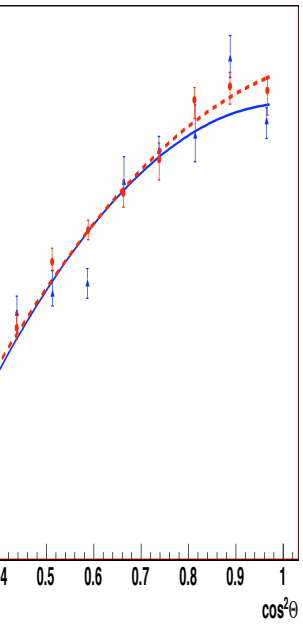

Comparison of pressure $P \leq 860.14$ hPa solid line) and $P \geq 863.56$ hPa (dashed line): $_{CIC}(1000)$ of bin entry $N_{cut} = 138$, performed ith $S(1000)$ data values.

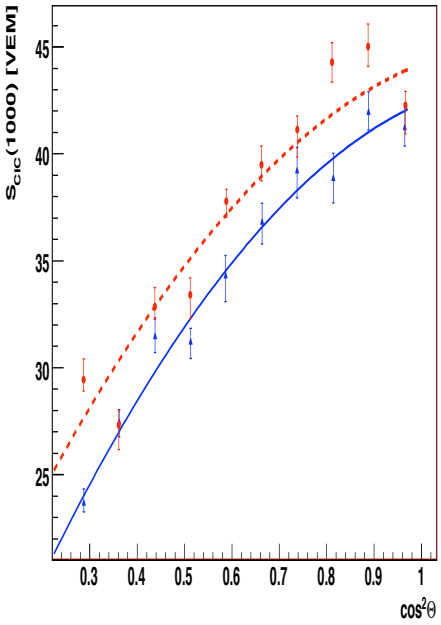

Figure B.26: Same as Figure B.25, but performed with weather corrected $S(1000)$ values.

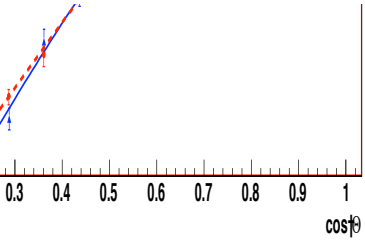

B.27: Comparison of density $\rho \leq 1.038$ kg/m^3 (solid line) and $\rho \geq 1.073$ kg/m^3 (dashed line): $S_{CIC}(1000)$ of bin entry $N_{\text{cut}} = 315$, performed with $S(1000)$ data values.

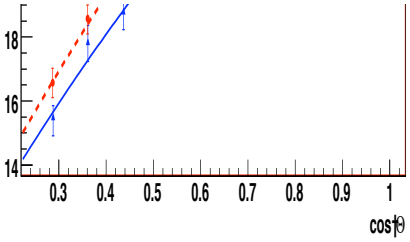

Figure B.28: Same as Figure B.27, but performed with weather corrected $S(1000)$ values.

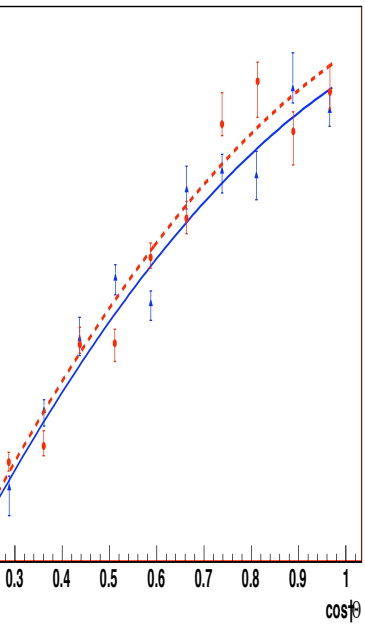

B.29: Comparison of density $\rho \leq 1.038$ kg/m^3 (solid line) and $\rho \geq 1.073$ kg/m^3 (dashed line): $S_{CIC}(1000)$ of bin entry $N_{\text{cut}} = 138$, performed with $S(1000)$ data values.

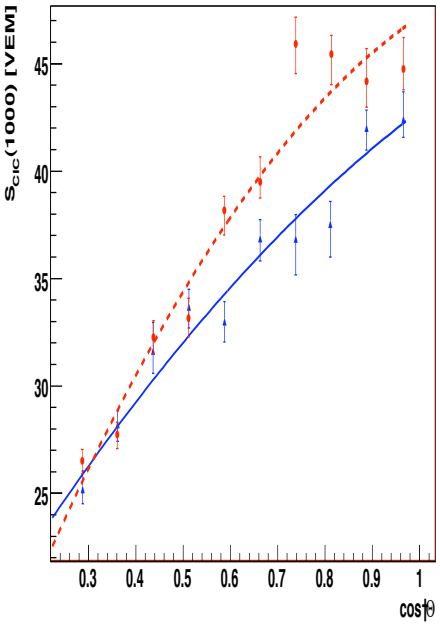

Figure B.30: Same as Figure B.29, but performed with weather corrected $S(1000)$ values.

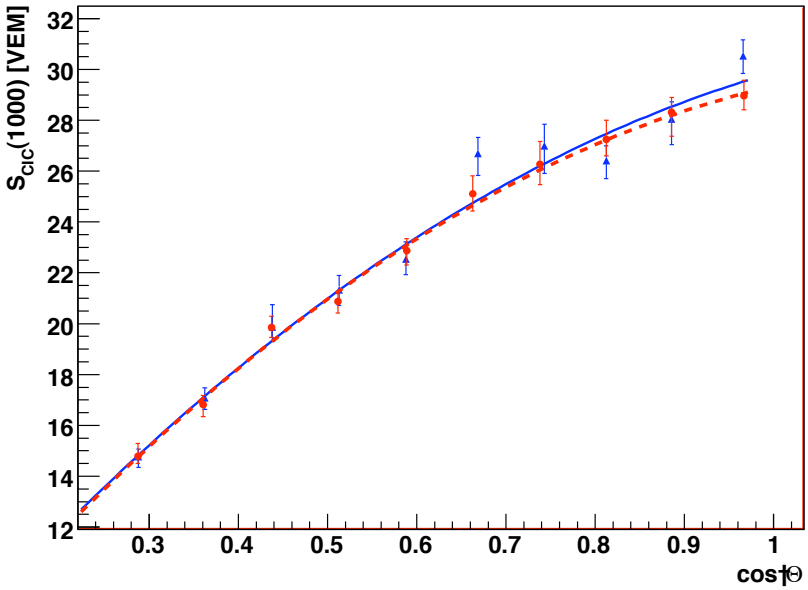

Figure B.31: Comparison of core distance $d_{\text{core}} \leq 441.0$ m (solid line) and $d_{\text{core}} \geq 664.2$ m (dashed line): $S_{CIC}(1000)$ versus $\cos^2\Theta$, performed for bin entry $N_{\text{cut}} = 338$.

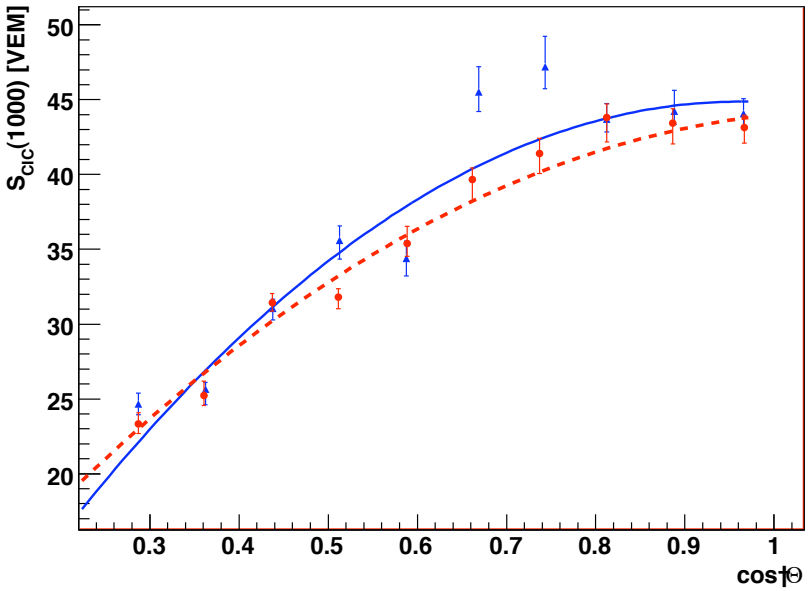

Figure B.32: Comparison of core distance $d_{\text{core}} \leq 441.0$ m (solid line) and $d_{\text{core}} \geq 664.2$ m (dashed line): $S_{CIC}(1000)$ versus $\cos^2\Theta$, performed for bin entry $N_{\text{cut}} = 148$.

List of Figures

2.1 Energy spectrum of primary cosmic rays. 5
2.2 Energy spectrum measured by different cosmic ray experiments. 6
2.3 Extensive air shower 7

3.1 Pierre Auger Observatory array. 12
3.2 Detector array of Auger North. 12
3.3 Surface detector. 14
3.4 Fluorescence detector. 15
3.5 Hybrid events. 16
3.6 Radio Antennas. 16
3.7 AMIGA array. 18
3.8 Temperature profile. 20
3.9 Humidity profile. 20
3.10 Pressure profile. 21
3.11 Density profile. 21

4.1 Charge and pulse histograms. 24
4.2 Raw histograms of station 1640 of event 200821400018. 26
4.3 Zenith angle and the energy distribution of T4 triggered events. 27
4.4 T5 trigger requirements. 28
4.5 Signal fluctuation and lateral trigger probability (LTP). 29
4.6 Θ distribution for all events and full acceptance events. 30
4.7 Plane versus spherical shower front. 32
4.8 LDF of event 200821400018. 33
4.9 Calibration of SD events, using hybrid events. 34

5.1 Effective detector area. 37
5.2 Zenith angle distribution. 37
5.3 Number of events in the equal sized Θ bins. 39
5.4 $S_{\mathrm{CIC}}(1000)$ curve, performed without correction. 40
5.5 $S_{\mathrm{CIC}}(1000)$ curve, performed with correction. 41
5.6 $S(1000)$ shuffling: Gaussian distribution for the first bin. 43
5.7 Distribution of $S_{\mathrm{offset}}(1000)$ for the first bin. 44
5.8 $S_{\mathrm{diff}}(1000)$ versus bin entry number N for the first bin. 45
5.9 First bin: $\overline{S}_N^{\mathrm{Gauss}}(1000)$ versus $S_N^{\mathrm{data}}(1000)$. 46

5.10 First bin: Distribution of $S^{\Theta}_{\mathrm{CIC}}(1000)$. 47
5.11 Θ_{offset} distribution of the first two bins. 48
5.12 $f_{\mathrm{CIC}}(\cos^2\Theta)$ for $N_{\mathrm{cut}} = 1030$. 50
5.13 Number of bin entries for Θ_+ and Θ_-. 51
5.14 $S_{\mathrm{CIC}}(1000)$ curves for Θ_-, Θ and Θ_+. 52
5.15 $f_{\mathrm{CIC}}(cos^2\Theta)$ for Θ_-, Θ and Θ_+. 52
5.16 Number of bin entries for a segmentation into ten and 25 bins. 53
5.17 $S_{\mathrm{CIC}}(1000)$ curve for a segmentation into eleven bins. 54
5.18 $S_{\mathrm{CIC}}(1000)$ curve for a segmentation into 25 bins. 55
5.19 $f_{\mathrm{CIC}}(cos^2\Theta)$ for segmentations into eleven and 25 bins. 55

6.1 $S_{\mathrm{CIC}}(1000)$ curve for $N_{\mathrm{cut}} = 452$. 58
6.2 $N_{\mathrm{cut}} = 452$ for $N_{\mathrm{cut}} = 452$. 60
6.3 Comparison of $f_{\mathrm{CIC}}(\cos^2\Theta)$ at different energies. 60
6.4 Fit of the parameters a and b. 62
6.5 Number of bin entries for a winter and a summer data subset. 63
6.6 $S_{\mathrm{CIC}}(1000)$ curve for seasonal data subsets and $E \approx 4.3$ EeV. 64
6.7 $S_{\mathrm{CIC}}(1000)$ curve for seasonal data subsets and $E \approx 7.0$ EeV. 64
6.8 $f_{\mathrm{CIC}}(\cos^2\Theta)$ for seasonal data subsets and $E \approx 4.3$ EeV. 65
6.9 $f_{\mathrm{CIC}}(\cos^2\Theta)$ for seasonal data subsets and $E \approx 7.0$ EeV. 65
6.10 Temperature distribution. 67
6.11 Number of bin entries for temperature data subsets. 67
6.12 $f_{\mathrm{CIC}}(\cos^2\Theta)$ for temperature data subsets and $E \approx 4.3$ EeV. 69
6.13 $f_{\mathrm{CIC}}(\cos^2\Theta)$ for corrected temperature data subsets and $E \approx 4.3$ EeV. . . 69
6.14 $f_{\mathrm{CIC}}(\cos^2\Theta)$ for temperature data subsets and $E \approx 7.0$ EeV. 69
6.15 $f_{\mathrm{CIC}}(\cos^2\Theta)$ for corrected temperature data subsets and $E \approx 7.0$ EeV. . . 69
6.16 Humidity distribution. 70
6.17 Number of bin entries for humidity data subsets. 71
6.18 $f_{\mathrm{CIC}}(\cos^2\Theta)$ for humidity data subsets and $E \approx 4.3$ EeV. 72
6.19 $f_{\mathrm{CIC}}(\cos^2\Theta)$ for corrected humidity data subsets and $E \approx 4.3$ EeV. 72
6.20 $f_{\mathrm{CIC}}(\cos^2\Theta)$ for humidity data subsets and $E \approx 7.0$ EeV. 72
6.21 $f_{\mathrm{CIC}}(\cos^2\Theta)$ for corrected humidity data subsets and $E \approx 7.0$ EeV. 72
6.22 Pressure distribution. 73
6.23 Number of bin entries for pressure data subsets. 74
6.24 $f_{\mathrm{CIC}}(\cos^2\Theta)$ for pressure data subsets and $E \approx 4.3$ EeV. 75
6.25 $f_{\mathrm{CIC}}(\cos^2\Theta)$ for corrected pressure data subsets and $E \approx 4.3$ EeV. 75
6.26 $f_{\mathrm{CIC}}(\cos^2\Theta)$ for pressure data subsets and $E \approx 7.0$ EeV. 75
6.27 $f_{\mathrm{CIC}}(\cos^2\Theta)$ for corrected pressure data subsets and $E \approx 7.0$ EeV. 75
6.28 Density distribution. 76
6.29 Number of bin entries for density data subsets. 77
6.30 $f_{\mathrm{CIC}}(\cos^2\Theta)$ for density data subsets and $E \approx 4.3$ EeV. 78
6.31 $f_{\mathrm{CIC}}(\cos^2\Theta)$ for corrected density data subsets and $E \approx 4.3$ EeV. 78
6.32 $f_{\mathrm{CIC}}(\cos^2\Theta)$ for density data subsets and $E \approx 7.0$ EeV. 78
6.33 $f_{\mathrm{CIC}}(\cos^2\Theta)$ for corrected density data subsets and $E \approx 7.0$ EeV. 78
6.34 Shower axis and shower core distance. 79

6.35 Shower axis distance distribution 80
6.36 Zenith angle distributions for shower axis distance data subsets. 80
6.37 Number of bin entries for shower axis distance data subsets. 81
6.38 Maximum core distance. 81
6.39 Shower core distance distribution. 82
6.40 Zenith angle distributions for shower axis distance data subsets. 83
6.41 Number of bin entries for shower core distance data subsets. 83
6.42 $f_{\mathrm{CIC}}(\cos^2\Theta)$ for shower core distance data subsets and $E \approx 4.3$ EeV. . . . 84
6.43 $f_{\mathrm{CIC}}(\cos^2\Theta)$ for shower core distance data subsets and $E \approx 7.0$ EeV. . . . 84

7.1 Comparison of $f_{\mathrm{CIC}}(\cos^2\Theta)$ and $f_{\mathrm{CIC}}^{\mathrm{ICRC}}(\cos^2\Theta)$. 87

A.1 $S(1000)$ shuffling: Gaussian distributions for all ten bins. 90
A.2 Distribution of $S_{\mathrm{offset}}(1000)$ for all ten bins. 91
A.3 $S_{\mathrm{diff}}(1000)$ versus bin entry number N for all ten bins. 92
A.4 All bins: $\overline{S}_N^{\mathrm{Gauss}}(1000)$ versus $S_N^{\mathrm{data}}(1000)$. 93
A.5 Distribution of $S_{\mathrm{CIC}}^{\Theta}(1000)$ for all bins. 94
A.6 The Θ_{offset} distributions for all ten bins. 95
A.7 $f(cos^2\Theta)$ in dependence of $cos^2\Theta$, plotted for Θ_- values. 96
A.8 $f(cos^2\Theta)$ in dependence of $cos^2\Theta$, plotted for Θ_+ values. 96
A.9 $f_{\mathrm{CIC}}(cos^2\Theta)$ for the fragmentation into ten bins. 97
A.10 $f_{\mathrm{CIC}}(cos^2\Theta)$ for the fragmentation into 25 bins. 97

B.1 $S_{CIC}(1000)$ curve at an energy of $E \approx 4.0$EeV 100
B.2 $f_{CIC}(\cos^2\Theta)$ at an energy of $E \approx 4.0$EeV. 100
B.3 $S_{CIC}(1000)$ curve at an energy of $E \approx 5.0$EeV 101
B.4 $f_{CIC}(\cos^2\Theta)$ at an energy of $E \approx 5.0$EeV. 101
B.5 $S_{CIC}(1000)$ curve at an energy of $E \approx 6.0$EeV 102
B.6 $f_{CIC}(\cos^2\Theta)$ at an energy of $E \approx 6.0$EeV. 102
B.7 $S_{CIC}(1000)$ curve at an energy of $E \approx 7.0$EeV. 103
B.8 $f_{CIC}(\cos^2\Theta)$ at an energy of $E \approx 7.0$EeV. 103
B.9 $S_{CIC}(1000)$ curve at an energy of $E \approx 8.0$EeV. 104
B.10 $f_{CIC}(\cos^2\Theta)$ at an energy of $E \approx 8.0$EeV. 104
B.11 $S_{CIC}(1000)$ curve at an energy of $E \approx 9.0$EeV. 105
B.12 $f_{CIC}(\cos^2\Theta)$ at an energy of $E \approx 9.0$EeV. 105
B.13 $S_{CIC}(1000)$ curve at an energy of $E \approx 10.0$EeV. 106
B.14 $f_{CIC}(\cos^2\Theta)$ at an energy of $E \approx 10.0$EeV. 106
B.15 $S_{CIC}(1000)$ curve for temperature data subsets and $E \approx 4.3$ EeV. 107
B.16 $S_{CIC}(1000)$ curve for corrected temperature data subsets and $E \approx 4.3$ EeV. 107
B.17 $S_{CIC}(1000)$ curve for temperature data subsets and $E \approx 7.0$ EeV. 107
B.18 $S_{CIC}(1000)$ curve for corrected temperature data subsets and $E \approx 7.0$ EeV. 107
B.19 $S_{CIC}(1000)$ curve for humidity data subsets and $E \approx 4.3$ EeV. 108
B.20 $S_{CIC}(1000)$ curve for corrected humidity data subsets and $E \approx 4.3$ EeV. . 108
B.21 $S_{CIC}(1000)$ curve for humidity data subsets and $E \approx 7.0$ EeV. 108
B.22 $S_{CIC}(1000)$ curve for corrected humidity data subsets and $E \approx 7.0$ EeV. . 108

B.23 $S_{CIC}(1000)$ curve for pressure data subsets and $E \approx 4.3$ EeV. 109
B.24 $S_{CIC}(1000)$ curve for corrected pressure data subsets and $E \approx 4.3$ EeV. . . 109
B.25 $S_{CIC}(1000)$ curve for pressure data subsets and $E \approx 7.0$ EeV. 109
B.26 $S_{CIC}(1000)$ curve for corrected pressure data subsets and $E \approx 7.0$ EeV. . . 109
B.27 $S_{CIC}(1000)$ curve for density data subsets and $E \approx 4.3$ EeV. 110
B.28 $S_{CIC}(1000)$ curve for corrected density data subsets and $E \approx 4.3$ EeV. . . 110
B.29 $S_{CIC}(1000)$ curve for density data subsets and $E \approx 7.0$ EeV. 110
B.30 $S_{CIC}(1000)$ curve for corrected density data subsets and $E \approx 7.0$ EeV. . . 110
B.31 $S_{CIC}(1000)$ curve for shower core distance data subsets and $E \approx 4.3$ EeV. 111
B.32 $S_{CIC}(1000)$ curve for shower core distance data subsets and $E \approx 7.0$ EeV. 111

List of Tables

5.1 Θ limits of each bin. 38
5.2 Error estimation of $S_{\mathrm{CIC}}(1000)$ at $N_{\mathrm{cut}} = 1030$. 49
5.3 The parameters a and b of $f_{\mathrm{CIC}}(cos^2\Theta)$ for Θ, Θ_+ and Θ_-. 53
5.4 The parameters a and b of $f_{\mathrm{CIC}}(cos^2\Theta)$ for ten, eleven and 25 bins. 54

6.1 Correction factors p_{N_i} and resulting N_{CIC_i}. 58
6.2 Error estimation of $S_{\mathrm{CIC}}(1000)$ at $N_{\mathrm{cut}} = 452$. 59
6.3 The parameters a and b of $f_{\mathrm{CIC}}(cos^2\Theta)$ for different energies. 61
6.4 The parameters a and b of $f_{\mathrm{CIC}}(cos^2\Theta)$ for seasonal data subsets. 63
6.5 The parameters a and b of $f_{\mathrm{CIC}}(cos^2\Theta)$ for temperature data subsets. . . . 68
6.6 The parameters a and b of $f_{\mathrm{CIC}}(cos^2\Theta)$ for corrected temperature data subsets. 68
6.7 The parameters a and b of $f_{\mathrm{CIC}}(cos^2\Theta)$ for humidity data subsets. 71
6.8 The parameters a and b of $f_{\mathrm{CIC}}(cos^2\Theta)$ for corrected humidity data subsets. 71
6.9 The parameters a and b of $f_{\mathrm{CIC}}(cos^2\Theta)$ for pressure data subsets. 74
6.10 The parameters a and b of $f_{\mathrm{CIC}}(cos^2\Theta)$ for corrected pressure data subsets. 74
6.11 The parameters a and b of $f_{\mathrm{CIC}}(cos^2\Theta)$ for density data subsets. 77
6.12 The parameters a and b of $f_{\mathrm{CIC}}(cos^2\Theta)$ for corrected density data subsets. 77
6.13 The parameters a and b of $f_{\mathrm{CIC}}(cos^2\Theta)$ for shower core distance data subsets. 83

List of Acronyms

Acronym	Explanation
AGN	Active galactic nuclei
AMIGA	Auger Muons and Infill for the Ground Array
CDAS	Central data acquisition system
CIC	Constant intensity cut
CLF	Central laser facility
CR	Cosmic rays
EAS	Extensive air shower
FADC	Flash analogue digital converter
FD	Fluorescence detector
GPS	Global positioning system
HEAT	High Elevation Auger Telescopes
LDF	Lateral distribution function
LL	Fluorescence telescope Los Leones
LTP	Lateral trigger probability
MC	Monte Carlo
PAO	Pierre Auger Observatory
PMT	Photomultiplier tube
$S(1000)$	Signal at a distance of 1000 m from the shower axis
$S_{CIC}(1000)$	$S(1000)$ value with bin entrie number N_{CIC}
S_{38}	S_{38° is the value of $S(1000)$ at a zenith angle of $\Theta = 38^\circ$
SD	Surface detector
ST	Single threshold
ToT	Time over threshold
UHECR	Ultra high energy cosmic ray
VEM	Vertical equivalent muon

Bibliography

[1] see e.g.: M. Longair, *High energy astrophysics, vol. 1*, 1992, cambridge University Press.

[2] P. Auger *et al.*, *Extensive Cosmic-Ray Showers*, Rev. Mod. Phys., *vol. 11*(3-4), 1939:288–291.

[3] see e.g.: C. Grupen, *Astroparticle physics*, 2005, springer-Verlag Berlin Heidelberg.

[4] T. Abu-Zayyad *et al.*, *Measurement of the spectrum of UHE cosmic rays by the FADC detector of the HiRes experiment*, Astropart. Phys., *vol. 23*, 2005:157–174.

[5] T. Abu-Zayyad *et al.*, *A measurement of the average longitudinal development profile of cosmic ray air showers between 10**17-eV and 10**18-eV*, Astropart. Phys., *vol. 16*, 2001:1–11.

[6] R. Abbasi *et al.*, *Observation of the GZK cutoff by the HiRes experiment*, Phys. Rev. Lett., *vol. 100*, 2008.

[7] N. Hayashida *et al.*, *Updated AGASA event list above 4*10**19-eV*, 2000.

[8] K. H. Kampert *et al.*, *Cosmic rays in the 'knee'-region: Recent results from KASCADE*, Acta Phys. Polon., *vol. B35*, 2004:1799–1812.

[9] M. e. a. Ave, Proceedings of the 27th ICRC (Hamburg, Germany), 2001, pp. 381.

[10] M. e. a. Pravadin, Proceedings of the 28th ICRC (Tuskuba), 2007, pp. 389.

[11] Y. Tokonatsu, Proceedings of the 30th ICRC (Mérida, México), 2007, pp. 1318.

[12] http://apcauger.in2p3.fr/Public/Presentation/Images/spectre.jpg, online accessed 06.10.2008.

[13] K. Greisen, *End to the cosmic ray spectrum?*, Phys. Rev. Lett., *vol. 16*, 1966:748–750.

[14] http://www.auger.de/public/teilchen.html, online accessed 07.10.2008.

[15] D. Kickelbick, *The energy spectrum of primary cosmic rays measured with the KASKADE-Grande experiment, PhD thesis, University of Siegen, Germany*, 2008.

[16] see e.g.: O. Alkhofer, *Introduction to cosmic radiation*, 1975, verlag Carl Thiemig.

[17] K. Greisen, *The extensive air showers*, Prog. Cosmic Ray Physics, *vol. III*, 1966:1–141.

[18] J. Abraham *et al.*, *Correlation of the highest energy cosmic rays with nearby extra-galactic objects*, Science, *vol. 318*, 2007:938–943.

[19] http://www.auger.de/public/sd.de.html,
online accessed 13.10.2008.

[20] I. Allekotte *et al.*, *The Surface Detector System of the Pierre Auger Observatory*, Nucl. Instrum. Meth., *vol. A586*, 2008:409–420.

[21] http://www.scielo.br/img/revistas/bjp/v36n4a/a12fig02.gif,
online accessed 17.10.2008.

[22] http://www.phy.mtu.edu/faculty/fick/Fig1tankcloseup.jpg,
online accessed 17.10.2008.

[23] http://research.roma2.infn.it/ auger/alignginanni.jpg,
online accessed 17.10.2008.

[24] http://www-hep2.fzu.cz/Auger/optic1.jpg,
online accessed 17.10.2008.

[25] http://astro.uni-wuppertal.de/ kampert/HE-Astro/hybrid.gif,
online accessed 18.10.2008.

[26] http://www.sciam.com/media/inline/20EB9007-E7F2-99DF-3611274085979E33.jpg,
online accessed 18.10.2008.

[27] O. Scholten, *Ultra-High Energy Cosmic Rays, entering a new Era of Astroparticle Physics and Detection Techniques*, 2007, proceedings of Science (MRU) 038.

[28] C. Timmermans, *Radio detection of Cosmic Rays at the Pierre Auger Observatory*, 2007, subm. to Proc. Roma Int. Conf. on Astro-Particle Physics, June 20-22, 2007, Rome, Italy.

[29] http://www.augerradio.org/wiki/moin.cgi/Public,
online accessed 17.10.2008.

[30] A. D. Supanitsky *et al.*, *Underground Muon Counters as a Tool for Composition Analyses*, Astropart. Phys., *vol. 29*, 2008:461–470.

[31] A. Etchegoyen, Proceedings of the 30th ICRC (Mérida, México), 2007, pp. 1307.

[32] H. Klages, Proceedings of the 30th ICRC (Mérida, México), 2007, pp. 713.

[33] X. Bertou *et al.*, *On weather effects, how to account for them and large scale anisotropy searches*, 2006, GAP2006-098, internal report, not for public display.

[34] B. Keilhauer *et al.*, *Molecular atmosphere profiles for Malargüe*, 2005, GAP2005-021, internal report, not for public display.

[35] M. Aglietta *et al.*, *Calibration of the surface array of the Pierre Auger Observatory*, Proceedings of the 29th ICRC (Pune, India), 2005, pp. 130.

[36] X. Bertou *et al.*, *Calibration of the Surface Array of the Pierre Auger Observatory*, Subm. to Nucl. Instr. Meth., 2006.

[37] D. Allard *et al.*, *The trigger system of the PAO surface detector: operation, efficiency and stability*, Proceedings of the 29th ICRC (Pune, India), 2005, pp. 116.

[38] M. Gomez Berisso *et al.*, *Computation of the Auger surface detector probability from real data*, 2005, GAP2005-059, internal report, not for public display.

[39] X. Bertou, *SDCast: The SD event broadcaster in CDAS*, 2007, GAP2007-089, internal report, not for public display.

[40] B. Becker *et al.*, *Comparison of different SD reconstructions*, 2007, GAP2007-068, internal report, not for public display.

[41] P. Privitera *et al.*, *The Angular Reconstruction and Angular Resolution of Air Showers detected at the Pierre Auger Observatory*, Proceedings of the 28th ICRC (Tsukuba, Japan), 2003, pp. 357.

[42] E. Armengaud *et al.*, *Fitting a variable radius of curvature*, 2003, GAP2003-108, internal report, not for public display.

[43] M. Ave *et al.*, *The accuracy of signal measurements with the water-Cherenkov detectors of the Pierre Auger Observatory*, Subm. to Nucl. Instr. Meth., *vol. A*, 2006.

[44] T. Schmidt *et al.*, *Fine tuning of the LDF parametrisation and the influence on* $S(1000)$, 2007, GAP2007-106, internal report, not for public display.

[45] P. Sommers, *First estimate of the primary cosmic ray energy spectrum above 3-EeV from the Pierre Auger observatory*, 2005.

[46] J. Abraham *et al.*, *Observation of the suppression of the flux of cosmic rays above* 4×10^{19} *eV*, Phys. Rev. Lett., *vol. 101*, 2008.

[47] J. Hersil *et al.*, *Observation of extensiver air showers near the maximum of their longitudinal development*, Phys. Rev. Lett., *vol. 6*, 1961.

[48] http://particulas.cnea.gov.ar/experiments/auger/private/monit/, online accessed 10.10.2008.

[49] H. Asorey, *Private conversation*, 2008.

[50] H. Asorey and E. Roulet, *Private conversation*, 2008.

[51] I. Allekotte *et al.*, *You thought you understood the hexagons?*, 2008, GAP2008-114, internal report, not for public display.

[52] I. Maris, *Measurement of the Ultra High Energy Cosmic Ray Flux using data of the Pierre Auger Observatory*, 2008, GAP2008-026, internal report, not for public display.

[53] M. Roth *et al.*, *Measurement of the UHECR energy spectrum using data from the Surface Detector of the Pierre Auger Observatory*, Proceedings of the 30th ICRC (Mérida, México), 2007, pp. 313.

Acknowledgement

proofreading My gratitude goes out to all those, who made this thesis possible.

First of all I would like to thank Prof. Dr. Ivor Fleck, who made it possible for me, to take part in the research for the Pierre Auger Observatory. Working on this interesting experiment has been a very pleasant and instructive experience. Furthermore I would like to thank him for the opportunity to spend half a year in San Carlos de Bariloche, Argentina.

Another person, who made this stay possible, is Prof. Dr. Ingo Allekotte. I am very thankful that he agreed to revise this thesis, for his supervision and also for his friendship.

My gratefulness goes out to the whole Bariloche group, for their warm hospitality and scientific support. I hope, we stay in contact. Especially I would like to thank Hernán Asorey, for the helpful discussions and to be a friend of mine. Another thank goes to Dr. Xavier Bertou, who had everytime an answer to all of my questions.

Additional I would like to thank all members of our working group, for the pleasant atmosphere. A special thank goes to Thomas Bäcker and Dr. Dirk Kickelbick, for spending hours in proofreading and discussing of physical questions, but foremost for the funny, amusing lunch breaks. It was a great pleasure!

Last but not least, I am proud to express my gratitude to my whole family. A special thank goes to Stefan Grebe, not only for his scientific, but also for his private support. Thank you for your love and your trust. I am very grateful for the support, my parents and my sister Alissa gave to me during my whole life and, as I know them, also will give me in the future. Thanks to you!

Erklärung

Hiermit erkläre ich, dass ich die vorliegende Masterarbeit selbstständig verfasst habe und keine anderen als die angegebenen Quellen und Hilfsmittel benutzt, sowie Zitate und Ergebnisse Anderer kenntlich gemacht habe.

(Ort) (Datum)	(Isabell Kristin Steinseifer)